An Extreme-UV Optical Multichannel Analyser with Resolution Enhancement for Laser Plasma Spectroscopy

A Thesis for the Degree of
Master of Science

submitted to

School of Physical Sciences
Dublin City University

by

Matthew Shaw B.Sc.

Research Supervisor
Dr. John T. Costello

September 1996

Declaration

I hereby certify that this material, which I now submit for assessment on the programme of study to the award of Masters of Science, is entirely my own work and has not been taken from the work of others save and to the extent that such work has been cited and acknowledged within the text of my work.

Signature : Matthew Shaw

Date : 24/9/96.

To Camilla and my parents

ABSTRACT

The development and characterisation of a multichannel extreme-UV (XUV) spectrometer system for emission and absorption spectroscopy of laser produced plasmas is described. The system consists of a 2.2m grazing incidence vacuum spectrometer to which an XUV sensitive array detector is coupled. The multichannel detector consists of a Galileo® Channel Electron Multiplier Array (CEMA) with Photodiode Array (PDA) readout. A comprehensive and user friendly software package for array detector/ experiment control and data acquisition was developed. The total system performance is illustrated by emission spectra of aluminium, aluminium oxide and tungsten and photoabsorption spectra of helium gas and thin aluminium samples. Limitations of the current system for the measurement of photoabsorption cross-sections are discussed.

The fundamental principles underlying three important classes of deconvolution methods, Fourier, Constrained Non-Linear and Maximum Likelihood, are described. The results of computer codes developed to implement each of the above techniques are presented and intercompared. Strengths and weaknesses of each technique are discussed with reference to restored emission spectra. The potential of deconvolution for resolution gain is demonstarted by application to an instrumentally broadened He 1s2 - 2s2p doubly excited resonance profile.

The thesis concludes with a description of future work on system characterisation and optimsation.

Table of Contents

Chapter 1

Introduction

CHAPTER 1 : INTRODUCTION

INTRODUCTION

At the beginning of the nineteenth century spectroscopic studies of the light emitted and absorbed by atoms and ions showed that particular wavelengths of light associated with atoms of a specific element are unique for that element and that as a result the spectral information must offer some insight into the internal structure of the atom. Towards the end of the nineteenth century the analysis of hydrogen and other simple spectra uncovered some important regularities and systematic trends in the observed wavelengths. Classical models of the atom were inadequate to explain these regularities and trends and it wasn't until 1913 that Bohr's theory of the hydrogen atom, based on Rutherford's nuclear atom and incorporating the ideas of Planck, made some progress towards explaining these observations. However, Bohr's semi-classical theory was not general enough to describe more than the gross features of the simplest one electron atom. It wasn't until the development of quantum mechanics in the middle and late nineteen twenties that progress was made into the understanding of many electron atoms. Certainly, a symbiosis grew between the understanding of atomic structure and development of the principles of quantum theory each allowing further and further of an insight into the other.

Atomic theories deal with the determination of the energy levels of atomic systems and their wave functions. The data generated are needed for the analysis of spectra, the determination of wavelengths and transition probabilities, the calculation of photoionisation cross-sections, impact excitations and ionisation cross-sections etc. Collecting and analysing experimental data allows us to understand the behaviour of physical systems at an atomic level. Quantum mechanics provides us with the theoretical framework and spectroscopy with the experimental means required to interpret complicated spectra in terms of the properties of the source from which they are radiated and the medium in which the source radiation is absorbed. The fundamental quantities determined in this way are important for many areas of research such as astronomy (determination of physical and chemical processes occurring in planets, stars, comets etc.), thermonuclear fusion, materials science and laser physics e.g. X-ray laser research.

In recent years there has been a growing interest specifically in extreme-ultraviolet (XUV) and soft x-ray (SXR) spectroscopy. There are two main reasons for this increase in activity:

1. Work in areas such as inertial confinement fusion [e.g., De Michelis and Mattioli 1984], X-ray laser research [e.g., Jaegle 1987] involve the study of hot ionised matter and the radiation emitted by this matter is predominantly in the extreme-UV and X-ray spectral regions.

2. At VUV (vacuum-ultraviolet) and XUV wavelengths it is possible to excite the outer most-inner-shells in atoms. This results in strong electron correlation effects such as one photon-two electron excitation [Madden & Codling 1965], delayed onset of absorption [Ederer 1964] and giant resonances [Connerade 1978]. Due to the fact that the lifetimes of excited states of inner shell transitions for decay into ion plus one or more electrons is very short, these effects are mainly observed in photoabsorption experiments and this is the reason why there is at present more activity in XUV absorption spectroscopy rather than the experimentally easier emission studies.

As a result of the above many developments have also been made in XUV technology and in particular XUV continuum light sources, normal/grazing incidence spectrometers equipped with high quality optics and detection systems that form an important part of these spectrometers and most recently layered synthetic micro structures or multilayers which provide high normal incidence reflectivity at XUV wavelengths.

Excited species emit radiation over the entire electromagnetic spectrum but in the study of hot, ionised matter the radiation of interest is emitted typically in the VUV to X-ray spectral bands. The radiation emitted is due to a number of physical phenomena and as a result the specific spectroscopic technology used to record such spectra depends on the energy region of interest. Figure 1.1 indicates the different regions of the electromagnetic spectrum and some physical processes which can give rise to the radiation emitted in each band. Also shown are the corresponding wavelength and energy scales involved. Figure 1.2 indicates the wavelength/energy range and nomenclature used in the VUV, XUV and soft X-ray regions of the spectrum which will be of use in the following discussions. The figure is illustrative in nature as the exact division between these electromagnetic bands is often a matter of personal preference.

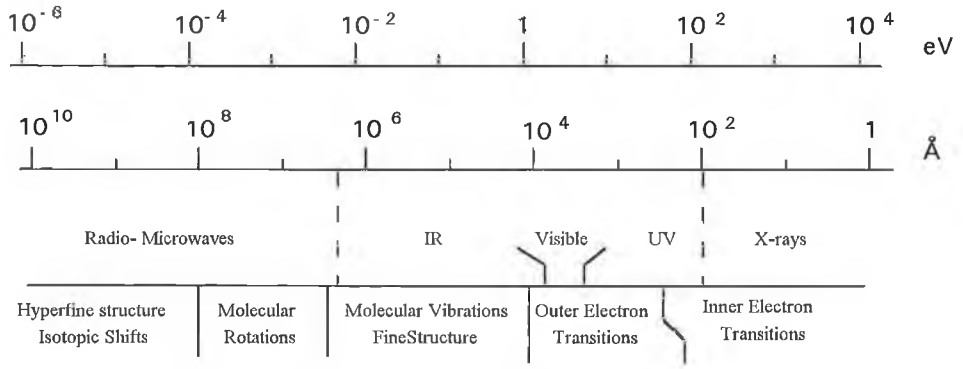

Figure 1.1 Energy ranges and corresponding spectroscopic phenomena [Bransden and Joachim 1985] .

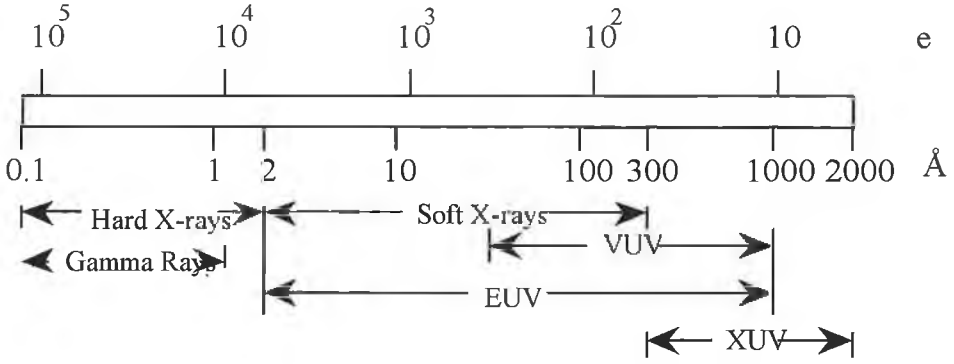

Figure 1.2 The wavelength and photon energy ranges used in the vacuum ultraviolet [Svanberg 1991].

Studies involving hot ionised matter have been greatly enhanced over the last two decades due to developments in the technology of high power laser systems. When the output of a high power (typically Q-switched or mode locked) laser is focused onto a target *in vacuo* a short lived (time scales ~10^{-13} - 10^{-6} sec), high temperature (electron temperature $T_e \sim 10^5$ - 10^8K) and high density (electron density $n_e \sim 10^{19}$ - 10^{24} cm^{-3}) plasma is formed. As many of the plasma parameters are to some extent controllable, the study of laser-produced plasmas (**LPP**) has greatly extended out understanding of hot ionised matter. These studies involve analysis of both radiative [e.g., De Michelis and Mattioli 1984] and particle [e.g., Bonham *et al* 1988, Kephart *et al* 1976, Decosk *et al* 1984] losses from the expanding plasma.

As well as providing a means of studying hot ionised matter laser plasmas have many other scientific and technological applications such as x-ray microscopy [Stead *et al* 1995], high resolution soft x-ray lithography [Frankel *et al* 1987, Turcu *et al* 1995], X-Ray diffraction [He *et al* 1993], Extended X-ray Absorption Fine Structure (EXAFS) studies [Malozzi *et al* 1979, Eason *et al* 1984, Kubiak *et al* 1990], pulsed laser

deposition dynamics [Murakami *et al* 1994] and photoabsorption studies of laser produced plasmas [Costello *et al* 1991].

1.1 LASER PRODUCED PLASMAS: FORMATION AND BASIC PHYSICS

As stated above laser plasmas are produced when the focused beam of a laser interacts with a solid target at irradiances in excess of ~10^8 W cm^{-2}. Laser pulses of such high power are necessarily of short duration due to the limitations on the average power available from conventional pulsed lasers and the laser radiation which reaches the target surface penetrates to only a fraction of a wavelength [Carroll and Kennedy 1981]. The laser radiation penetrating the surface couples strongly to the conduction electrons so that heating, evaporation and ionisation of the target material occur rapidly. The r.m.s electric field **E** in V m^{-1} is related to the laser flux ϕ by the expression $\mathbf{E} = 19.4\ \phi^{1/2}$. So for example if $\phi = 10^{12}$ W cm^{-2} then $\mathbf{E} = 2 \times 10^9$ V m^{-1}, which is of the order of 0.1% of the field experienced by an electron located one Bohr radius from a hydrogen nucleus. Figure 1.3 shows schematically how a laser plasma is created and what happens both at the target and within the plasma.

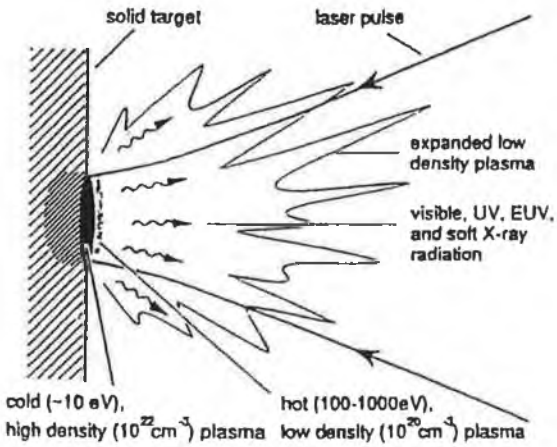

Figure 1.3 Schematic diagram showing how a laser-produced plasma is formed and what happens at the target and within the plasma [Fawcett *et al* 1966].

The leading edge of the focused laser pulse vapourises and ionises material from the surface of the target and creates a low temperature expanding plasma known as the priming plasma. This occurs within the first few cycles of the **E**-field of the laser pulse. After the priming plasma has been formed absorption of the laser radiation usually occurs via inverse Bremsstrahlung. Inverse Bremsstrahlung is a process whereby a photon is absorbed by an electron-atom/ion system resulting in the electron being raised from a lower continuum level to a higher one, thereby increasing the kinetic energy of

the electron. Inverse Bremsstrahlung is the dominant mechanism in the evolution and growth of a LPP. In the early stages of plasma evolution the dominant absorption process is electron-neutral inverse Bremsstrahlung. When sufficient electrons and ions are generated the dominant plasma absorption mechanism makes a transition to electron-ion inverse Bremsstrahlung. The light emitted by a laser plasma results from interactions between electrons and atomic/ionic species and results in radiation of the following types occurring:

Line Radiation is due to the spontaneous decay of an excited atom, ion or molecule (in a bound state) to a lower energy level.

Recombination Radiation (free-bound radiation) occurs when a free electron recombines with an ion. Since the upper level is continuous the spectrum of the emitted radiation is continuous, displaying however the characteristic discontinuities at the wavelengths corresponding to the ionisation energies of bound levels.

Bremsstrahlung (free-free radiation) is emitted, when electrons make transitions between free energy levels in the field of ions. The resulting spectrum is continuous.

For further details on radiative energy transfer processes within laser plasmas refer to [Hughes 1975, Dekker 1989]. For plasmas created by a small table top pulsed laser, typical plasma parameters are as follows :

Laser parameters (specific to D.C.U lab)

Laser type:	Nd:YAG	Ruby	Dye
Energy (joules):	1	1.5	3
Pulse lengths (ns):	12	25	800
Power densities (W cm^{-2})	10^{11} - 10^{12}	10^{11} - 10^{12}	10^{9} -10^{10}
Wavelength	1.06 μm	694.3 nm	340 - 940 nm

Plasma parameters

Electron Temperatures: few eV's - 100 eV

Electron densities: 10^{19} cm^{-3} - 10^{21} cm^{-3}

In the interest of completeness it is noted that for irradiances > 10^{13} W cm^{-2} several new physical effects occur within laser plasmas e.g. stimulated Raman back scatter [Darrow *et al* 1992], hard X-rays with energies up to 1 MeV [Kmetec *et al* 1992], high harmonics of the laser frequency [Macklin *et al* 1993], subpicosecond FIR emission [Hamster *et al* 1993] and MeV electrons produced by laser wake-field acceleration [Modena *et al* 1995]. Although these high irradiances are not applicable to this work , the physics of plasmas produced by such high irradiances are of much current interest and likely to result in many further, novel observations and applications.

1.2 SPECTROSCOPY OF LASER PRODUCED PLASMAS

Laser plasmas have proven to be versatile sources of VUV/XUV line and continuum radiation and have been used in both emission and absorption spectroscopy. Early studies of LPP concentrated on the emission spectra of multiply ionised species [e.g., Fawcett 1984]. The results of these studies combined with *ab-initio*/scaled multiconfiguration atomic structure calculations have produced a great deal of basic atomic data along with a greater understanding of the effects of increasing ionisation on atomic structure. Absorption studies, in particular XUV photoabsorption experiments, provide important information on inner-shell and double electron excitations and also on photoionisation continua. The implementation of a photoabsorption experiment has two basic requirements. The first is the production of an absorbing medium with sufficient densities of atomic or ionised species to allow the recording of an absorption spectrum. The second requirement is to have a smooth, intense and reproducible continuum (backlighting) radiation source. The radiation from this source being passed through the absorbing medium.

Figure 1.4 below indicates schematically how a photoabsorption experiment is carried out and also shows some of the different methods and techniques used in these experiments.

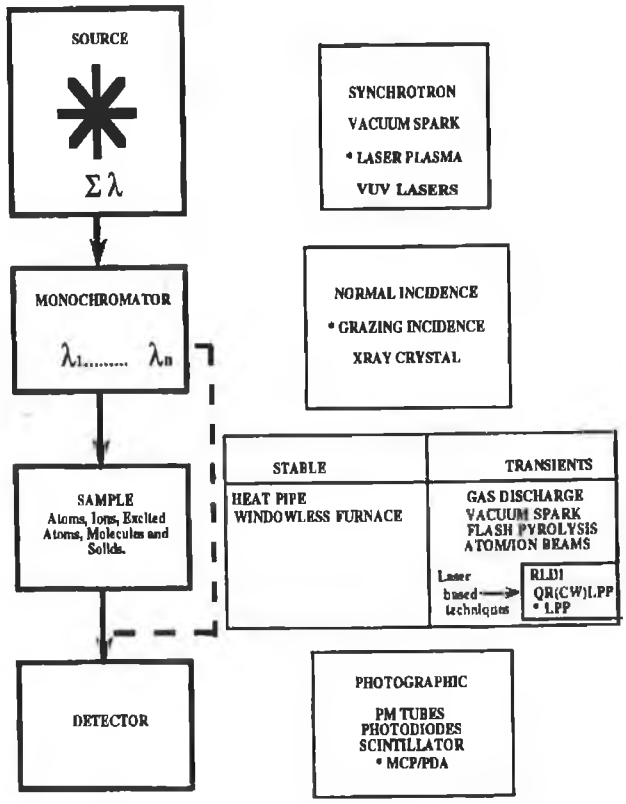

Figure 1.4 Schematic representation of a VUV/XUV photoabsorption experiment. Shown are the different experimental stages and the alternatives approaches for each stage.

There have been a number of inventive approaches to the generation of absorbing vapours and plasmas such as flash pyrolysis [Tondello 1972] , Resonant Laser Driven Ionisation - RLDI [Lucatorto *et al* 1980] and laser plasmas [Costello *et al* 1991 and references therein]. Flash pyrolysis systems use powdered samples of the material to be studied. These samples are placed inside quartz or glass tubes surrounded by a helical flash lamp. The energy released by the flash lamp produces neutral and singly ionised atoms within the tube which can then be used along with a synchronised pulsed continuum source to measure the absorption spectrum of these species [Roig 1975, Cantu et al 1977]. RLDI is another effective and widely used technique for the production of absorbing atomic and ionic columns. A singly ionised column is produced by the interaction of a high power dye laser beam (tuned to an atomic resonance line) with a vapour contained in a heat pipe [McIlrath *et al* 1986]. It is also possible to produce doubly ionised species by the use of a second time synchronised dye laser tuned to a resonance line of the singly ionised column [Lucatorto *et al* 1981]. This technique has been used to examine a number of different ions e.g. Ba and Na [Lucatorto *et al* 1980], Xe, Cs^{+} and Ba^{++} [Hill *et al* 1982 and 1987] and also, as one of its major successes, provide an understanding of the collapse of the 4*f* wave function in Ba with

increasing ionisation [Lucatorto *et al* 1981]. The limitations of the two previous techniques are that they only provide ionic species with a low degree of ionisation (singly and doubly charged ions) and in order to study either refractory metal vapours or ion stages greater than 2+ RLDI is severely limited by restrictions on the experimental set-ups (e.g. vapour pressures in heat pipes and dye lasers tuned to wavelengths in the UV). A technique which overcomes these difficulties and which allows the recording of photoabsorption spectra of multiply ionised species is the Dual Laser Plasma (DLP) technique in which both the absorbing and backlighting plasmas are produced by the interaction of high-power laser beams with suitable solid targets.

Before the advent of laser plasma continua, the two most popular XUV light sources were the BRV vacuum spark and synchrotron radiation. The triggered vacuum spark, [Ballofet *et al* 1961], provides continuum radiation in the 80 to 500 Å range and has been used extensively in the production of photoabsorption spectra. It is a three-electrode discharge device with continuum emission from a plasma created at the tip of an electrode. Mehlman and Esteva [1974,1969] using a pair of crossed BRV sparks in order to generate both the continuum and absorbing plasmas, obtained the VUV and XUV absorption spectra of Be^+ and Mg^+. A problem with using this type of source is that in order to move to shorter wavelength radiation you must use higher discharge currents which places limitations on the source repetition rate and electrode lifetimes. Further this source must be operated in a high vacuum environment.

Synchrotron radiation has also been used also as a continuum radiation source for many years in photoabsorption studies [see e.g., Wuillemmier 1994]. It has a number of advantages in that the radiation is intense, free from lines and provides an output whose energy distribution can be calculated theoretically. Another very important property of this radiation in for example solid-state studies, is the fact that the radiation has strong polarisation properties. Using synchrotron radiation in conjunction with an ion beam, West and his collaborators obtained absolute photoionisation and photoabsorption cross-sections for a number of different ions including K^+ [Lyon *et al* 1986] and Ba^+ [Peart *et al* 1987]. Some of the disadvantages of this source are that it is expensive to operate and also you must bring your experiments to the machine.

1.2.1 LASER PLASMA CONTINUUM SOURCES

Development of laser plasma continuum sources has increased in recent years due to a need for convenient small scale sources to act as alternatives to the more conventional

devices such as synchrotron and BRV spark. These alternative sources tend to be either experimentally difficult to use, very expensive, non-portable or have limited spectral coverage.

[Carroll *et al* 1978] carried out studies of the continuum emission from a number of rare earth metals and higher Z materials. In particular, they found that the emission from elements samarium (Z=62) to ytterbium (Z=70) was of high intensity and almost exclusively continuum in nature apart from a few discrete line features. Further the continuum radiation was emitted over a broad wavelength range 40 - 2000 Å. These results stimulated further measurements [Carroll *et al* 1980,1983] of the time-resolved and time-integrated emissions from the rare earth metals with a view to establishing these continuum sources as low cost "table top" alternatives to synchrotron sources for photoabsorption studies in the VUV and XUV regions. A number of high resolution studies [Orth *et al* 1986, Gohil *et al* 1986] examining the uniformity of these laser plasma continua have been under taken. These have shown that using a high resolution grazing incidence spectrograph these spectra are true continua down to a resolution of 4 x 10^{-3} nm. In a contemporaneous experiment [Bridges *et al* 1986] showed that there was a progression from mainly line emission for low-Z plasmas to pure continuum emission for the rare earths (Figure 1.5). The origin of laser-plasma rare earth continua is discussed in detail by [O'Sullivan 1983] and in the interests of brevity will not be discussed here.

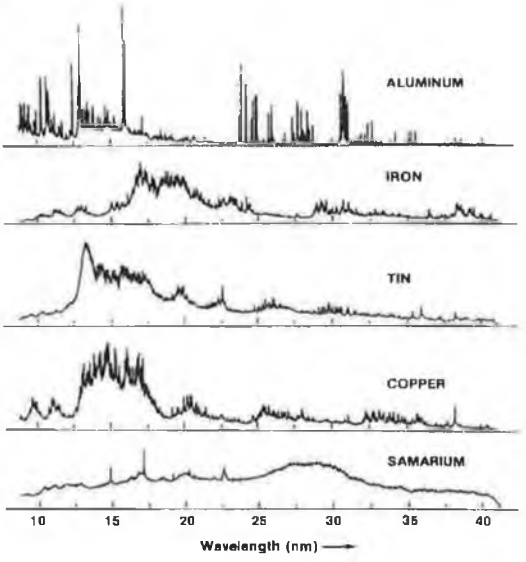

Figure 1.5 Spectra showing the transition from mainly line emission for low Z target to pure continuum for the rare earths. The transition from discrete to continuum emission in the rare earths is apparent [Bridges *et al* 1986].

Laser plasma continuum sources are advantageous when compared with other continuum sources for a number of reasons. These are highlighted as follows:

Laser produced plasma continuum light sources

- have good shot to shot reproducibility.
- are insensitive to ambient pressure variations.
- are of small almost point like spatial extent. This last property is important for experiments requiring a source of continuum which provides spatial resolution.
- emit an intense burst of XUV radiation which has very high instantaneous brightness at least comparable to the flux per pulse observed from other sources (e.g. synchrotron, BRV spark e.g. [Biijerk *et al* 1991, Kuhne *et al* 1977].
- have pulse widths comparable to the length of the laser pulse.
- are relatively inexpensive and easy to set up.
- exhibit conditions that are controllable/selectable by simple variations of experimental parameters e.g. laser energy, pulse length, wavelength, focusing conditions and choice of target material.
- have a wide spectral coverage (30 -> 2000 Å) where the lower bound of this range is set by the target irradiance
- are free from undesirable line emission.

1.2.2 LASER PLASMA PHOTOABSORPTION EXPERIMENTS AND DEVELOPMENTS

In the following section a brief discussion of a Dual Laser-Plasma Photoabsorption (DLPP) technique [Costello *et al* 1991] in which both the absorbing and backlighting plasmas are formed by a pair of laser pulses focused onto suitable target materials.

The first two laser plasma experiment carried out was by Carillion *et al* [1970]. In this experiment they measured the absorption by one aluminium laser-plasma of the flux emitted by a second Al plasma. These authors found that although the emission was dominated by discrete line structure there were a small number of narrow wavelength intervals (of width typically ~ 10 Å) which contained predominantly Bremsstrahlung continuum emission only. They used this fact to obtain absorption spectra of an aluminium plasma at a small number of single wavelengths (Figure 1.6).

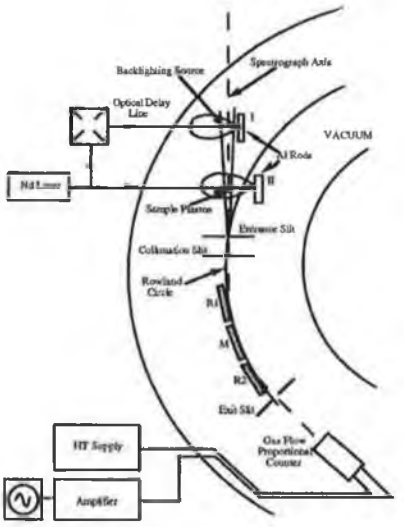

1.6 (a)

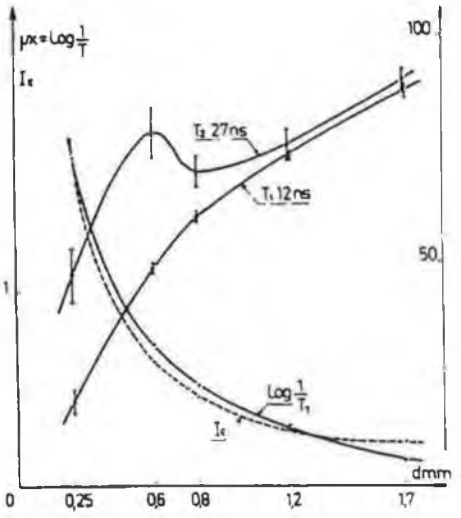

1.6 (b)

Figure 1.6 (a) Schematic diagram showing the experimental set-up used by Carillion *et al* 1970 to record the absorption by an Al laser-plasma of the flux emitted by a second Al plasma. (b) Transmittance (T) spectrum at 98 Å showing that at distances ~0.3 mm from the target surface absorption is due to both inverse Bremstrahlung and photoionisation of aluminium ions (Al^{3+}) present in the cool outer region of the recombining plasma [Carillion *et al* 1970].

Further, it was observed that by varying the time between the generation of the absorbing and backlighting plasmas (delays used ~ 12 - 27 ns) and scanning the continuum source through the absorbing plasma they could identify different absorption mechanisms at different stages of plasma evolution. For short inter-plasma time delays the absorption decreased smoothly as you moved away from the absorbing plasma core indicating inverse Bremsstrahlung as the main absorption mechanism. For longer delays there was a modulation of the total absorption at distances ~ 0.3 mm from the plasma

core. This was explained by the fact that as the plasma cooled and expanded there were ions of low enough charge to allow photoionisation to occur so that absorption of the backlighting continuum emission could be attributed to both a combination of inverse Bremsstrahlung and photoionisation. This experiment showed that laser plasmas could be used as sources of continuum for absorption experiments and also provide suitable absorbing columns of ions and neutral species. Also by variation of the time delay between absorbing and backlighting plasmas it possible to obtain time and space resolved spectra. A limitation to this experiment was that it could not be used for photoabsorption studies over a broad wavelength range.

Carroll *et al* [1977] used the continuum emission from a tungsten laser plasma to produce the spatially resolved absorption spectrum of singly ionised lithium Li^+. The purpose of the experiment was to observe the helium like doubly excited states of Li^+ and to determine their energies and profile parameters. The absorbing lithium plasma and backlighting tungsten plasma were generated using a single Q-switched ruby laser (Fig. 1.7).

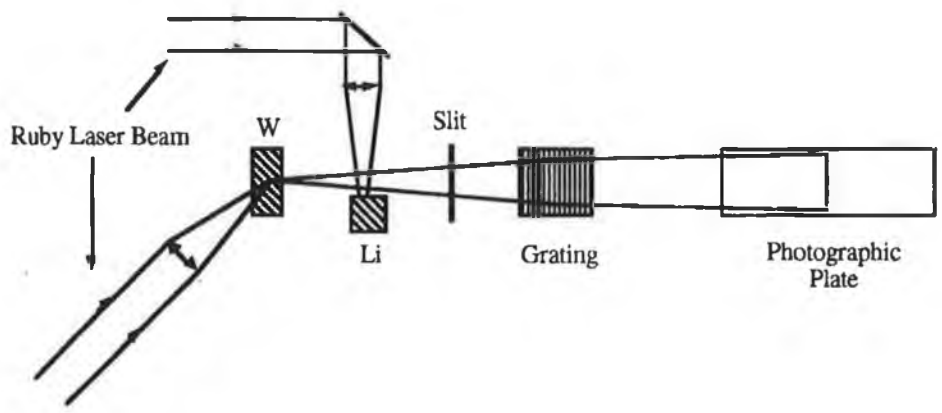

Figure 1.7 Dual Laser-Plasma (DLP) experimental set-up used by Carroll and Kennedy [1977] to record the photoabsorption spectra of Li^+. The tungsten target provided a point like source of XUV continuum radiation, which allowed the recording of spatially resolved spectra.

Tungsten was used as a continuum target based on observations made by Ehler *et al* [1966] who noticed the predominance of continuum emission in the V-UV spectral region above 400 Å. Carroll and Kennedy also noted in this experiment the importance of beam focusing conditions in the production of the ionic species to be studied. Also alignment of the absorbing and continuum sources with respect to one another and the spectrometer axis was stated as crucial to the success of the experiment. Photographic

plates were used to record the spectra and microdensiometer traces were used in the determination of profile parameters q and τ [Fano 1961].

The DLP technique was adopted by [Jannitti *et al* 1984] and used in the photo absorption studies of low-Z ions. The experimental procedure and set-up (Figure 1.8) differed from previous DLP experiments [Carroll *et al* 1977] in a number of ways which provided a number of advantages.

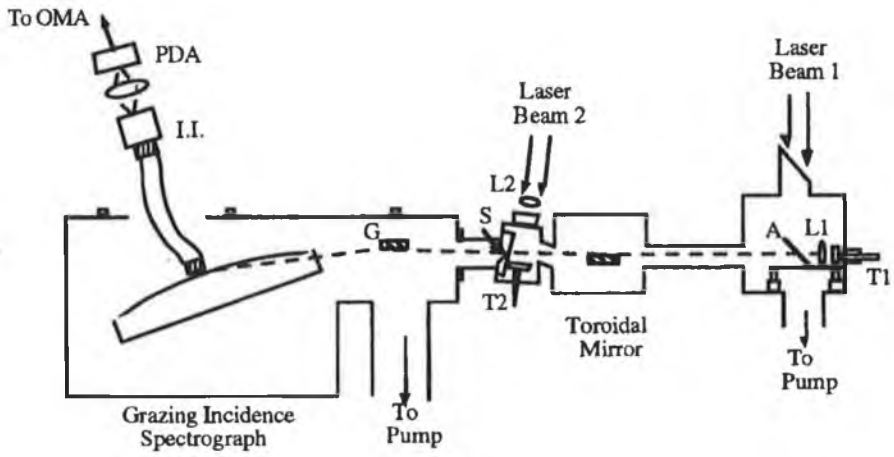

Figure 1.8 DLP set-up used by [Janitti *et al* 1984]. The set-up is similar to that of [Carroll *et al* 1977] with the addition of a XUV detection system consisting of a scintillator coated fiber-optic face plate coincident with the Rowland circle and also a toroidal mirror, which improves the coupling of the continuum radiation through the absorbing plasma and onto the spectrometer slit.

The introduction of toroidal optics [Rense and Violett 1959, Tondello 1979] improved the flux coupling efficiency and spectral imaging capabilities of the VUV/XUV grazing incidence spectrometer. The effective source brightness was increased by viewing the laser plasma straight on through a small hole in the focusing lens. Another major improvement made to the DLP method in this experiment was the fitting of an VUV/XUV optical multichannel analyser (OMA) to the spectrometer. This detection system consisted of a scintillator coated face plate coincident with the Rowland circle of a vacuum spectrometer and movable along the curve so that a large spectral region could be scanned. The scintillator converts the XUV photons to visible light for detection via a fibre-optic image guide lens coupled to a intensified photodiode array. This system allowed the direct measurement of relative photoabsorption cross-sections, a process which with photographic detection systems proved very time consuming. The fact that the recorded data could be stored in direct digital format permitted deconvolution

(Chapters 3 and 4 discuss this topic further) and other procedures to be applied to the digitised data to improve the spectral resolution. To improve detector spatial resolution (and hence spectral resolution) [Cromer *et al* 1985] fitted a special resolution enhanced channel electron multiplier array (CEMA - see Chapter 2) to the front end of the detector. These CEMA devices consist of an array of miniature photomultiplier tubes which are directly sensitive to VUV/XUV photons.

The capabilities of the DLP technique were further extended by the use of two temporally synchronised lasers by Carroll and Costello [1986]. This approach allowed increased power densities on targets and variable inter-plasma time delay (Δt, 250 ns $\rightarrow$ 100 μs). The system allowed the study of absorption spectra of highly refractory atomic/ionic species and the production of time resolved absorption spectra of laser-produced plasmas which provides important information about the dynamics of laser plasmas.

A variation of the DLP method has been used by Balmer and his co-workers [Balmer *et al* 1989] to measure photoabsorption spectra of highly ionised atoms in the soft X-ray spectral range (1-10 Å). The experimental arrangement is shown in Figure 1.9.

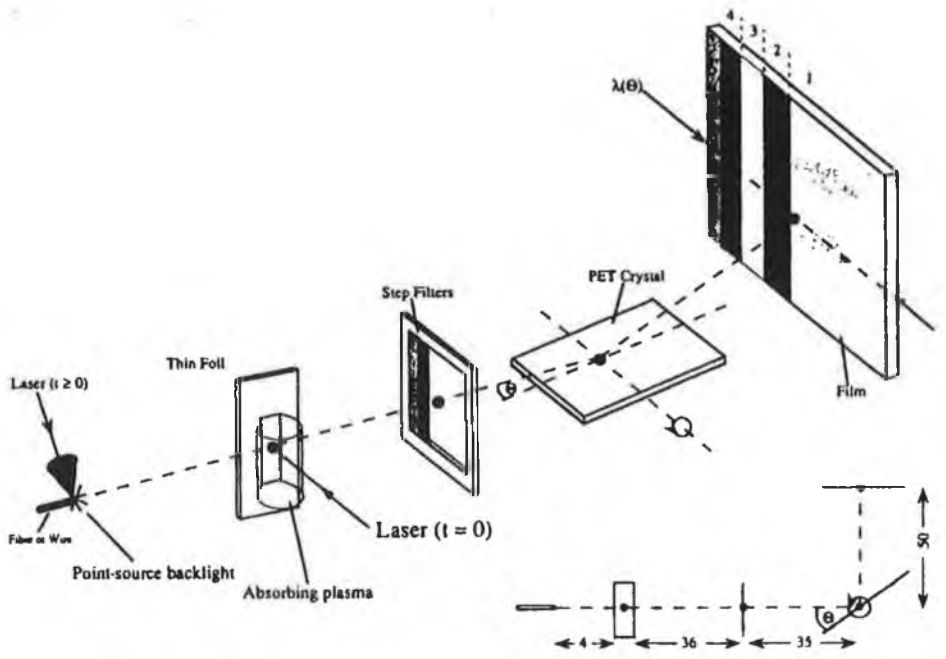

Figure 1.9 Experimental set-up for point projection spectroscopy as used by Balmer *et al* [1989]. This set-up allowed the study of soft X-ray absorption spectra (1 - 10 Å) of highly ionised ions.

The absorbing plasma is produced by irradiation with a pulse of 1 ns duration (8-25 J) focused onto a thin aluminium foil. To produce the backlighting plasma a thin wire ~ 10 mm of either tungsten or Yb coated carbon fiber is irradiated with a short 600 ps pulse which yields a quasi-point soft x-ray source. The transmitted X-ray radiation passes through the absorbing plasma and is dispersed by a crystal spectrometer and recorded on film. The technique is known as point projection absorption spectroscopy. It provides quantitative data on the photoionisation cross-sections of highly charged ions. This particular method has been used to study bound-bound transitions in hydrogen-like (Al^{+12}) and helium-like (Al^{+11}) aluminium ions including satellite as well as resonance line features. The experiments also provide a quantitative measure of ion ground state populations which are of importance in the study of plasma media for e.g., XUV laser research.

For a more complete review of XUV absorption spectroscopy with laser plasmas and the different experimental techniques used refer to the article by Costello *et al* [1991] and references therein.

1.2.3 EXPERIMENTAL DIFFICULTIES IN VUV/XUV SPECTROSCOPY

In the measurement of spectra emitted from (and absorbed by) laser-produced plasmas there are many experimental problems which must be overcome. The fact that air is opaque to VUV/XUV radiation means that spectrometers must be evacuated. Also, below the LiF 1050Å cut-off [Samson 1967], there is a lack of materials which transmit VUV/XUV radiation. This fact has led to the development of some novel approaches for confining gases, vapours or plasmas, such as windowless furnaces [Garton *et al* 1969] and flash pyrolysis [Tondello 1972]. Further it has necessitated the use of reflective rather than conventional transmissive optics.

The main problem with grazing-incidence spectrometers is the severe astigmatism entailed (see [Samson 1967] for a discussion of this point). By using a combination of a toroidal mirror and a grating one can compensate for astigmatic losses [e.g., Rense and Violett 1959, Tondello 1979]. The need to go to grazing incidence at XUV wavelengths is necessitated by the reflective properties of gratings and mirrors. At wavelengths below 100 nm the reflectivity of materials is $\leq$ 30 % for nearly all materials at normal incidence (viewed straight on) and below wavelengths ~ 30 nm this value drops to only at few percent. This is the reason why normal incidence spectrometers usually operate at wavelengths longer than 30 nm and also, to minimise the number of reflections, use only

a single dispersing and focusing element e.g. a concave grating. On the other hand, at large angles of incidence total reflection with a reflectance approaching unity occurs above a critical angle, and this property is utilised in XUV spectrometers, where the radiation is incident on the grating at grazing angles of less than a few degrees.

1.3 SPECTROSCOPIC DETECTION SYSTEMS

Many different spectroscopic instruments for studies at XUV wavelengths have been used (see [Samson 1967] for a review). Historically the detection systems on these instruments can be divided into two main types: photographic and photoelectric. Photographic instruments, using film/plates as the detection media, have the advantage of image storing capability. They permit the recording of a very large amount of data with a single exposure; thus permanent records are made for future reference. This method of recording effectively allows the multiplexing of data over a broad spectral region onto one recording element. A common type of photographic plate used in VUV/XUV studies is the Eastman Kodak SWR (short wavelength radiation) type [Burton *et al* 1973]. Photographic recording also has a number of major disadvantages. The sensitivity is considerably lower than that of a photoelectric detector; at UV wavelengths the quantum efficiency is of the order of ~ 1% that of a photoelectric detector (e.g., microchannel plate - MCP or VUV sensitive photomultiplier tube). Also the response is non-linear as a function of the incident energy which makes photometric calibration a difficult and a time-consuming process. Another problem is the fact the data stored on plates is not electrical in character so that the measurement of information recorded must be carried out using a device called a microdensiometer which is a cumbersome and laborious process.

Photoelectric instruments, on the other hand, have a greater stability of response and provide a linear output as a function of the incident energy. The photomultiplier tube (PMT) is one such type of detector. It has a fast response time (better than 5 ns typically), high sensitivity ($> 10^3$ A/W typical), linear response and wide dynamic range. However at any one instant it can provide spectral information at one single wavelength (or averaged over a narrow wavelength interval). In order to record information over a broad spectral region you must use a scanning monochromator and sequentially illuminate the detector. This can lead to problems in the measurement of absolute/relative intensities for unstable sources. Another problem with a PMT is its dark current. Even when there is no radiation incident on the detector there is still a

background signal present. This problem can be minimised by detector cooling and also by the suitable choice of photocathode material.

Over the last 15 years or so array detectors have been developed to act as alternatives to photographic and single-channel PMT type detectors. They offer the advantages of electronic read-out of a PMT along with the spatial resolution and multiplexing characteristics of a photographic plate. These detectors are solid state devices, consisting of a large number of light sensitive elements (usually 512 or 1024) closely arranged in a row. Each individual element represents one channel of an optical multichannel analyser (OMA), in which a count proportional to the intensity of the incident radiation on the individual element is stored. An OMA is a electro-optical signal-processing/readout system which when combined with an array detector allows real-time detection along with image processing capabilities. Array detectors are placed in the focal plane of the spectrometer and with geometry of 1024 photodiodes, 25 mm diode separation and 2.5 mm height form effectively a strip of electronic 'photographic' plate. To improve the light sensitivity of these devices the array detector is placed behind an image intensifier device such as a microchannel plate (MCP, see Chapter 2). This device produces bunches of electrons that are spatially arranged corresponding to the original radiation spectrum. These electron bunches impinge on a phosphorescent material. The light thus produced is then transferred to the diode array with the spatial information retained via fibre-optic coupling device. A more complete description of such a detector assembly is given in Chapter 2. The above type of diode array detector was initially developed for plasma impurity analysis in tokamak fusion devices [Fonck *et al* 1982, Hodge *et al* 1984, Schwob *et al* 1983] but has become widely used in laboratory spectroscopy. The main benefit of these detectors is their capability to record simultaneously and digitally acquire whole spectra. The speed and ease of data acquisition and processing with these detectors has meant they are attractive alternatives to photographic and PMT detection systems.

1.4 SPECTROSCOPIC IMAGE ENHANCEMENT

Spectroscopic imaging systems use either photographic (film, plates) or photoelectric (PMT's, Diode Arrays) detection for image sampling and recording and thus set a limit on the highest spatial frequency which can be recorded. Further the optical elements used to produce the images (lenses, mirrors, stops, gratings, etc.) degrade the quality of the image formed. The images are therefore instrumentally smeared with a resultant loss of spatial resolution. It is possible, with a knowledge of

the specific way in which the image is degraded, (i.e., the instrument function) to at least partially restore the image and so gain back some of the lost resolution. The potential resolution gain, of the order of three or so (depending on the signal to noise ratio in the data) along with the use of cheap, powerful desktop computers make image enhancement (deconvolution) techniques worthy of detailed investigation. Implementation of different deconvolution techniques and a comparison of their results would provide a greater understanding of the resolution enhancement capability of individual techniques and allow examination of their sensitivity to signal to noise ratio.

The work described in this thesis involved the development of a software package for the control and data acquisition of a customised soft X-ray/XUV/VUV spectrometer equipped with an MCP/self scanning diode array detector. The control and data acquisition was carried out using an Optical Multichannel Analyser (OMA) system. Also investigations of the use of image enhancement (deconvolution) techniques to improve the resolution of spectra recorded using the spectrometer were carried out. This work was carried out as part of the design and construction of a multi high power laser facility for the production and study of dense laser-produced plasmas by spectroscopic means [Kennedy *et al* 1994].

Chapter 2 describes the total spectrometer system (spectrometer, detector etc.) used in this thesis, giving details related to its mechanical, optical and electronic characteristics. It also includes details of the software and interfacing equipment used as part of the experimental set-up used. The performance of the complete set up is demonstrated by showing a series of emission (and absorption) spectra of laser plasmas. Chapter 3 presents the theory explaining three major deconvolution techniques i.e. Linear/Filtered Fourier [Michaelian and Friesen 1987], Constrained Non-Linear [Blass and Hasley 1981] and Maximum Likelihood [Frieden 1983] . Chapter 4 presents results on the application of these deconvolution methods to the enhancement of VUV/XUV emission and absorption spectra. A comparison of the different techniques and their relative merits and downfalls is given. Chapter 5 outlines the conclusions and future work.

REFERENCES

Ballofet, G., Romand, J. and Voldar, B., C.R. Acad. Sci. **252**, 4139 (1961).

Balmer, J., Lewis, C.L.S., Corbett, R.E., Robertson, E., O'Neill, D., Lamb, M.J., Saadat, S., O'Neill, D., Kilkenny, J.D., Back, C.A., Lee, R.W., Phys. Rev. A., **40**, 330 (1989).

Bijkerk, F. and Shevelko, A.P., SPIE Vol. **1503** Excimer Lasers and Applications III (1991).

Blass, W.E. and Hasley, G.W., "Deconvolution of Absorption Spectra", Academic Press (1981).

Bonham R.W., Quattlebaum J.C, Spectroscopy **3**, 42 (1988)

Bransden and Joachim, "The Physics of Atoms and Molecules", 1985.

Bridges, J.M., Cromer, C.L. and McIlrath, T.J.,Appl. Opt. **25**, 2208 (1986).

Burton, W.M., Hatter, A.T., Ridgely, A., Appl. Opt. **8**, 1851 (1973).

Cantu, A.M., Parkinson, W. H., Tondello, G. and Tozzi, G.P., J. Opt. Soc. Amer. **67**, 1030 (1977).

Carillion, A., Jaegle, P. and Dhez., Phys. Rev. Lett. **25**, 140 (1970).

Carroll, P.K. and Costello, J.T., Phys. Rev. Lett. **57**, 1581 (1986).

Carroll, P.K. and Kennedy, E.T., Phys. Rev. Lett. **38**, 1068 (1977).

Carroll, P.K., and Kennedy, E.T., Contemp. Phys., **22**, 61 (1981).

Carroll, P.K., Kennedy, E.T. and O'Sullivan, G., IEEE. J. Quant Electron. **QE-19**,1807 (1983).

Carroll, P.K., Kennedy, E.T. and O'Sullivan, G., Opt. Lett. **2**. 72 (1978).

Carroll, P.K., Kennedy, E.T. and O'Sullivan, G., Appl. Opt. **19**, 1454 (1980).

Connerade, J.P., "Giant Resonances in Atoms, Molecules and Solids", (Edited by J.P Connerade, J.M., Esteva, and R.C. Karnatak), NATO ASI Series B: Physics Vol. 151, P 3 (1987).

Costello, J.T., Mosnier, J.P., Kennedy, E.T., Carroll, P.K. and O'Sullivan, G., "X-UV Absorption Spectroscopy with Laser-Produced Plasmas: A Review", Phys. Scr. **T34**, 77 (1991).

Cromer, C.L., Bridges, J.M, Roberts, J.R. and Lucatorto, T.B., Appl. Opt. **24**, 2996 (1985).

Darrow, C.B., Coverdale, C., Perry, M.D., Mori, W.B., Clayton, C., Marsh, K., Joshi, C., Phys. Rev. Lett. **69**, 442 (1992).

Decoste, R., Kieffer, J.C., Pascabe, D., Pepin, H., Appl. Phys. Lett., **45**, 229 (1984)

Dekker, M., Chapters 1 and 2 and references therein., "Laser-Induced Plasmas and Applications", (Edited by Radziemski, L.J. and Cremers, D.A.), (1989).

DeMichelis, C. and Mattioli, M., Rep. Prog. Phys. **47**, 1233 (1984).

Eason, R.W, Bradley, D.K., Kilkenny, J.D. and Greaves, G.N., J. Phys. C: Solid State Phys. **17**, 5067 (1984).

Ederer, D.L., Phys. Rev. Lett. **13**, 760 (1964).
Ehler, A.W. and Weisler, G.L., Appl. Phys. Lett. **8**, 89 (1966).
Fano, U., Phys. Rev. **124** 1866 (1961).
Fawcett, B.C., J. Opt. Soc. Amer. **B1**. 195 (1984).
Fawcett, B.C., Gabriel, A.H., Irons. F.E., Peacock, N.J., Saunders, P.A.H, Proc. Phys. Soc., **88** 1051 (1966)
Fonck, R.J., Ramsey, A.T. and Yelle, R.V., Appl. Opt., **21**, 2115 (1982).
Frankel, R.D., Drumheller, J.P., Kaplan, A.S. and Lubin, M.J., Proc. of Microelectronics Seminar Interface 86, Eastman Kodak, p. 82 (1987).
Frieden, B.R, J. Opt. Soc. Amer. **73**, 927 (1983).
Garton, W.R.S, Connerade, J.P., Mansfield, M.W.D. and Wheaton, J.E., Appl.Opt. **8**, 919, (1969).
Gohil, P., Kaufman, V. and McIlrath T.J., Appl. Opt. **25**, 2039 (1986).
Hamster, H., Sullivann, A., Gordon, S., White, W., Falcone, R.W., Phys. Rev. Lett. **71**, 2725, (1993).
He, H., Wark, J.S., RAL Annual Report 93-031, 45 (1993)
Hodge, W.L., Stratton, B.C. and Moos, H.W, Rev. Sci. Instrum. **55**, 16 (1984).
Hughes, T.P., Plasmas and Laser Light, Bristol:Adam Hilger (1975).
Jaegle, P., J. Physique. Colloq. **C9**, C9-323, Supplement au n^{o} 12, Tome 58 (1987).
Jannitti, E., Nicolosi, P. and Tondello, G., Opt. Commun. **50**. 225 (1984).
Jannitti, E., Nicolosi, P. and Tondello, G., Physica. **124C** 139 (1984).
Kephart, J.F., Giovanelli, D.V., Williams, A.H., J. Appl. Phys. **47**, 2907 (1976)
Kmetec, J.D., Gordon III, C.L., Macklin, J.J., Lemoff, B.E., Brown, G.S., Harris, S.E., Phys. Rev. Lett. **68**, 1527 (1992).
Kubiak, G.D., Outka, D.A., Rohlfing, C.M., Zeigler, J.M., Windt, D.L., Waskiewicz, W.K., J. Vac. Sci. Technol. B. **8**, 1643 (1990).
Kuhne, M. and Kohl, J., Appl. Opt. **16**, 1786 (1977)
Lucatorto, T.B. and McIlrath, T.J., Appl. Opt. **19**, 3948 (1980)
Lucatorto, T.B., McIlrath, T.J., Sugar, J. and Younger, S.M., Phys. Rev. Lett. **47**, 1124 (1981).
Lyon, I.C., Peart, B., Dolder, K. and West, J.B., J. Phys. **B19.**, 4137 (1986).
Macklin, J.J., Kmetec, J.D., Gordon III, C.L., Phys. Rev. Lett. **70**, 766 (1993).
Madden, R.P. and Codling, K., Astrophys. J. **141**, 364 (1965).
Malozzi, P.J., Schwerzel, R.E., Epstein, H.M. and Campbell, B.E., "Laser EXAFS: Laboratory EXAFS with a nanosecond pulse of laser-produced x-rays", Science, **206**, 353 (1979).

McIlrath, T.J., Sugar, J., Kaufman, V., Cooper, D. and Hill III, W.T., J. Opt. Soc. **B3**, 398 (1986).
Mehlman, G. and Esteva, J.M., Astrophys. J. **157**, 945 (1969).
Mehlman, G., and Esteva, J.M. , Astrophys, J. **188**, 191 (1974).
Michaelian, K.H. and Friesen, W.I., Appl. Spec. **42**, 1538 (1987).
Modena, A., Najmudin, Z., Dangor, A.E., Clayton, C.E., Marsh, K.A., Joshi, C., Malka, V., Darrow, C.B., Danson, C., Neely, D., Walsh, F.N., Nature, **377**, 606 (1995).
Murakami, K., Ohyanagi, T., Miyashita, A., Yoda, O., AIP Conf. Proc. **288**, 375 (1994).
O'Sullivan, G., J. Phys. **B16**, 3291 (1983).
Orth, F.B., Ueda, K., McIlrath, T.J. and Ginter, M.L., Appl. Opt. **25**, 2215 (1986).
Peart, B., Lyon, I.C., *J. Phys. B.* **20** 673 (1987)
Rense, W.A. and Violett, T., J. Opt. Soc. Am. **49**, 139 (1959).
Roig, R.A., and Tondello, G., J. Opt. Soc. Amer. **65**, 829 (1975).
Samson, J.A.R., "Techniques of Vacuum Ultraviolet Spectroscopy",Wiley & Son (1967)
Svanberg, S., "Atomic and Molecular Spectroscopy", Springer-Verlag 1991.
Schwob, J.L., Finkenthal, M. and Suckewer, S., Ann. Isr. Phys. Soc. **6**, 54 (1983).
Stead, A. D., Cotton, R.A., Goode, J.A., Duckett, J.G., Page, A.M., Ford, T.W., J. X-Ray Sci & Technol. **5**, 52-64, 1995.
Tondello, G., Astrophys. J. **172**, 771 (1972).
Tondello, G., Optica Acta, **26**, 357 (1979).
Turcu, I.C.E., Reeves, C.M., Stevenson, J.T.M., Ross, A.W.S., Gundlach, A.M., Prewett, P., Anastasi, P., Koek, B., Mitchell, P., Lake, P. Microelectronic Engineering **27**, 295 (1995)
Wuillemmier, F.J., "New Directions with Third-Generation Soft X-Ray Synchrotron Radiation Sources", (eds. A.S. Schlachter and F.J. Wuilleumier), Kluwer Academic Publishers, 47-102 (1994)

Chapter 2

Experimental

CHAPTER 2 : EXPERIMENTAL

2.1 INTRODUCTION

The current chapter describes the main experimental system used to obtain spectral data presented in the thesis. The main aim is to demonstrate clearly the integration of grazing incidence spectrometer with array detector, lasers and software resulting in a complete experimental system for the study of emission and absorption spectroscopy of laser produced plasmas. The final section of the chapter outlines some of the measurements done to illustrate the performance of the experimental set-up. These tests include single shot sensitivity, spectral resolution and noise.

2.2 MULTILASER PLASMA SPECTROMETER SYSTEM

The experimental set-up outlined below was developed to perform photoabsorption studies of the XUV region of the electromagnetic spectrum. To date it has been applied to the study of photoabsorption by plasmas, atoms, ions, excited atoms and ions, gases and solids [Kennedy *et al* 1994]. The system can also be used to look at emission spectra. The overall layout of the apparatus used is shown schematically in Figure 2.1.

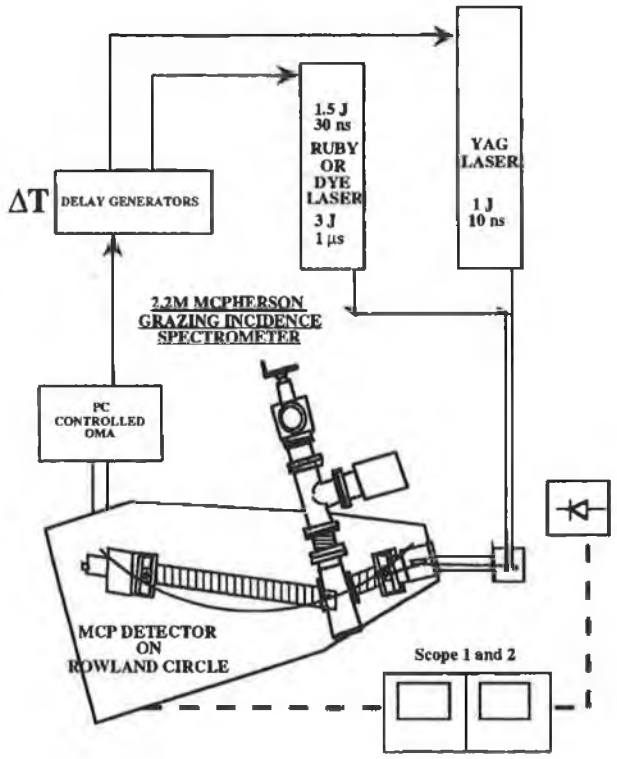

Figure 2.1 Schematic showing general features of the DLP experimental set-up.

The experimental set-up shown above is based on the DLPP (Dual Laser Plasma Photoabsorption) technique [Costello *et al* 1991 and references within] and permits the measurement of both space and time resolved spectra of laser produced plasmas .

Any photoabsorption experiment has four main elements :

- a source of continuum emission
- a spectrometer capable of examining the spectral region of interest
- a sample
- a detector to record the light transmitted through the sample.

The experimental set-up for an emission experiment is very similar except no sample cell is required and the source of radiation is often a line emission source (Aluminium Oxide) rather than a continuum source (Tungsten or Tantalum).

2.2.1 DUAL LASER PLASMA EXPERIMENT

A schematic diagram of the dual laser plasma photoabsorption experiment is shown in Figure 2.1. The capability of this system to perform photoabsorption studies of neutral, excited and ionic species is achieved through the time synchronisation of two (or more) pulsed laser systems incorporated in the set-up.

The absorbing column is produced by the ablation of spectroscopically pure targets *in vacuo* by either a flash pumped dye laser (~3 J in 1 μs) or by a Q-Switched ruby laser (~ 1.5 J in 30 ns) focused in either point or line geometry by a spherical or cylindrical lens respectively. The radiation from the emitting plasma passes through the laser generated absorbing column and is collected by a toroidal mirror which efficiently couples the light into a 2.2 metre grazing incidence spectrometer. The XUV light is dispersed into its constituent wavelengths along the Rowland circle of the spectrometer. The spectrometer is equipped with a Micro Channel Plate (MCP) image intensifier, the output of which is proximity focused by means of a fibre optic face plate, onto a self scanning photodiode array (PDA) detector . After each laser shot the video signal from the detector is displayed on a digitising oscilloscope (HP54501A), thereby permitting the user to monitor variations in continuum intensity or absorbed signal on a shot to shot basis. A second oscilloscope (HP54502A) is used to monitor both variations in laser pulse shape/intensity and in optical delay between laser pulses. The synchronised video signal from the PDA detector is digitised and stored in an EG & G Optical Multichannel Analyser (OMA - Model 1461) after each laser shot. If there is jitter in inter laser pulse delay or in relative intensity from shot to shot any 'rogue' scan can be discarded by the user before

accumulation takes place. The accumulated data are then down-loaded into a PC where the spectra can be stored and/or processed. The operational characteristics of the key individual components, mechanical, optical and electronic, which together make up the facility are described in the following sections.

2.2.2 GRAZING INCIDENCE SPECTROMETER

A description of the spectrometer has been given by Kiernan [1994] and a summary is included here simply for completeness. A schematic diagram of the spectrometer is shown in Figure 2.2. When working in the soft x-ray region (2 - 300Å) region of the spectrum it becomes necessary to operate reflection gratings at grazing incidence due to the poor reflectivity at normal incidence of single optical surfaces at such short wavelengths [Samson 1967]. The instrument used throughout this work is a Mc Pherson Model 247 M8, 2.2 metre grazing incidence VUV/XUV monochromator and conforms to a Rowland circle mounting for concave gratings. The complete optical system, stainless steel ways, grating chamber, entrance slit assembly and detector chamber are mounted on a granite base. This has the advantage of excellent stability and of providing excellent damping for unwanted vibration. The stainless steel curved way is fixed to the base plate and then machined to the Rowland circle radius.

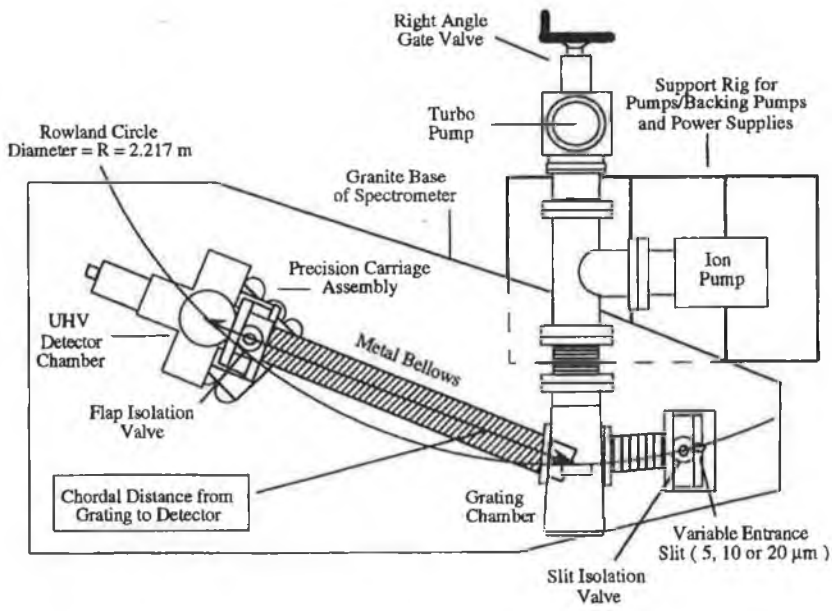

Figure 2.2 Top down view of grazing incidence spectrometer.

The exit slit assembly has been removed and a multichannel detector chamber installed in its place. This chamber houses an MCP detector, flap isolation valve,

pressure gauge ports and is attached by means of an adjustable mount to the carriage assembly. The carriage assembly utilises a recirculating ball bearing system, assuring smooth and accurate movement over the entire tracking range. Correct angular orientation of the scanning detector assembly to the beam is maintained through all wavelengths by a straight edge bar. The bar is built in an upside down "U" configuration and houses the wavelength drive screw. A manual scanning knob and mechanical counter assembly is attached to the end of the precision drive screw and straight edge assembly. Rotation of the knob moves the multichannel detector assembly along the Rowland circle. The mechanical counter reading is graduated in inches and indicates the chordal distance from the centre of the grating to the approximate centre of the detector array. The detector chamber can be moved across the Rowland circle, i.e., perpendicular to the point of tangent, via an adjustable translation stage. The adjustment is controlled by means of a micrometer and two locking screws. Loosening one screw and tightening the other screws moves the detector across the circle. An isolation valve is located between the detector chamber and the metal bellows. A support frame has been designed to carry cooling lines to the detector system which clamps onto the detector chamber. A stainless steel o-ring sealed bellows connects the detector scanning assembly and the main vacuum chamber which contains the grating.

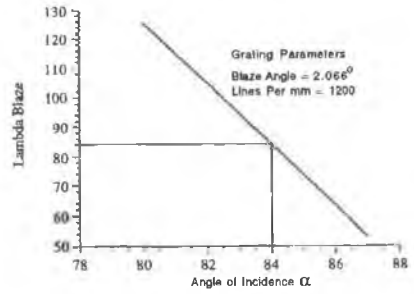

Figure 2.3 Plot of the variation of blaze wavelength (Å) with angle of incidence for the 1200 lines per mm grating used in this set of experiments [Kiernan 1994].

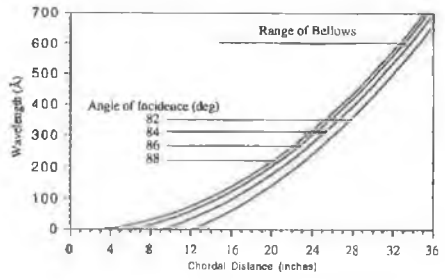

Figure 2.4 Plot of the wavelength ranges possible with a 1200 lines per mm grating at angles of grazing incidence from 82° to 88° [Kiernan 1994].

The main vacuum chamber (housing the grating) is made from stainless steel, sealed and connected by means of short bellows to a vacuum chamber containing the entrance slit assembly. Although in a fixed position while in operation, this latter chamber is easily moved along the curved wave for settings angles of incidence from 82° to 87°, with positive stops in 1/2° increments. All experimental data shown in this thesis were obtained with the entrance slit maintained on the Rowland circle at an angle of incidence of 84° to the grating normal. The grating used was concave with a gold coating, ruled at 1200 lines per mm with a blaze angle of 2° 4' (λ_{blaze} = 84.34 Å). Figure 2.3 shows the dependence of λ_{blaze} on the angle of incidence α. The grating assembly is kinematically mounted and can be removed/replaced or other grating assemblies placed in position without further alignment. The effective wavelength range of the instrument is determined by the grating being used, the length of bellows between the scanning detector chamber and the main grating vacuum chamber and the angle of incidence between the slit and the grating normal. Figure 2.4 summarises the wavelength ranges possible with the 1200 lines per mm grating at various angles of incidence. The wavelength range is inversely proportional to the number of ruled lines per mm. When substituting a grating not previously aligned, micrometers provide for fine adjustments on all axes. All motions, except focus, pivot on a ball bearing at the centre of the grating mount.

The ultimate operating pressure of the spectrometer is determined by the UHV requirements of the MCP detector. The MCP must be operated at pressures less than 2×10^{-6} mbar. The vacuum pumping system is connected to the main grating chamber by means of a vibration damped bellows terminated with 100mm (inner diameter) conflat type flanges. There are two types of vacuum pumps in use. A 240 l/s turbo molecular pump, backed by a two stage rotary, is employed to evacuate the system starting from atmospheric pressure (having vented and backfilled the instrument with dry nitrogen). When the pressure has reached approximately 1×10^{-5} mbar an ion pump is switched on. After the ion pump discharge has stabilised the turbo pumping system is isolated from the spectrometer via a right angled gate valve and switched off. The ion pump brings the ultimate pressure down in the detector chamber to less than 2×10^{-7} mbar, well below the minimum operating requirements. The ion pump is a getter type pump and as such has no need of a backing pump and, when operated in a UHV environment, it can safely be left running for years without deterioration in performance. The entire pumping system is supported on a specially designed rig, the height of which can be adjusted before connecting to the main vacuum chamber.

2.2.3 MULTICHANNEL PHOTOELECTRIC DETECTION SYSTEM.

For many years integrating detectors in the form of photographic plates were the basic tools of the spectroscopist. In more recent times, in order to gain the advantages of direct electronic detection, people have turned increasingly to the use of scanning instruments with single channel outputs and electronic detectors such as photomultiplier tubes or photodiodes. It was long recognised that array or multichannel detectors would be a powerful and welcome tool if they could be built with sufficient resolution, sensitivity and dynamic range. The operational characteristics of Microchannel Plates (MCP's) with photodiode or CCD array image readout meet all of the above mentioned requirements.

Originally developed as an amplification element for image intensification devices, MCP's have direct sensitivity to charged particles and energetic photons. Experience gained in the area of secondary emission in dynode electron multipliers in the 1960's and from earlier work on the technique of creating resistive surfaces in lead glass, together laid the foundation for the development of this device. The most important advance came through size reduction techniques achieved by glass fibre drawing techniques which form the basis of fibre optic device fabrication. A detailed description of the MCP manufacturing process is given by [Wiza 1979].

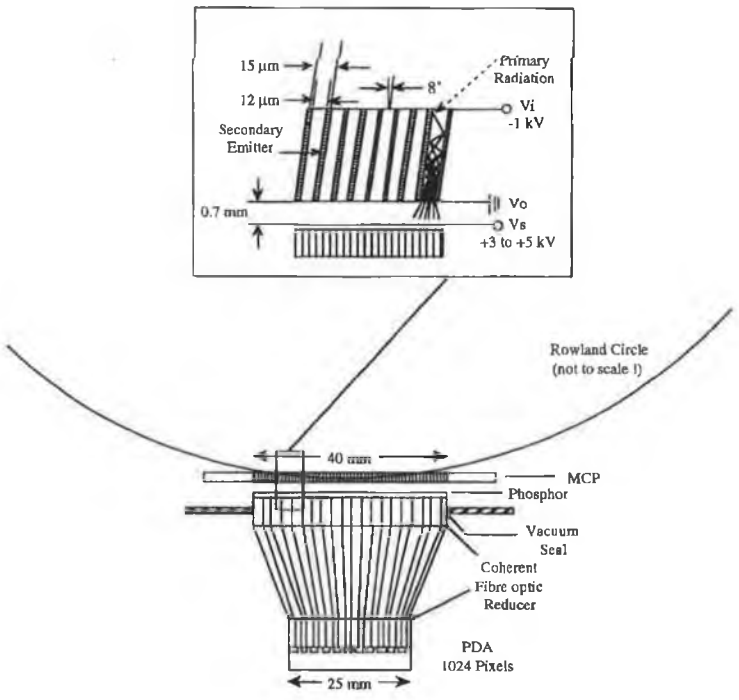

Figure 2.5 Diagram of MCP detector system installed in the grazing incidence spectrometer, the upper half of the figure is an expanded view of the signal intensification region [Schwob *et al* 1987].

An MCP can be considered as an array of miniature electron multipliers oriented parallel to one another. The device used here was supplied by Galileo Electro-Optics and has channel diameters of 12 μm on 15 μm centres. The active area of the matrix is 12.5 cm^2 and covers an approximately 40 mm length of the Rowland circle. The channel axes are biased at an angle of 8° to the surface normal. The quantum efficiency (QE) of a standard MCP is 10-20% for normal incidence photons with energies above 15 eV. The OAR (Open Area Ratio) of the MCP can be increased on the input side through chemical funnelling. By increasing the area of the open channels, the detection quantum efficiency will increase proportionally. Standard MCP's typically will have OAR's greater than 50%; however, chemical funnelling can produce OAR's of 70 % or greater [Callcott *et al* 1988]. This is particularly important in the grazing incidence regime where geometrical shadowing can prevent incident photons from penetrating far into the channels. In addition, surface photocathode coatings such as CsI (as used with present detector) improve QE and extend the sensitivity to shorter wavelengths. The channel matrix is manufactured from lead glass, treated in such a way as to render the walls semiconducting. Thus each channel can be considered to be a continuous dynode structure which acts as its own dynode resistor chain. Parallel electrical contact to each channel is provided by the deposition of a metallic coating on the front and rear surfaces of the MCP, which serve as input and output electrodes. The input electrode (Vi in Figure 2.5) is biased at up to -1kV with respect to the output electrode (Vo). This helps to prevent any back emitted electrons from leaving the array. The typical electron gain is about 1 x 10^4, depending on the MCP voltage. The amplified signal emerges as a bunch of electrons which are then accelerated across a vacuum gap (width = 0.7mm, E_{field} = 6 x 10^4 Vcm^{-1}) by a positive potential difference of about 4 kV (Vs) and proximity focused on a phosphor coated fibre optic bundle. The gain produced by an MCP is given by [Wiza 1979] :

$$G = \left(\frac{AV}{2\alpha V_0^{1/2}} \right)^{\frac{4V_0\alpha^2}{V}} \qquad (2.1)$$

where V is the total channel voltage, V_0 is the initial energy of the emitted secondary electron ~ 1 eV, α is the length to diameter ratio l/d (typically in the range 40-60), A is a proportionality constant ~ 0.4. Substituting typical values in Equation 2.1 yields G ~ 3 x 10^4.

The fibre optic bundle is mounted on a bakeable UHV flange and is tapered from 40 mm down to 25 mm, resulting in a demagnification factor of 1.6. Thus the visible

photon signal produced by the phosphor is readout by a self-scanned 1024 pixel (25 μm x 2.5 mm) PDA (Photo Diode Array - EG & G Model 1453).

2.2.4 PHOTO DIODE ARRAY (PDA) DETECTOR AND COMPUTER INTERFACE.

Linear silicon photodiode arrays function as photodiodes that are reverse biased and so they are, in effect, charged capacitors. When light strikes one of these photodiodes, electrons are released that neutralise holes to discharge the photodiode capacitance and change the voltage across the diode. During exposure to light, the voltage on each diode drops proportionally to the light (photons) falling on the diode during the exposure. During PDA scanning, shift registers and FET switches in the array package cause the photodiodes to be successively connected to the input of the detectors amplifier (Figure 2.6).

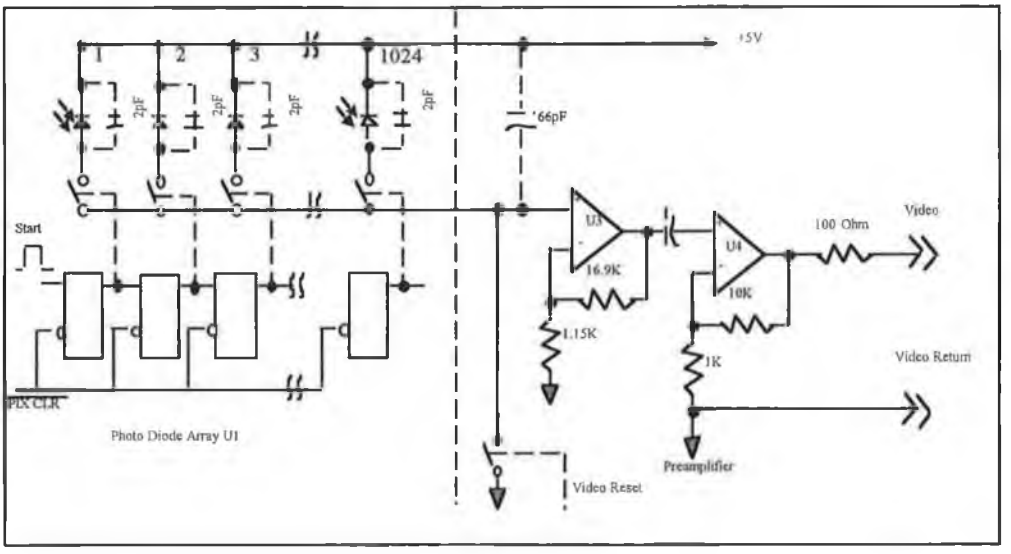

Figure 2.6 Simplified diagram of the PDA detector (Model 1453).

Each successive level defines the integrated light on the addressed pixel. The analog video signal from the PDA is controlled and read by an EG&G Princeton Applied Research 1461 Detector interface which forms the heart of the OMA system and is a desktop size device designed to acquire data from a light detector. The detector sends an analog signal through a shielded cable to a detector controller card (EG & G Model 1462) mounted in a slot of the interface. The controller converts this signal to digital information that can be used by the interface. In addition, the controller governs all aspects of the detector operation including, scanning, triggering and temperature.

The digitised data is stored in the interface's on board memory (32K RAM) and can be accessed by an external host computer. The external computer not only accepts data, but also controls the entire data acquisition process. This control is maintained by means of a set of special commands that the microprocessor based interface interprets and executes. Parallel communication between interface and PC is achieved through an IEEE-488 GPIB (General Purpose Interface Bus) and a GPIB connector. A comprehensive menu driven software package, to control the data acquisition process, was developed in house by the author. This software allows the user to adjust the data acquisition parameters, such as total number of scans, inter scan time-delay and detector integration time in remote mode. Flexibility of data storage is also provided; e.g., the user can chose between running in continuous mode and accumulating all scans in memory, or in single shot mode where after each scan, which synchronises the laser pulses, a choice is made whether or not to add the resulting data to memory. This decision to run in continuous or single shot mode is usually determined by the stability of the inter-laser time delay which is monitored by a fast optical sensor (BPX65 photodiode operated at a 9 V reverse bias) connected to a Hewlett Packard 54502A digitising scope with a single shot sampling frequency of up to 2.5 ns/point. Digital data, stored in the interface unit, are then down loaded through the GPIB to the PC where it is stored in standard ASCII file format for further data processing.

2.3 SOFTWARE AND INTERFACING

2.3.1 BACKGROUND

The purpose of this section is to discuss the various elements involved in developing software for the control of and data acquisition from the associated PDA detector and associated electronics. Following an outline of the main operational requirements of the software a description of the various software (GPIB control files) and hardware (computer, GPIB interface card, Optical Multichannel Analyser (OMA) detector interface) will be given. Explanations and diagrams describing the various timing considerations in the experiment will be presented. Finally a brief discussion of the actual software developed and how it should be used will be given.

A substantive aim of this project was to develop software for the control and data acquisition of the EG & G detector interface.

The specific requirements for the software development can be stated as follows :

- The software had to be intuitive and user friendly so that a first time user could use the system with relative ease and little tutoring.

- Along with the multichannel spectral experiments carried out, a time synchronised multi-laser system is used. This synchronisation was carried out using in house designed delay generators with an increment of 10 ns and a jitter of ± 5 ns [Lynam *et al* 1992]. The OMA device had to provide a master trigger pulse which was passed to the delay generators, which in turn trigger the lasers, in a well defined time sequence. The software had to ensure that this pulse occurred at the correct time in the sequence of events during an experiment.

- The last basic requirement of the software was that it control and acquire spectral image data from the detector in a simple and efficient manner with the use of a PC computer and a detector interface. Spectral images would then be transferred to the PC computer via the OMA. The software in the PC would then be required to plot on screen and later to a printer the spectral image. Facilities such as adding multiple shots, and averaging files were included in the software.

These are the requirements which were originally stated. Further improvements and facilities were added to the software during testing of the complete system. These are discussed later during a more detailed account of the software capabilities.

2.3.2 GENERAL HARDWARE / SOFTWARE DESCRIPTION

The hardware used in the software development and interfacing included the following :

- Tandon 286 PC-AT computer
- General Purpose Interface Bus (GPIB) card (National Instruments 488 equivalent)
- EG&G PARC Model 1461 Detector Interface including a Model 1462 Detector controller
- EG&G PARC Model 1453 Silicon Photodiode Detector
- Hewlett-Packard (HP) 54501A 100 MHz Digitising Oscilloscope

The software used in the development and interfacing included the following :

- Turbo C++ Version 1.0
- GPIB-PC software files and additional programs and files including installation, test and example programs.
- SPECTRA CALC™ plotting and data analysis software.

The figure below shows the hardware configuration used while the software was being developed and tested.

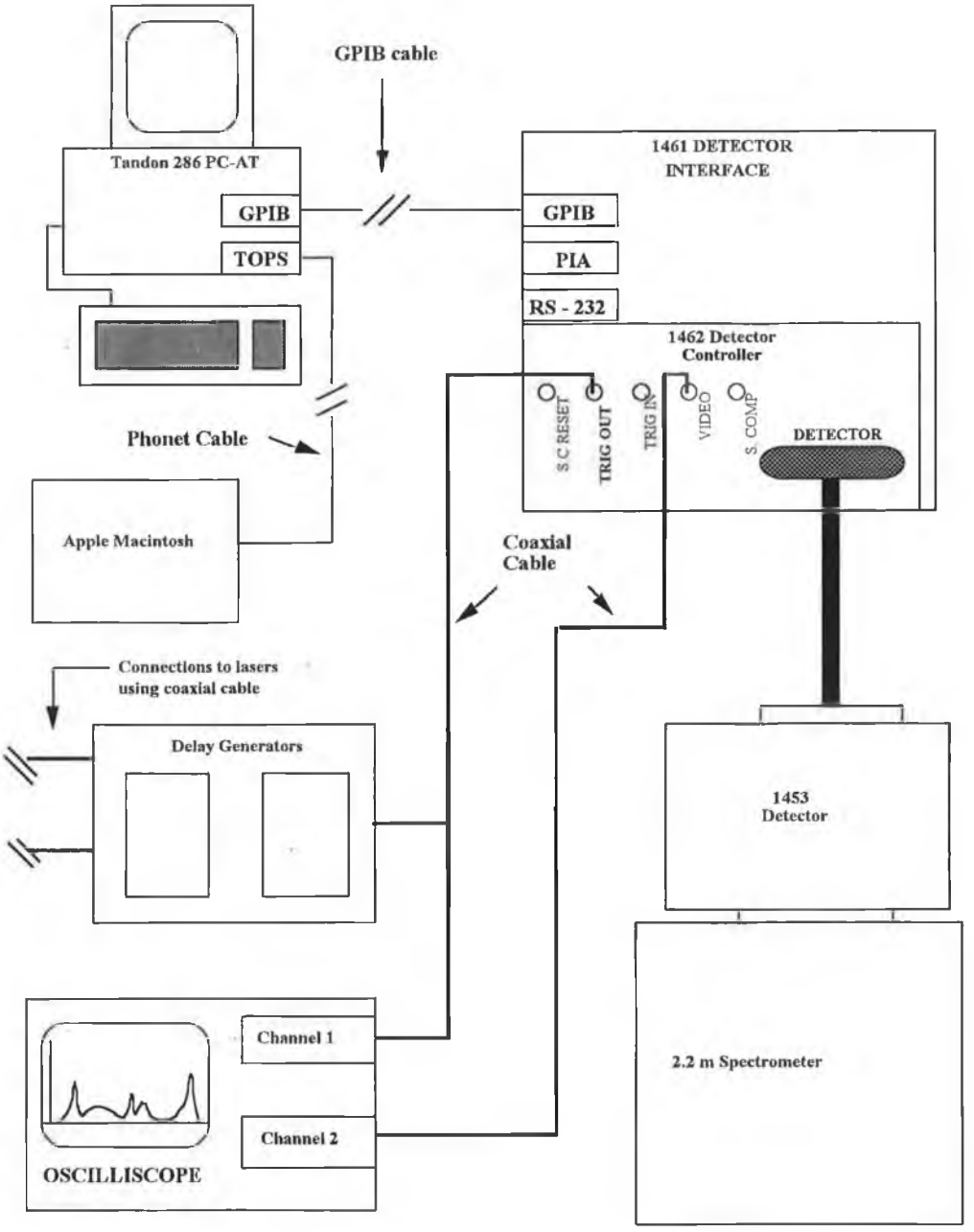

Figure 2.7 Schematic showing a typical data acquisition set-up using a Model 1461 Detector Interface.

2.3.2.1 TANDON PC

This is an IBM compatible 286 machine with 1 MB of RAM, 40 MB hardisk, Advanced MicroDevices math co-processor, VGA monitor and two interface card slots. This computer was used to program the OMA and acquire data from it. It was also used as a temporary storage device for the experimental data acquired. Long-term storage for the data was on 3.5" floppy disks and also on an Apple Macintosh IIci computer. The data was transferred from the PC to the Macintosh via a TOPS network. The TOPS communications card was installed in one of the PC's interface slots, while the GPIB card occupied the other. The data was plotted and analysed on both the Macintosh and PC.

2.3.2.2 GENERAL PURPOSE INTERFACE BUS (GPIB) AND ITS ASSOCIATED SOFTWARE

The GPIB is a link, or bus, or interface system, through which interconnected electronic devices communicate. This link is used to connect and control programmable instruments. Typical data transfer rates for the link range from 250 KB to 1 MB per second. These high data transfer rates have led to other applications such as intercomputer communication and peripheral control. This communication link is now an industry standard designated as IEEE-488. The IEEE-488 bus is the most widely used method of connecting a number of instruments to the I/O port of a computer. Ability to make use of the bus is a built-in feature on many EG&G PARC instruments including the Model 1461 Detector Interface.

Communication between devices on the bus is done by passing one of two types of message through the system. The first are known as device-dependent messages and contain information such as programming instructions, measurement data, machine status, and data files. The second type, interface messages, are command type messages for, say, addressing and unaddressing devices. Devices on the bus can be listeners, talkers and/or controllers. In this project, the user software and computer act as talker and listener, the GPIB interface is the controller addressing and unaddressing talkers and listeners before they send and receive data, while the 1461 Detector Interface is both a listener (receives instructions from computer) and talker (sends spectral data from its memories to the PC via the GPIB). A talker basically sends messages to one or more listeners with the controller managing the flow of information by sending commands to all the devices.

Using a plug-in interface card and controlling software (discussed below), an IBM PC or compatible can be converted to a controller in charge of a wide range of test

equipment. The GPIB interface card used in this project is a PCII-IBM PC interface card supplied by Integrated Measurements Systems (UK) Ltd.. This is a half-size card which occupies one of the card slots in the PC. Interconection between the interface and the 1461 interface is made using a standard IEEE-488 cable.

There are a number of support and utility files which come with the GPIB interface system which must be installed in order for the interface to operate properly. The more important files are briefly discussed below :

- **GPIB.COM -** It is a device handler file that is loaded at system start-up by the DOS operating system. This file remains resident in memory while the computer is switched on. It permits all GPIB hardware (talkers, listeners and controllers) to communicate with one another. It allows you to use different programming languages, operating systems and computer architecture's.

- **IBIC** - With the IEEE-488 Bus Interactive Control (IBIC) utility you can control and communicate with instruments from the keyboard. The IBIC utility is a simple way to learn the GPIB handler functions and the device specific commands of the instrument or to troubleshoot the system.

- **IBCONF** - A utility program that configures the GPIB interface handler for GPIB addresses, time-out settings, termination methods, and device-specific characteristics. The settings entered via this program are then stored in the file GPIB.COM for use by the interface system. See appendices for the settings used in this project.

- **APPLICATIONS MONITOR -** A software utility that performs automatic error detection and identification. It is a memory resident program which is useful in debugging sequences of GPIB calls from within an application program.

Figure 2.8 displays the important files involved in using a GPIB interface to control a device. Also shown are the different operating systems and programming languages which make use of the handler file GPIB.COM.

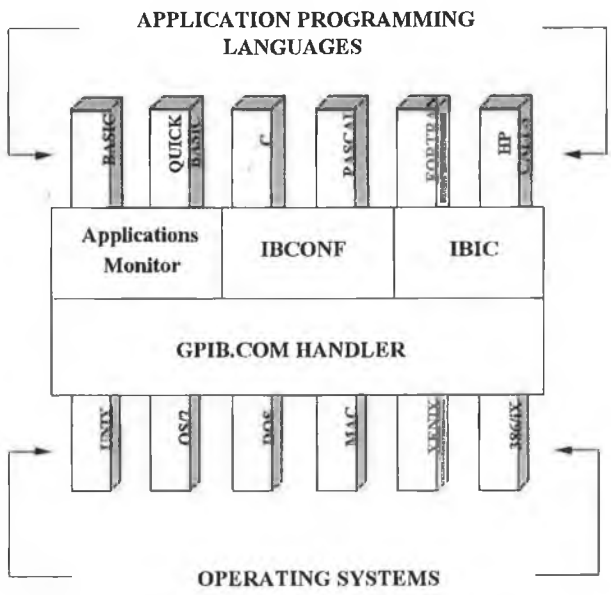

Figure 2.8 Diagram showing the various programming languages and operating systems which can use the various utility programs provided with the GPIB software.

The diagram shows that the GPIB is a very flexible method of communicating with many devices no matter what the software and hardware used. For this project the application programming language used was TURBO C, while the operating system was DOS.

Also the files which the GPIB uses and the application software must be installed having regard to a particular directory structure. Details concerning the file installation are given in the appendices.

2.3.2.3 MODEL 1461 DETECTOR INTERFACE INCLUDING THE MODEL 1462 DETECTOR CONTROLLER

The 1453 PDA array detector described in Chapter 2 is controlled using an electro-optical signal processing/readout system known as a Optical Multichannel Analyser (OMA). This system, developed by EG&G PARC laboratories, provides an extremely fast and powerful computer controlled method for light analysis and spectroscopy. The specific type of OMA system described here is a Model 1461 Detector Interface which houses a range of cards in vacant slots and allows connection to one or more PDA detectors (Figure 2.9).

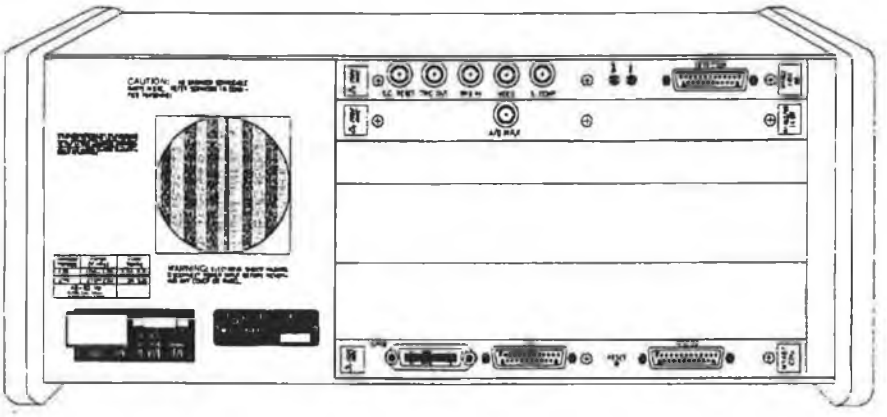

Figure 2.9 Model 1461 Interface [EG & G 1461 Interface Manual].

It is a desktop size instrument designed to acquire data from light detectors. The data are stored in the 1461's memory and can be read by an external "host" computer. Utilising either user or commercially developed software the external computer not only accepts data from the 1461, but it is also capable of controlling the entire data acquisition process. This is achieved using a Model 1462 Detector Controller. This is a card, conforming to the virtual memory extended (VME) bus standard, which is installed in a free slot of the 1461 interface. The 1462 controls the spectral data acquisition by utilising both on and off-board timing circuitry, various amplifiers, latches and a 12-bit Analog to Digital Converter (ADC). The main functions of the controller are to convert the analog signals generated on the detector photodiodes into digital data (which are then stored in the 1461 interface RAM), provide the timing required for the controlled scanning of the detector and also receive and transmit trigger pulses which can be used to control the experiment. The control is carried out using a set of commands specific to the Model 1461, which are sent to it via the external computer. The interface then interprets the commands and configures the detector controller to perform the control and data acquisition in the manner specified by the parameters sent to it by the user. The interface is only used to acquire data from and control the detector; actual analysis and interpretation of the data is carried out by the "host" computer and its software. The Model 1461 basically functions as an interface between the computer and the detector and serves as the power supply for the detector and the detector controller.

2.3.2.4 MODEL 1461 DETECTOR INTERFACE CONFIGURATION

The following information is just a brief summary of the interface configuration used in the experiments relevant to this project. The 1461 interface unit contains mainly solid state electronics, incorporating VME bus circuitry along with a MOTOROLA™ 68000 microprocessor. The timing between the various circuits of the interface is

controlled by a 16 MHz crystal oscillator. The interface has a capacity of 8 VME slots. The slots contain the 1461 CPU board and the 1462 detector controller; this allows for 128 kbytes of ROM and 32 kbytes of RAM. This means up to 6 separate 1024 point curves or sets of readings can be stored in separate memory locations. The memory is expandable using extra memory boards installed in the vacant slots. Three interfaces available to the user; serial RS232, a non standard parallel and IEEE488 GPIB. There are a number of switch settings which must set in order for this interface to be addressable. The GPIB dip switches are the ones on the left-hand side as you look at the CPU board through the rear panel of the 1461 interface The switch settings used are shown in diagrams contained in the appendices.

2.3.2.5 MODEL 1462 DETECTOR CONTROLLER CONFIGURATION

This is an extra VME card which is installed in the 1461 detector interface along with the 1461 CPU board. The 1462 controller used in these experiments was installed in slot 8 of the 1461 interface. The connections between the controller and the rest of the experimental set-up are as follows :

- Detector input/output. This is a 25-pin D connector which provides interfacing to the PDA detector (Model 1453). The connector holds the timing signals, analog voltages and the DC power levels that allow detector operation.

- Video Output. This connector transmits the output of the 1462's sample-and-hold circuitry. It is used for the real-time (instantaneous) monitoring of the signal on the detector pixels (picture element). This signal is transmitted as a video signal via a 1 MΩ connection to a video monitoring device such as an oscilloscope. It is a useful feature as it allows you to see what the spectral data looks like without having to first download and then plot the data.

- Trigger Out (TOUT). The output signal of this connector is pixel (28 μs) wide with rising edge occurring 3 pixels (pixel no. 1028) after the last analog to digital conversion of the detector scan. The availability of this pulse is software controlled. The pulse is used to trigger the oscilloscope video input via a 50 MΩ connection and provide a master pulse to two delay generators used to synchronise the different lasers used in the experiments.

The other connections on the detector controller are explained in the controller user manual (see references).

2.3.2.6 DETECTOR SCANNING/EXPOSURE TIME CONSIDERATIONS

There are a number of scanning methods available to the user of the detector interface/controller combination. The 1462 controller only allows the use of a mode known as the normal scanning mode. During normal scanning, the amount of charge on each detector element (pixel) is read by the detector, digitised by the detector controller, and stored in the 1461 interface.

The basic unit of time in the 1461 system is called the **exposure time**. It is the total time between successive reads of a detector element i.e. a pixel. It is composed of three basic elements; SCAN TIME, OVERHEAD TIME, VARIABLE INTEGRATION TIME (VIT). The SCAN TIME is the time required to read/reset all the detector pixels (1024 pixels for the Model 1453 Detector) as opposed to the pixel time which is the time required to read/reset one pixel (28 μs). The OVERHEAD TIME is immediately after the scan time. It is used by the interface and controller to make decisions about the next detector scan. For the experimental configuration used in this project this time is the same for every scan. The VIT follows the OVERHEAD TIME and during this period the detector is not being scanned and the system is basically at rest. There is a trade-off between increased VIT and dark current build up / saturation. VIT can range from values of 0 seconds to larger values which have no practical use. By having a large exposure time you integrate a greater amount of flux falling on the detector array, hence you increase the signal to noise ratio. Longer exposure times also mean greater build up of dark current, which can over a long period of time saturate the detector. This must be a consideration when setting the exposure time. For the experiments carried out in this project, the exposure time is a multiple of 30 ms. Usually it is set to the minimum value of 30 ms, as the laser plasma pulse has duration of less than 1 μs or so and hence exposure times greater than the minimum do not improve SNR.. The following details about exposure times are of relevance to the 1462 controller used in conjunction with the Model 1453 detector:

No. of Array Elements	Pixel Time	Base Exposure Time
1024	28 μs	30 ms

The base exposure time consists of the detector scan time plus the overhead time explained previously. The exposure time for the 1462 controller is composed of the

base exposure time (30 ms) plus multiples of this time (delays scans) which make up the total exposure time. During these delay scans, which are part of the VIT, the array is not read/reset and as a result the flux falling on the pixels is constantly being integrated. These delay scans are added to the base exposure time if the exposure time required is greater than 30 ms e.g., exposure time 120 ms means there is a period of 4 x 30 ms before the detector pixels are read/reset. The diagrams below illustrate the various timing and scanning procedures used with the 1461 detector interface/1462 controller/1453 detector.

A. **Schematic showing how base exposure time for detector system is defined**

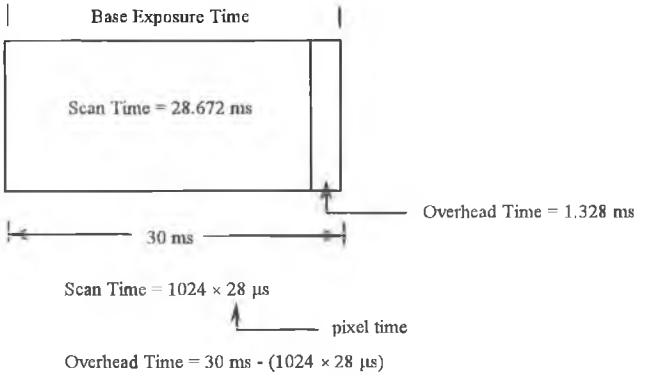

B. **Schematic showing trigger pulse available at TRIG OUT connector of detector controller**

NOTES : This TRIG OUT pulse is software controlled. When data acquisition mode 4 is used this pulse appears during the overhead time and before a data acquisition scan takes place. This is shown below.

C. **Schematic showing where trigger pulse occurs during exposure time when data acquisition mode 4 is used**

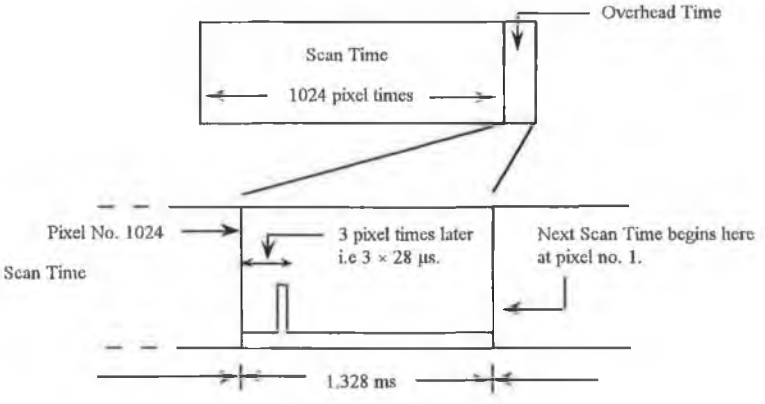

NOTE : The rising edge of the trigger pulse occurs 3 pixels after the last A-to-D conversion of the detector scan ie at pixel no. 1028. i.e at (1028 × 28 µs) of the 30 ms base exposure time. This pulse is sent to the delay generators which then fire the lasers.

Fig 2.10 Diagram showing the breakdown of the base exposure time of the 1462 Detector Controller and where the TRIG OUT pulse occurs during a scan.

Figure 2.10 shows the situation when the base exposure time is chosen as the exposure time used during experiments. NOTE : these drawings are not to scale. The diagrams below show the situation when the exposure time is chosen so that it is greater than 30 ms. This diagram shows how delay scans are used to increase the exposure time. This diagram does not include a TRIG OUT pulse before each scan.

Model 1462 Exposure Time, Normal Scanning and Synchronisation

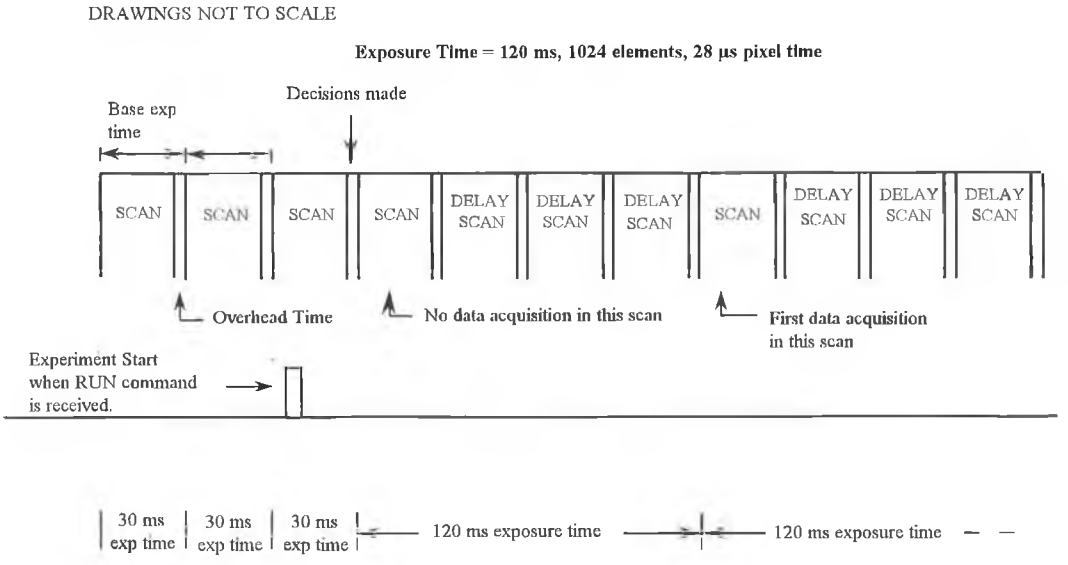

Fig 2.11 Model 1462 Exposure Time

When the detector interface receives the RUN command from the control software it implements the sequence of events shown in Figure 2.12. The scan during which the RUN command is received runs to completion. During the following overhead time decisions are made about what to do next based on the selected data acquisition mode

The 1461 interface has pre-programmed sets of commands which perform specific functions which affect the way it stores and processes the detector data and also the way it controls the detector using the 1462 detector controller. The various commands are detailed and explained in chapters 10 - 17 of the 1461 interface instruction manual [see reference list EG & G manuals]. What follows is an explanation of the commands which are relevant for this project. The commands which control and acquire the data are grouped together in specific programs stored in the ROM chips of the 1461. These are known as the data acquisition modes of the device. The data acquisition mode used almost exclusively in the experiments described here is mode 4.

Before a data acquisition mode can be used, the detector interface must have the relevant parameters sent to it via the host computer. A listing of this mode and an explanation of how it operates follows:

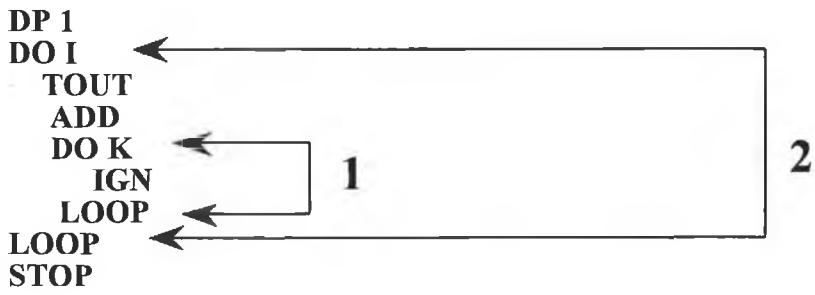

1 **DELAY LOOP CONTROLLED BY THE NUMBER OF IGNORE SCANS**

2 **OUTER LOOP PERFORMS THE ACQUISTION PROCESS A SPECIFIED NUMBER OF TIMES**

Figure 2.12 Diagram showing the listing for the data acquisition mode used by the detector interface during the experiments

The command 'DP1' selects double precision for data storage. There is one set of 'I' scans. These are the actual data acquisition scans where the lasers fire due to the TOUT trigger pulse sent from the detector controller before each scan and the resulting data, which is imaged onto the array, is read from the detector. After each scan the data is added into the same memory location previously specified by the MEM command. There is a provision for ignoring K scans which allows you to program a delay between a sequence of data scans and so allow you to control the frequency of laser shots.

There are a total of 17 pre-programmed data acquisition modes available. Mode 4 is chosen because it is suitable for the experiments carried out for the following reasons :

- It provides a trigger output pulse (TOUT) which occurs before the start of each experiment. This pulse synchronises events in the experiment from the point of view of firing two lasers at pre-set times using delay generators.

- The data for a number of laser shots, which is read from the detector, can be added/accumulated in the one memory location so that there is a $\sqrt{n}$ improvement in the signal-to noise ratio (SNR) over a single scan.

- The provision of ignore scans in the loop means that the duty cycle of the laser systems used can accurately controlled.

2.3.2.7 PC OMA SOFTWARE PACKAGE

The menu driven software package developed as part of this thesis controls the entire operation of the 2.2 m spectrometer described above, from triggering the lasers to fire, to acquiring the resultant spectra from the PDA detector via the OMA control box. Also post processing of the data e.g. subtracting spectra , getting the natural log, plotting etc. was accomplished using the software. The diagram below shows the main menu and all the sub-functions that can be performed. The software is user friendly and is activated by typing OMAPROG at the DOS prompt.

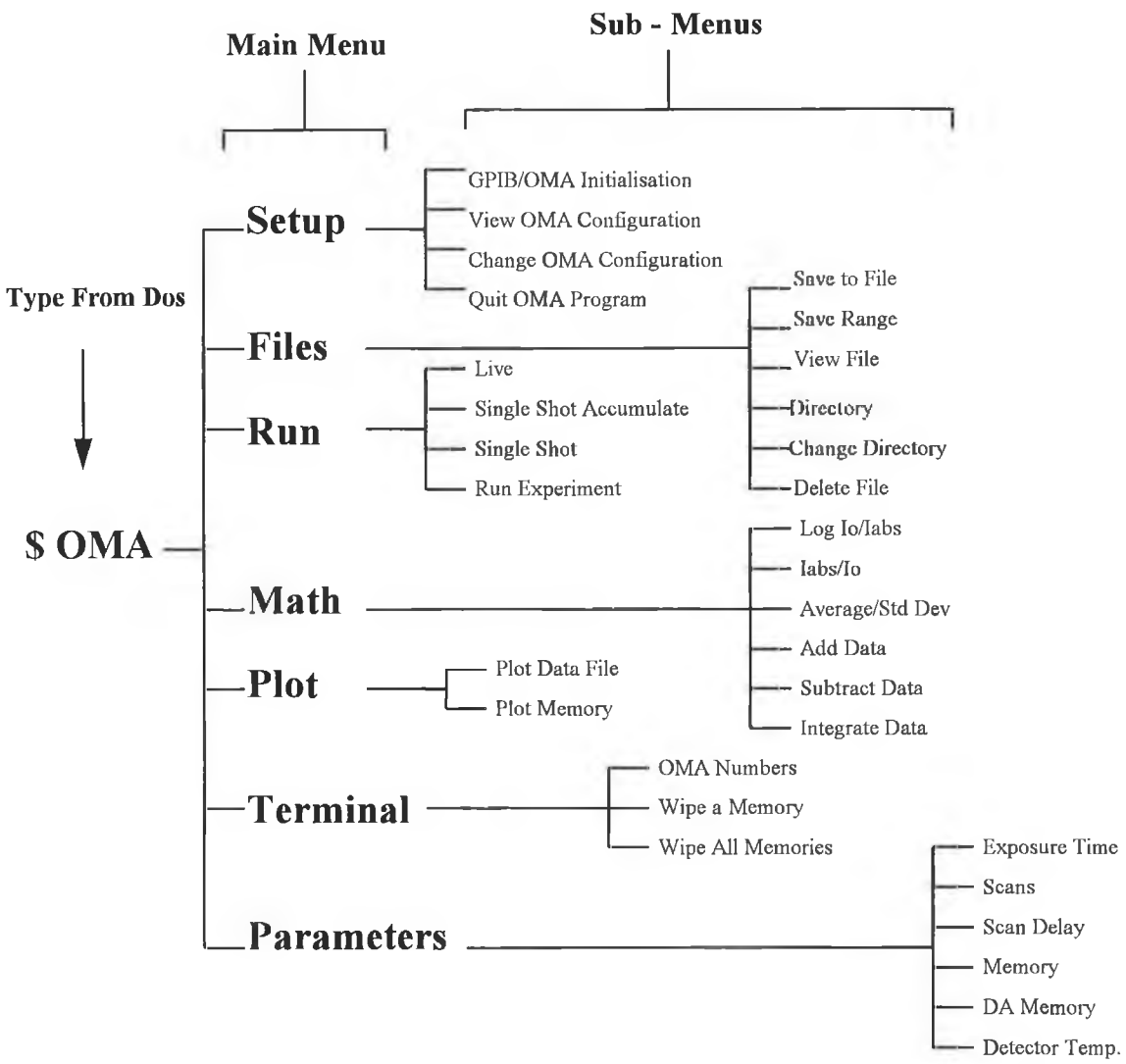

Figure 2.13 OMA Software Flow chart showing Main Menu Options and sub-functions.

2.4 SPECTROMETER PERFORMANCE

2.4.1 RESOLUTION

The resolving power and reciprocal dispersion (see Figure 2.14) of a spectrometer are closely related quantities. While the dispersion determines the separation of two wavelengths, the resolving power determines whether this separation can be distinguished. Each monochromatic beam itself forms a diffraction pattern, the principal maxima of which are represented by the order number m. Between such maxima, secondary maxima exist whose intensities decrease as the number of ruled lines, N, exposed to the incident radiation increases. In practice these secondary maxima are very much weaker than the principal maxima. If we use Rayleigh's criterion, two lines of equal intensity will just be resolved when the maximum of one falls on the minimum of the other. The resolving power is defined as $\lambda/\Delta\lambda = mN$ (for a plane grating), where $\Delta\lambda$ is the minimum wavelength separation which can be resolved. Mack *et al* [1932] have shown that a slit width W gives rise to an image width on the focal curve, of a concave grating in a Rowland mount, corresponding to a wavelength interval $\Delta\lambda = Wd/R$, where d is the inter grove spacing and R is the radius of curvature of the grating. Slit widths of 10 and 20 μm, combined with a 1200 lines/mm grating of radius of curvature = 2.2 m, were used throughout the photoabsorption/emission experiments described in this thesis which gives rise to an instrumental line width of between 0.038 and 0.076 Å.

In order to critically assess the performance of the instrument, in terms of its resolution, it was decided to examine the wavelength separation of some well known closely spaced lines in the emission spectrum of a laser produced aluminium plasma. Using a 1200 lines/mm grating the wavelength range accessible with the spectrometer is approximately 80 to 500 Å, as determined by the angle of incidence on the grating and the available length of bellows connecting the grating chamber to movable detector.

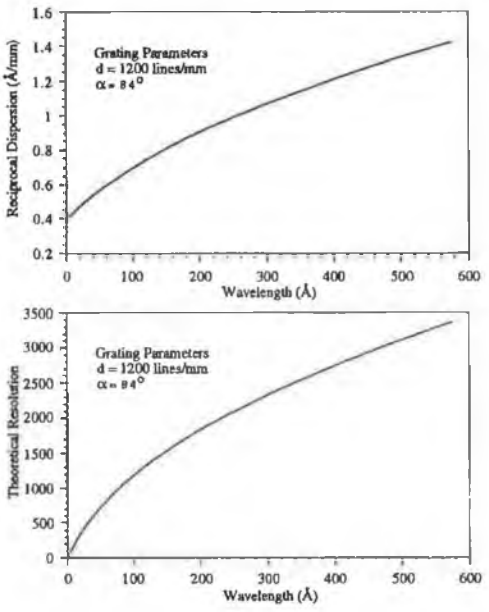

Figure 2.14 Plots of reciprocal dispersion (Å/mm) and theoretical resolution ($\Delta \lambda / \lambda$) for a 1200 lines/mm grating as a function of wavelength

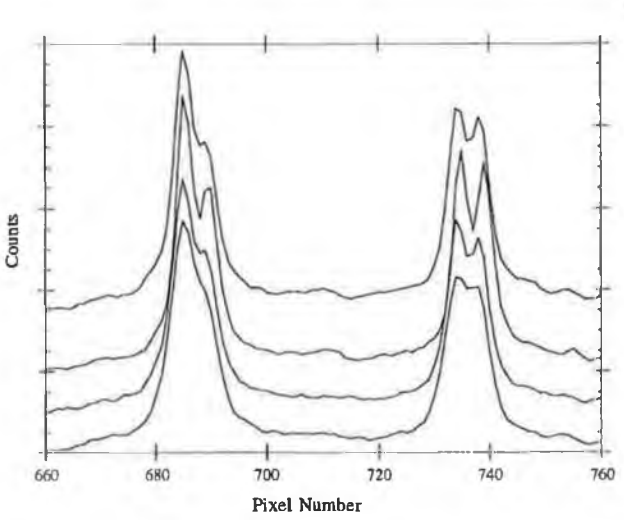

Figure 2.15 Spectrum of Al VII emission lines (10 μm entrance slit) showing dependence of resolving power on the position of the detector on the Rowland Circle [Kiernan 1994]

At about midway through this range, at approximately 260 Å, there are a number of Al VII doublets which were chosen for resolution testing. The aluminium plasma was generated by focusing the output of the Q-switched YAG laser on spectroscopically pure aluminium. The reciprocal dispersion at 260 Å is 0.99 Å/mm for this grating/Rowland circle configuration. As mentioned in section 2.2.3, the detector presents 40 mm of coverage at the circle, through the demagnification introduced by the fiber optic taper each pixel (25 μm diameter) of the PDA,

corresponds to a spatial sampling width of 40 μm on the Rowland circle. Hence, at 260 Å each pixel corresponds to a wavelength interval of ~ 0.04 Å. The Al VII doublet feature has a wavelength separation of 0.171 Å (~ 4 pixel widths) and should therefore be a good test of the resolving power of the multichannel spectrometer system.

Early results on emission spectra (the lower most curve in Figure 2.15) in the region of this doublet feature (at pixel no. 734) were disappointing. A single broad peak with very little evidence of fine structure was observed. Two potential sources of resolution degradation were examined; firstly the voltage between the exit face of the MCP and the phosphor, V_{ph}, was increased to help reduce the spread of the emergent electron bunches. The divergence of the electron beam is caused by space-charge repulsion and by the random non axial velocity components of the electrons as they exit the channels and reduces as $\sqrt{V_{ph}}$ and hence only a minor improvement was expected and subsequently observed. Secondly, and more beneficially, the detector was traversed across the Rowland circle assuming that some degree of misalignment and defocusing had occurred. The effect is well illustrated in Figure 2.15 above where the improvement in resolution is obvious as the detector is moved in 0.01 inch increments through the point of best focus.

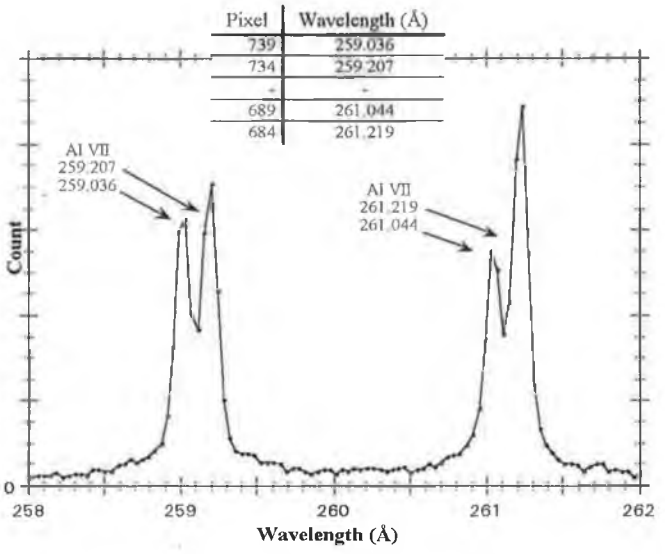

Figure 2.16 Spectrum at optimised focal position on the Rowland circle where the Al VII doublet at 260 Å is clearly resolved.

The spectrum shown in Figure 2.16 was recorded at the optimised detector position and represents the accumulation of three laser shots, at an MCP voltage of -0.930 kV and phosphor-MCP voltage of 4.5 kV. On examination of the doublet feature

components, 259.207 and 259.036 one observes that there are 5 pixels separating the features in comparison to an expected 4 pixels. One cause for a slight loss in resolution is most probably linked to the size of the gap between the MCP and the phosphor. The dependence of the diameter (ϕ) of the electron-bunch spot on the phosphor to the MCP-phosphor voltage Vph and gap distance (s) is given to a good approximation by, $\phi = s[V_{ph}]^{-1/2}$ [Cromer *et al* 1985]. A simple calculation with this formula shows that for a gap s = 0.7mm and V_{ph} = 4200 V, $\phi \approx 11$ μm. This is substantially less than the observed instrument limits of ~ 4 pixel widths or 100 μm. However, taking the Nyquist sampling spatial frequency limit of $f_{samp} > 1/2\Delta x$, Δx = pixel width, at least 3 pixel widths are required to avoid aliassing and hence a 4 pixel limit is quite acceptable.

2.4.2 DETECTOR NOISE PERFORMANCE

A basic understanding of the origin, behaviour and magnitude of noise sources in a spectrometer detection system helps considerably in optimising its signal to noise ratio (SNR). The PDA detector used here is a parallel imaging detector and the advantage of using such a detector is largely determined by its inherent sensitivity and resolution and by its noise behaviour relative to that of the system as a whole.

Several sources of noise are present when signals stored by a PDA are read out. These have been discussed in detail by a number of authors [Simpson 1979, Talmi *et al* 1980, EG & G Model 1453 Service Manual] and are summarised here.

Before discussing detector noise we should make brief mention of the effect of dark current i_d. As the temperature of a PDA is reduced, the number of thermally generated electron/hole pairs decreases with a resultant decrease in i_d. Dark current i_d effectively limits exposure time and hence PDA detectors are normally cooled during operation. For data collected in this thesis, an operating temperature of 5°C was achieved by means of a Peltier-effect thermoelectric cooler coupled to the 1453 PDA camera head. Additional cooling was provided on this detector by circulating water through the cooling block at the rear of the detector housing.

There are a number of sources of noise present when the signals stored by the PDA are read out. The two main components of this noise 1) Random noise and 2) Fixed pattern noise. The following sections focus in on the first of these noise sources as fixed pattern noise can be removed by subtracting a dark scan from the scan containing the optical information of interest (NOTE : this subtraction assumes the array temperature and readout rate are kept constant and hence this fixed pattern is constant from scan to scan). Fixed pattern noise is caused by stray capacitive

coupling of the transients arising from the clock driving signals to the video lines by external stray capacitances and by diode-to-diode dark charge variations.

2.4.2.1 NOISE SOURCES

Random noise in PDA's is generally due to the following sources :

1. Photon (Shot) noise on the incident light.
2. Shot noise on the dark current.
3. Noise due to the preamplifier
4. The reset noise of the pixels of the array ('KTC' noise).

The first noise component is due to the statistical nature of the arrival of the photons at each pixel. This is a natural source of noise which obey Poisson statistics.

All silicon image detectors are subject to thermally generated dark current and its associated statistical fluctuations i.e. dark current shot noise. The dark current shot noise in electrons is given by

$$n_d = \sqrt{\frac{i_d\, t_i}{q_e}} \qquad (2.2)$$

where i_d is the dark current, t_i the integration (exposure time) between readouts and q_e the electronic charge. If you take $i_d = 1$ pA (dark current at 5°C), $t_i = 30$ ms and $q_e = 1.6 \times 10^{-19}$ then $n_d = 433$ which is less than 1 e^- / pixel. For $t_i \sim 1$ sec then $n_d = 2$ to 3 e^- / pixel.

The noise due to the preamplifier is

$$n_a = \frac{C}{q_e}\sqrt{4kTB\,\frac{k_o}{g_m}} \qquad (2.3)$$

where k is Boltzmann's constant, B is the bandwidth, T is the absolute temperature, and k_o/g_m is the channel resistance of the input FET and C is the capacitance at the amplifier input which is composed of

$$C = C_v + C_{amp} + C_s$$

where C_v is the video line capacitance of the photodiode array, C_{amp} is the preamplifier input capacitance, and C_s is any stray capacitance due to the amplifier

input mode. For B = 10 MHz, kT = 1/40 eV, C = 10 pF then $n_d \approx 250$ over 1024 pixels.
The pixel reset (or 'KTC') noise is given by

$$n_r = \frac{1}{q_e}\sqrt{kTC_p} \tag{2.4}$$

where C_p is the pixel (diode) capacitance. The pixel noise is larger than this however due to the multiple readout switching of the PDA and the lowest total rest noise available to an off-chip amplifier is

$$n_r = \frac{1}{q_e}\sqrt{kT(2C_p + 2C_{vc})} \tag{2.5}$$

where C_p is the pixel diode capacitance and C_{vc} is the video line to clock capacitance. Applying equation 2.5 to the 1024 pixel S series array used in this thesis, with C_p = 2 pF and C_{vc} = 1.2 pF yields at 20°C, $n_r \approx 1000$ and at 5°C, $n_r \approx 950$. This noise contribution tends to be the dominant component on a detected signal.

2.4.2.2 EXPERIMENTAL NOISE DATA.

In order to obtain data regarding noise levels and how they affected the system performance it was necessary to ensure that the PDA was in a light tight environment. This was achieved by closing the entrance slit to the spectrometer. The PDA temperature was set to 5°C to simulate typical experimental conditions and a number of different measurements were made. These are summarised and discussed below.

A series of measurements were undertaken in order to investigate the relationship between dark current and dark noise and how these vary with exposure time. This was done by performing single dark scans of the array for various exposure times (30,60,120,240,480,960,1920 ms). A plot of the pixel value for each exposure time vs. pixel number is presented in Figure 2.17 (a), while the average dark count vs. exposure times is shown in Figure 2.17 (b)

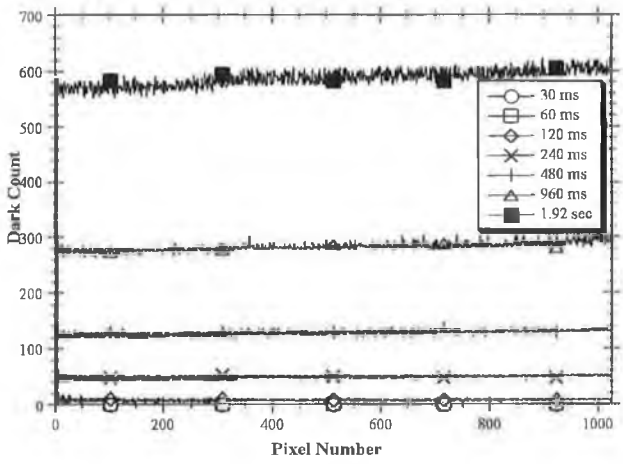

2.17 (a)

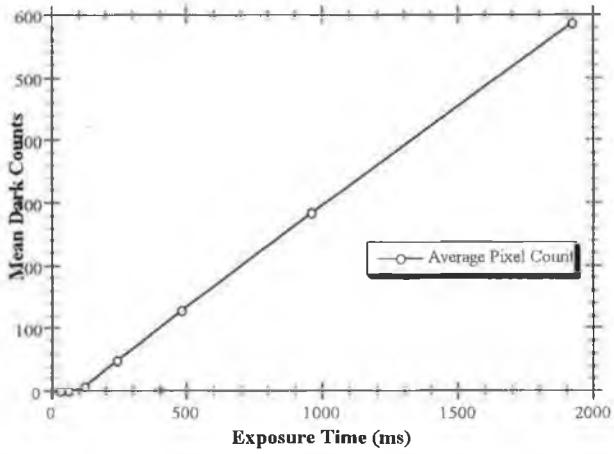

2.17 (b)

Figure 2.17 Relationship between dark count and exposure time on a 1024 element EG & G silicon PDA (Model 1453). (a) Pixel counts across array for various exposure times. (b) Relationship between dark count and exposure time.

Figure 2.17 (a) shows that as the exposure time of the detector increases the dark pixel count across all 1024 pixels increases. At low exposure times ~ 30 to 120 ms the count is close to zero and not significant. However, as is clear from Figure 2.17 (b), at an exposure time of ~ 1 sec one obtains a dark count of approximately 280 counts. Given the detector dynamic range of 2048 counts, this number represents ~14 % of full scale range at a detector temperature of 5°C. For spectra which have low intensity peaks and some continuum present this could be a limiting factor in the determination of positions and intensities of such small peaks. Figure 2.17 (b) shows that, as expected, the mean dark pixel count increases linearly with increasing exposure time. From this graph we see that at low exposure times this relationship, for the 1453 detector used here, does not hold and the signal is below one least significant bit volts corresponding to a charge of ~ 5000 electrons. It was also noted

during operation that the detector saturation count is 1786 rather than 2048. The observed deviation is likely to be due to (i) the 1453 amplifier gain is too low, (ii) a negative offset voltage may be sitting on the video signal or (iii) a combination of both factors. The existence of an offset voltage is strongly supported by the observation of an offset in the Figure 2.17 (b) where a signal count of zero is obtained for exposure times < 120 msec. Using 2.17 (b) the intercept is -35 counts. Adding this to 1786 gives a saturation count of 1821. Hence in addition to the observed offset the gain is only 89 % of its ideal value.

There is also fixed pattern noise present in each of the data sets in Figure 2.17 (a). This effect can be removed by subtracting a second dark scan at the same exposure time leaving only the true random noise on the difference signal. Figure 2.18 shows such difference scans (centred at zero counts), but with an off-set of 50 counts added to each data set so that the magnitude and level of variation can be examined for each exposure time. From this plot you can see that the random noise on the detector array is visibly increasing with exposure time, as expected from equation 2.2 which shows that the dark current shot noise is proportional to the exposure time t_i.

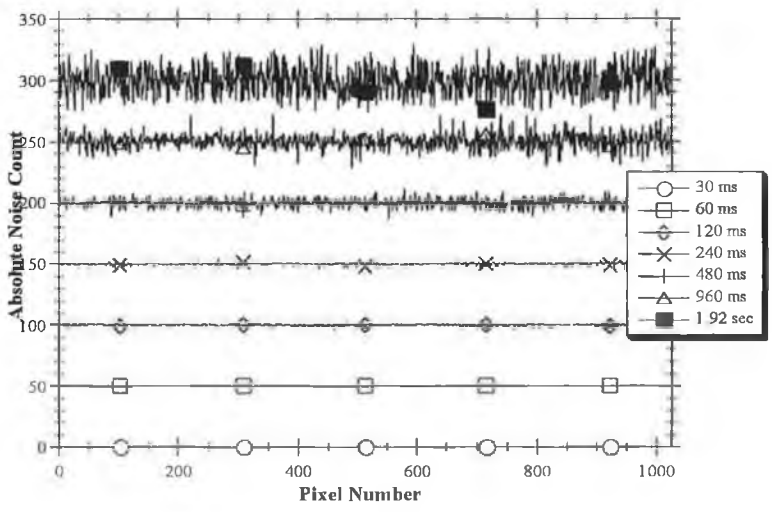

Figure 2.18 Random noise on PDA

The relationship between the mean square value of the shot noise current i_{nd} and the mean dark current is given by the expression

$$\overline{i_{n_d}^2} = 2e\overline{I_d}\,\Delta f \qquad (2.6)$$

where Δf is the bandwidth of the detector, e the electronic charge and $\overline{I_d}$ the mean dark current. If the noise in the detection system is truly random shot noise then the above relationship is valid and the only source of noise is the shot noise on the dark current then a plot of the RMS noise versus the square root of the dark current should yield a straight line. This is relationship is plotted in Figure 2.19 below.

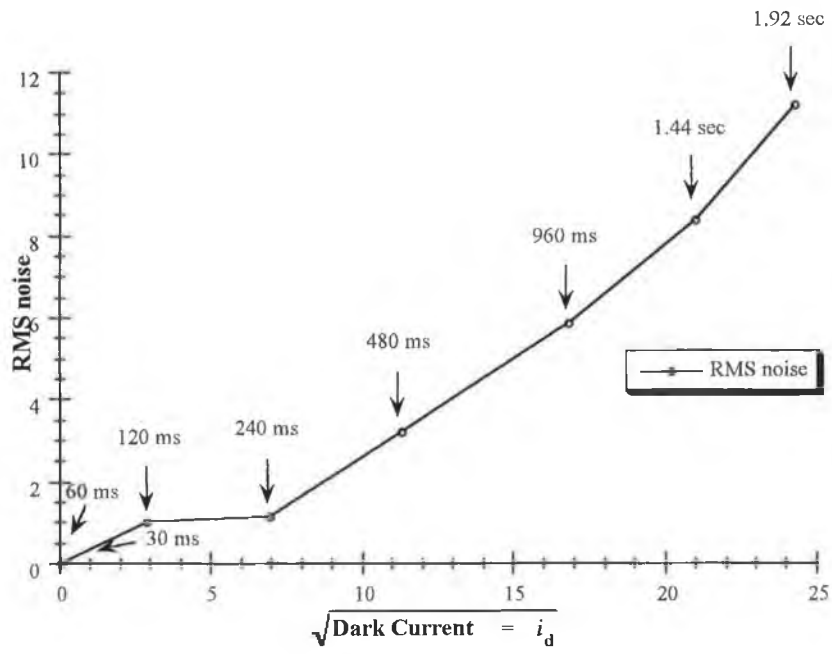

Figure 2.19 Relationship between the R.M.S noise and dark current

From this graph we see for exposure times between 240 and 1920 ms we have an approximate linear relationship. At exposure times below 240ms, this relationship does not appear to be linear. However due to the above mentioned offset in the video signal one cannot reliably use data below the 240 ms exposure time. The trend in Figure 2.19 indicates noise increasing more than linearly with exposure time and hence noise, sensitive to exposure time and above shot noise is clearly present. Such additional noise sources could be e.g., thermal in origin.

In the above graphs we have looked at the noise on the detector array for various different exposure times for single scans. The following data illustrates the effect of averaging scans and how this affects the noise levels on the array readout signals. A series of measurements were made in which a number of scans at the same exposure time (480 ms) were taken for different numbers of scans. This series of scans were averaged for each measurement made. To examine the averaging effect on the random noise levels a second series of measurements were made at the same exposure time and subtracted from corresponding first scans. Figure 2.20 (a) shows

the random noise levels across the detector array for various different sets of subtracted scans at an exposure time of 480 ms. From the plot it is obvious that by video signal averaging we reduce the random noise level. This is an important observation and one which was used in taking spectra i.e., improve the data SNR. This is important especially in the case of mean spectra where poor SNR makes it difficult to distinguish real peaks from noise peaks. Further, poor SNR can also cause spurious results (false peaks) when deconvolution techniques e.g., Fourier methods (see chapters 3 and 4) are applied to data sets. Figure 2.20 (b) demonstrates the relationship between the RMS noise and the number of scans. The graph shows that the RMS noise, as expected, is inversely proportional to the square root of the number of scans. The high degree of linearity in this plot indicates the absence of fixed pattern noise as it has been subtracted out leaving only truly random noise present on the data.

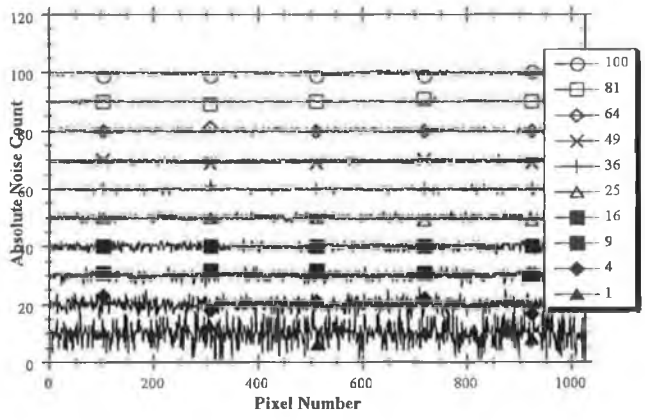

2.20 (a)

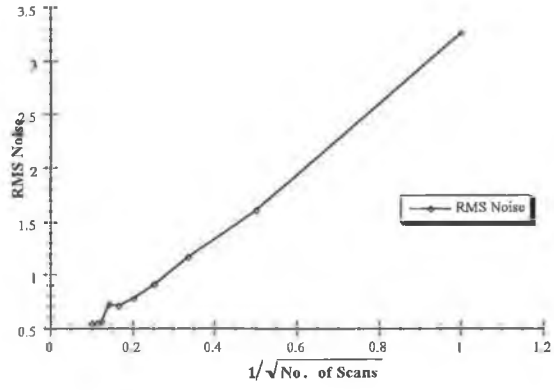

2.20 (b)

Figure 2.20 (a) Plot of absolute noise count vs. pixel for different numbers of scans averaged and subtracted. (b) Relationship between the r.m.s noise and no. of scans of the detector array. NOTE : each data set in graph (a) has been off-set by 10 counts clarity. The exposure time for all these scans is 480 ms.

From the above analysis of the noise from the detector array we can say that in order to minimise the amount of noise observed we must minimise the exposure time if possible and also use data subtraction and averaging to get rid of both random noise (shot, amplifier, etc.) and fixed pattern noise.

2.4.3 SINGLE SHOT SENSITIVITY .VS. MULTI-SHOT AVERAGED SPECTRA

With source and detector noise present in the spectrometer system, an experiment was carried out which recorded single and multi-laser shot averaged spectra of Aluminium Oxide (AlO). This was done to examine the single .vs. multiple shot performance of the multichannel spectrometer system. Figure 2.21 shows a single shot emission spectrum taken using AlO as a target material (exposure time used was 30 ms). The lines in this spectrum were identified using the tables of Kelly [1987]. The spectrum shows that the spectrometer is capable of clearly resolving closely spaced lines e.g., the O VI doublet at 173Å and also that the detector is very sensitive to XUV radiation with both good spatial resolution and photodiode sensitivity (i.e. photons/count). The presence of low ion stages of aluminium and oxygen and the fact that very little continuum is present indicate that the spectrometer is looking at the cool part of the laser plasma plume, some distance away from the target surface and that for this particular experiment the power density of the laser is low. From these observations we see that the laser plasma/spectrometer/detector combination provides single shot sensitivity. It should also be noted that such sensitivity is observed right throughout the 25 -> 180 eV photon energy range of the system [Kennedy *et al* 1994].

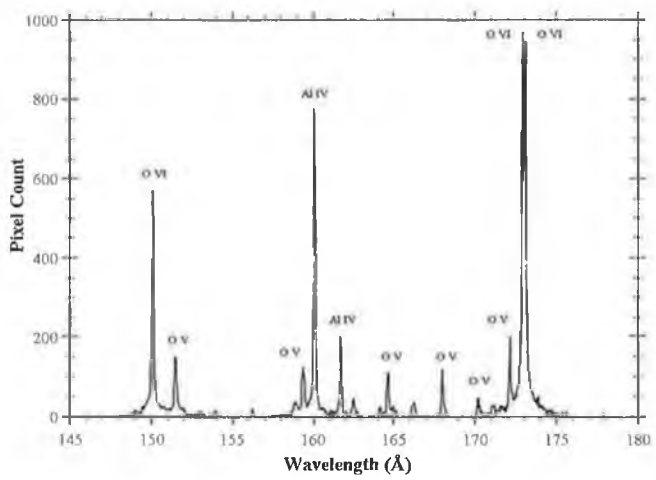

Figure 2.21 AlO spectrum showing the single shot sensitivity of system.

If the experiment is repeated for multiple accumulated laser shots it is clear from Figure 2.22 that the resolution is unaffected by multiple shot averaging and is an indication of very good mechanical stability of the spectrometer system. This is most likely due to the good anti-vibration design of the system e.g. granite base, damping legs, etc.

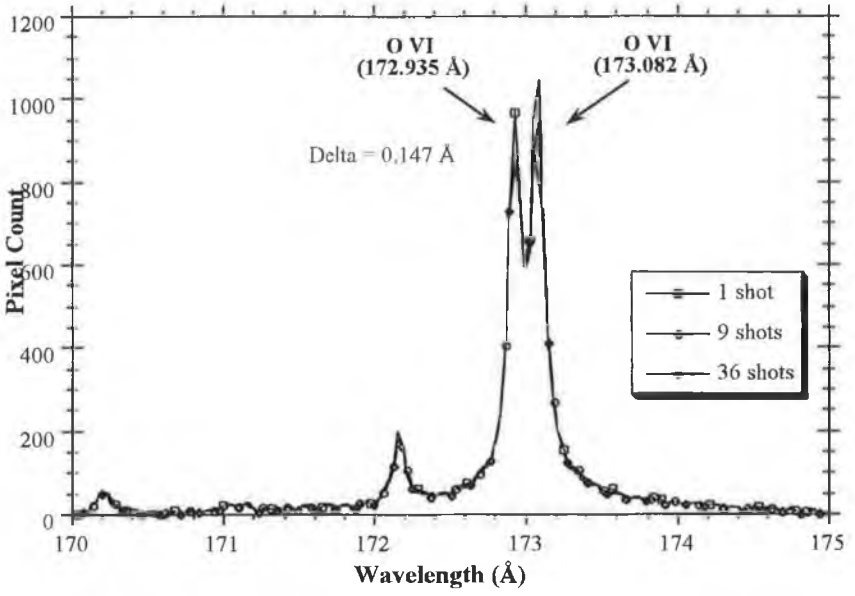

Figure 2.22 Effects of multiple shot averaging.

For each spectrum above, we see that there appears to be a reduction in the intensity of the doublet lines with increasing number of scans averaged. This is most likely due to the occlusion of the plasma by the hole/pit generated in the target each time the laser hits the target.

2.4.4 PHOTOABSORPTION PERFORMANCE

The following section describes the capabilities of the system for looking at photoabsorption spectra using a laser plasma continuum light source. To highlight this potential an experiment was carried out to look at photoabsorption in helium gas, near the K edge at ~ 500 Å corresponding to direct photoionisation and at ~ 206 Å corresponding to double electron excitation. The spectra below were produced by allowing Helium gas into the laser plasma target chamber. The continuum light is provided by a laser generated tungsten plasma which acts as the backlighting source (I_o). Figure 2.23 shows a tungsten continuum spectrum covering the full array in the wavelength range close to 500 Å.

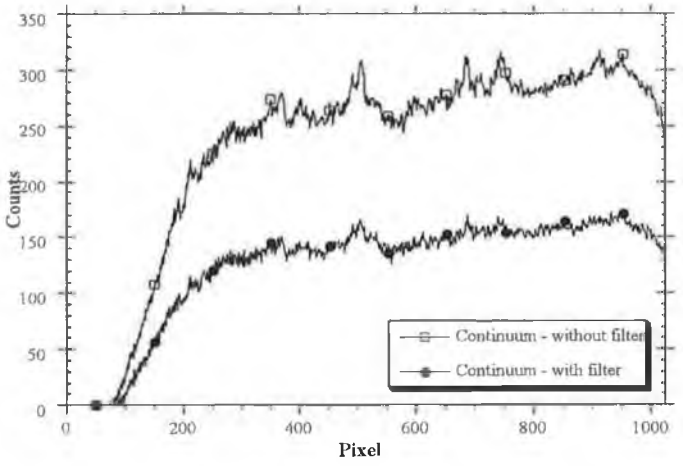

Figure 2.23 XUV continuum emission spectra (10 shots accumulated) of a YAG generated tungsten plasma in the 500 Å region with and with out an aluminium thin film filter.

Figure 2.23 shows that tungsten is a suitable backlighting source due to its broad emitting spectral range, almost completely line free continuum emission in the XUV and its relatively low mass ablation rate. There are some self absorption features present in these spectra but the intensities and positions of these features are stable and so tend to divide out. The low continuum signal of ~ 300 counts is expected as 500 Å is almost 400 Å distant from the blaze wavelength of 84 Å. Note; at the long wavelength end of the spectrum the rapid fall-off in intensity is due to shadowing of the detector by the fully extended bellows.

In photoabsorption spectroscopy two phenomena which affect the measured transmission (I / I_0) are scattered light and overlapping higher spectral orders. These effects can be minimised by using thin film foils which have spectral windows and act as bandpass filters in well defined energy ranges. Figure 2.23 shows the same spectra taken with and without one of these thin film foils. The foil used here is a 2000 Å Al foil mounted on copper wire mesh to support it. It is inserted between the source and the toroidal mirror chamber (see Figure 2.1). Aluminium is a good foil to use as it is durable and easier to process than many other filter materials. It has a wide bandpass (from 170 Å to 800 Å) and is excellent for visible light rejection [Powell *et al* 1990]. The absorption coefficient of Al at ~ 500 Å is ~ 5 μm^{-1}. For a 2000 Å filter, this corresponds to a transmission of < 40 %. However the measured transmission of ~ 55% indicates additional light above the first order continuum falling on the detector. This postulate may be seen by considering the following. Suppose a sample has 40 % transmission, $T = I / I_0 = 0.4$. Now consider an additional contribution to I_0 (due to superimposed scattered light or higher order

light) is represented by I′. With the Al filter in place I has I′′, possibly less than I′, superimposed. Then the transmission is 55% as opposed to 40 % expected.

$$T' = \frac{I + I''}{I_o + I'} \tag{2.7}$$

Dividing equation 2.7 by I_o we get

$$= \frac{I/I_o + I''/I_o}{1 + I'/I_o} \tag{2.8}$$

Our expression for T' then becomes

$$T' = \frac{T + I''/I_o}{1 + I'/I_o} \tag{2.9}$$

Substituting our values from above this expression becomes

$$0.55 = \frac{0.4 + I''/I_o}{1 + I'/I_o} \tag{2.10}$$

$$= \frac{0.4 + S''}{1 + S'} \tag{2.11}$$

where I''/I_o (S") is the transmitted additional light and I'/I_o (S') is the incident additional light.

With the Al filter in place one would expect S' to be substantially greater than S". Taking say S' = 0.2 we obtain S" ~ 0.04 as a typical example which confirms this expectation. For S' = 0.1 we obtain S" ~ 0.1 also which would appear to be unphysical and hence we conclude that there must be a substantial component of additional light on the I_o at ~ 500 Å which is significantly reduced on the I.

The general signature of the above spectra is in good agreement with the measurements of Bridges *et al* [1986] and highlights also the shot to shot reproducibility of the backlighting spectrum. This is a key requirement for obtaining reliable cross-section data. Measurements made by Kennedy *et al* [1994] have shown that shot to shot variations may be kept below 2% by paying careful attention to the tungsten target alignment and surface preparation details.

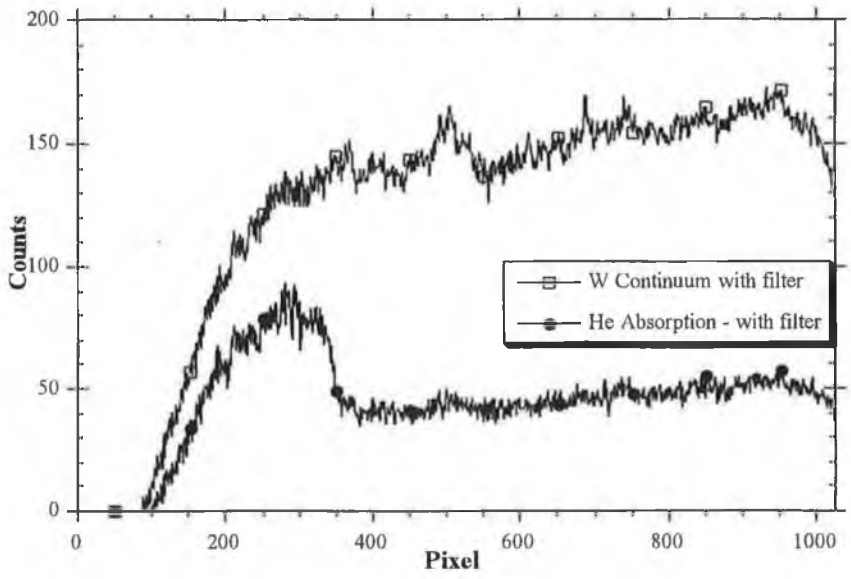

Figure 2.24 Tungsten Continuum (I_0) and He photoabsorption (I) at the 500 Å (~25 eV) edge

Figure 2.24 again shows the continuum spectrum of tungsten in the 500 Å region and underneath it the absorption spectrum obtained by allowing helium gas to flow into the chamber. The spectrum clearly shows the K-edge of helium at 500 Å.

Figures 2.23 and 2.24 show the spectra as they were recorded on the detector. To obtain relative and absolute cross-section information about the species we are examining we must take the ratio of I to I_0. The relative cross-section can then be determined by calculating $Ln\ (I_0/I) = \sigma nl$, where σ is the cross section (cm^2), n is the number density of the absorbing species (cm^{-3}) and l is the length of the absorbing column (cm). The plots below (Figures 2.25 and 2.26) show the relative and absolute cross-sections of helium as a function of pressure and for different wavelengths and with and without foils.

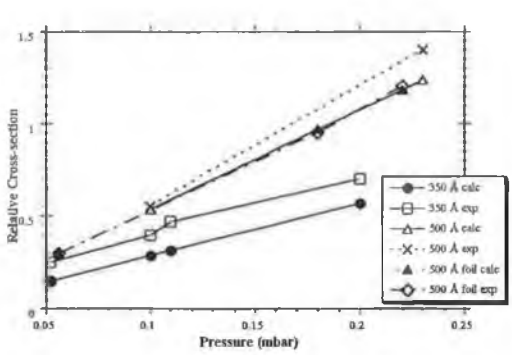

Figure 2.25 Relative cross-section data for Helium at different energies with and without Al filters.

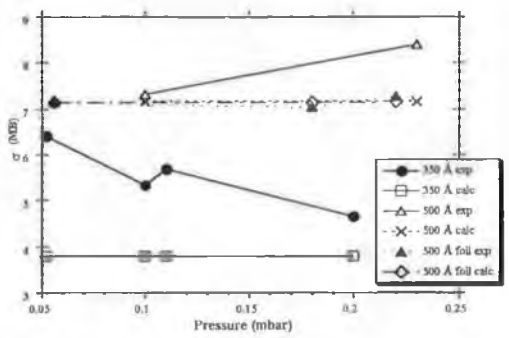

Figure 2.26 Absolute cross-section data for Helium at different energies with and without Al filters.

The data in Figure 2.25 indicates that as we increase the pressure, while keeping σl remains constant the relative cross section increases, as expected from expression $Ln\ (I_0/I) = \sigma nl$. For comparison purposes the calculated data are also plotted for selected wavelengths and pressures of He gas. We know l and can calculate n from the ideal gas equation, PV=nRT, where P is pressure in mbar, V is volume in litres, n is the number of moles, R is the universal gas constant and T is the temperature in degrees Kelvin and the values for σ are tabulated [Kennedy and Manson 1972]. The discrepancy between calculated and experimental data can be explained by previously discussed effects of scattered light and order sorting. The use of XUV filters helps eliminate this discrepancy and this can be seen in Figure 2.25 where the calculated and experimental values for the relative cross sections agree. The filter reduces scattered light (for $\lambda > 800$ Å) and also can assist on higher order light reduction by suppressing light below 180 Å. Scattered light is the result of laser-plasma radiation specularly reflected from shiny surfaces (e.g., optics, slits, bellows etc.) in the spectrometer and falling on the detector plane. Higher order light is simply explained by the grating equation $m\lambda = d (\sin \alpha + \sin \beta)$. For a given angle of incidence α and diffraction β, $m\lambda$ = const. Hence at the observation angle β, λ appears in first order (m=1), λ/2 in second order (m=2) etc. For example, with the above experimental system when we measure light at 350 Å first order, we also get second and third order light at ~ 175 Å and ~ 117 Å all at the same pixel number. This can add to the signal on the detector and give a higher incident (and transmitted) intensity than if just the first order (350 Å) were present. Figure 2.26 above shows the effect of scattered light/higher orders splitting as we see that according to this graph the cross section varies with pressure, which is an unphysical effect. In order to understand this observation consider the following. It is clear from Figure 2.23 and 2.24 that $T' < T$ at all wavelengths in the absence of the Al filter. This occurs when light other than first order radiation impinges on the photodetector. The modulated transmission T', from equation 2.9, is given by

$$T' = \frac{T + I''/I_o}{1 + I'/I_o}$$

where I" and I' are additional light contributions to I and I_o respectively. At 0.2 mbar and $\lambda = 350$ Å, T = 0.57 and T' = 0.5. Substituting into expression above gives

$$T' = 0.5 = \frac{T + I''/I_o}{1 + I'/I_o} = \frac{0.57 + S'}{1 + S'}$$

which implies

$$S'' = 0.5S' + 0.07$$

Substituting S' = 0.2 yields S" = 0.03 in expectedly good agreement with the values obtained in the Al filter absorption experiment. The further reduction in S" is likely to the result of enhanced attenuation of S" by the He gas. However the relative contributions of scattered light .vs. higher (2nd order) light have not been determined.

Finally an experiment was carried out to look at the photoabsorption spectrum of helium in the wavelength range corresponding to double-electron excitation $1s^2 \rightarrow$ 2snp (~ 200 Å) [Madden and Codling 1963, Domke *et al* 1991]. This spectrum is shown in Figure 2.27 and shows the asymmetric nature of the resonances which is due to the interaction between the doubly excited state and the underlying direct photoionisation continuum producing an interference effect in the cross section. This series is shown in the energy region ~ 100 Å to ~ 215 Å in figure 2.27, where up to the fifth member is clearly visible.

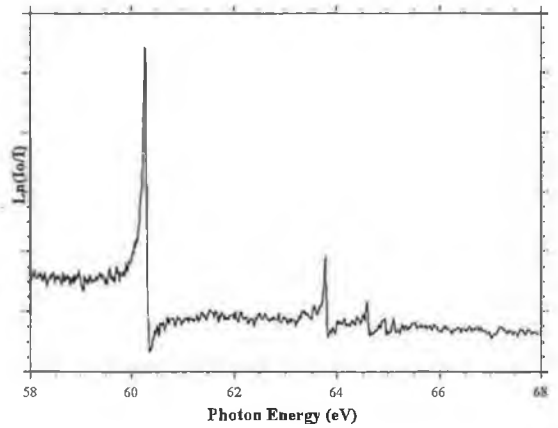

Figure 2.27 Photoabsorption spectrum of helium gas in the vicinity of the $1s^2(^1S) \rightarrow$ 2snp (^1P) doubly excited resonances.

An important point to note in the measurement of the helium photoabsorption cross section is the insensitivity of the continuum output of the backlighting plasma to the ambient helium pressure. Also, the first member does not display a zero in the cross-section at ~ 60.2 eV. This is due to the limited resolution of the system and is discussed further in Chapter 4.

REFERENCES

Bridges J.M., Cromer C.L. and McIlrath T., Appl. Opt., Vol. **25**, No. 13, (1986).

Carroll, P.K., Kennedy, E.T. , Phys. Rev. Lett. **38**, 1068 (1977).

Callcot T.A., Ederer D.L. and Arakawa E.T., Nucl. Inst and Meths. in Physics. Res. A266, North Holland, Amsterdam,578,(1988).

Costello *et al*, Phys Scr. Review Paper. (1991).

Cromer C.L., Bridges J. M., Roberts J.R. and Lucarto T. B., Appl. Opt., Vol. **24,** No. 18, (1985).

Domke, M., Xue, C., Pushmann, A., Mandel, T., Hudson, E., Shirley, D.A., Kaindl, G., Greene, C.H., Sadeghpour, H.R. and Petersen, H., Phys. Rev. Lett. **66** 1306 (1991).

EG&G PARC™ Model 1461 Detector Interface Instruction Manual (1990).

EG&G PARC™ Model 1462 Detector Controller and Model 1462/99 14-BIT A/D Converter Operating and Service Manual (1984).

EG&G PARC™ Model 1461/88 Applications Program Instruction Manual (1989).

Kelly R.L., "Atomic and ionic lines below 2000 angstroms : Hydrogen through Krypton", Part I (H-Cr), Part II (Mn-Kr) and Part III (Finding List), J. Physical & Chem. Ref. Data, Vol **16,** supplement No.1, (1987).

Kiernan, L., PhD. Thesis, Dublin City University (1994).

Kennedy *et al*, SPIE, 1994.

Kennedy, D.J. and Manson, S.T., Phys. Rev. A. **J 1** 227 (1972)

Lynam, W.G., Caroll, P.K., Costello, J.T., Evans, D., O'Sullivan, G., J. Phys. B., **25** 3963 (1992).

Mack, J.E., Stehn, J.R. and Edlen, B., J. Opt. Soc. Am., **22**, 245, (1932).

Madden, R.P. and Codling, K., Phys. Rev. Lett. **10** 516 (1963)

McPherson ™, "Instruction Manual for 2.2 Metre Grazing Incidence Vacuum UV Monchromator", (1992).

NATIONAL INSTRUMENTS : GPIB-PC User Manual for the IBM Personal Computer and Compatibles. (April 1988 Ed.) NATIONAL INSTRUMENTS CORP.

Powell F.R., Vedder P.W., Lindblom J.F and Powell S.F., Opt. Eng, Vol **29**, No. 6 (1990).

Samson J. A., 'Techniques of Vacuum Ultraviolet Spectroscopy', Wiley & Sons (1967).
Schwob, J.L., Wouters, A.W., Suckewer, S., Rev. Sci. Instrum. **58** 1601 (1987)
Simpson, R.W., Rev. Sci. Inst., **50** 730 (1979)
Talmi, Y. and Simpson, R.W., App. Opt. **19** 1401 (1980)
Wiza J.L., Nucl. Inst. and Meths, Vol **162,** 587, (1979)

Chapter 3

Theory of Deconvolution of Instrumental Broadening Effects in Spectral Data

CHAPTER 3 : THEORY OF DECONVOLUTION OF INSTRUMENTAL BROADENING EFFECTS IN SPECTRAL DATA

3.1 INTRODUCTION

Spreading, blurring, and mixing are qualitative terms used to describe the degrading of images due to aberations in imaging optics and the finite spatial resolution of recording media. For example the human eye sometimes 'sees' blurred images due to physical and/or physiological effect/defects e.g diffraction limit by the pupil/lens, aberations due to lens shape, retinal damage etc. Like the human eye all other optical instruments are similarly limited in the fine spatial detail of an object which they can resolve. Convolution provides a mathematical framework in which to compute the combined effect of each individual contribution to image blurring by complex optical instruments (e.g a spectrometer) and constitutes a key idea of the present chapter.

Within spectroscopy there are a number of forms of spectral line spreading or blurring due both to the physical process giving rise to the line and also to the limited resolution of the spectrometer/detector combination being used to measure the line profile. It is intuitively obvious that little can be done to eliminate or reduce physical broadening without interfering with the process itself. On the other hand, a knowledge of how the spectrometer-detector combination broadens a spectrum line should provide us with a means of removing such instrumental broadening. In fact a number of spectral image restoration techniques have been developed using this intuitive idea and will be discussed later in this chapter.

The study of line profiles in laser-produced plasmas has provided the most important diagnostic technique of the last 25 years. Critical to many of these studies has been the removal of additional instrumental broadening. Hence a brief outline of a number of spectral line broadening mechanisms in laser produced plasmas seems a pertinent starting point for this chapter.

3.2 PHYSICAL LINE BROADENING EFFECTS

A laser produced plasma consists of a collection of electrons and ions undergoing a random thermal motion within a plasma plume superimposed on the bulk directed motion of the plume away from the solid target surface. In certain laser plasma experiments it has been observed that, although thermal Doppler broadening is a

relatively small contributary factor to observed line widths, ion-motional Doppler effects result in broad asymmetric line shapes [E.G., Iglesias and Greim 1988]. However for most experiments, due to the potentially high electron and ion densities (particularly in the plasma core), one must conclude that both electron-impact and quasi-static Stark broadening (due to ions) are potentially the most significant line broadening mechanisms. We discuss briefly in the following subsections the typical relative contributions of each of natural, Doppler and Stark broadening effects.

3.2.1 INHERENT LINE BROADENING EFFECTS

3.2.1.1 NATURAL LINE BROADENING

This is due to the finite lifetime Δt_i of any atom in any excited state E_i. As a result of this naturally occurring phenomenon, Heisenberg's Uncertainty Principle says that there will be an uncertainty ΔE_i in the value of E_i given by

$$\Delta E_i \Delta t_i = h/2\pi \tag{3.1}$$

where h is Planck's constant. For resonance transitions in which the lower level is the ground state and hence $\Delta t \rightarrow \infty$ and $\Delta E \rightarrow 0$ we need only consider the upper state lifetime. For a line originating from transitions between excited states we must consider the total broadening to results from the superpostion of each ΔE_i , ΔE_f

For example consider a resonant transition with $\Delta t \approx 10^{-12}$ sec.

$$\begin{aligned} \Delta E &= h/(2\pi \times \Delta t) \\ &= 1.056 \times 10^{-22} \text{ J} \\ &= 6.6 \times 10^{-4} \text{ eV} \end{aligned}$$

As $\Delta E < 1$ meV it is clear that for typical linewidths of > 100 meV measured in VUV spectra of laser produced plasmas that this makes an insignificant contribution.

3.2.1.2 DOPPLER BROADENING

As referred to above this physical broadening effect makes two contributions in the case of an expanding laser produced plume.

(1) Due to the random thermal motion of emitting ions within the plasma plume which should result in a symmetric Gaussian profile e.g in an Al plasma with a temperature of say 50 eV (~ 6 x 10^5K) (see Kirkbright 1974)

$$\Delta\lambda / \lambda = \sqrt{(2kT\ ln2) / mc^2} \qquad (3.2)$$

$$= \sqrt{(2 \times 1.38 \times 10^{-23} \times 6 \times 10^5 \times 0.693) / (26 \times 1.67 \times 10^{-27} \times 9 \times 10^{16})}$$

$$= 5.5 \times 10^{-5}$$

For a typical XUV line say Al VII 250 Å doublet

$$\Rightarrow \Delta\lambda = 0.013 \text{ Å}$$

which is small in comparison to the measured width of ~ 0.1 Å.

(2) However ion-motional or 'hydrodynamic' Doppler broadening can in some cases be many times greater than the above and hence account for the bulk of the observed width of a line [Iglesias and Griem 1988] (in those cases where obviously Instrumental/Stark broadening cannot be invoked as an explanation). A simple Doppler shift calculation for an ion expansion velocity of ~10^5 m/sec yields $\Delta\lambda / \lambda \sim 3 \times 10^{-4}$ and $\Delta\lambda \sim 0.1$ Å at 200 Å, which is not too different from typical observed widths ($\Delta\lambda / \lambda \sim 3 \times 10^{-4}$). Although in many cases a combination of Doppler and Stark broadening mechanisms must be invoked to explain observed profiles [Nicolosi *et al* 1979], some experiments have been able to isolate regions of Stark domination close to the target and of ion-motional Doppler domination in the expanding plume [Irons *et al* 1972]. In this case sophisticated computer models must be used to compute observed line profiles.

3.2.1.3 STARK BROADENING

It is well known that placing an atom in an intense electric field leads to a redistribution of the atomic energy levels with a resultant effect on the observed spectrum of such an excited atom. In laser produced plasmas intense microfields are present which can result in such quasi static broadening of atomic/ionic spectrum lines. For hydrogen and hydrogenic ions the full width half maximum (FWHM) for a line at a centre wavelength λ_o is given by [Befeki - 1976]

$$\Delta\lambda_{1/2} = 8.11 \times 10^{-18} \times (1-0.7\, N_D^{-1/3}) \times \lambda_o^2 \times (n_1^2 - n_2^2) \times ((Z_p)^{1/3} / Z_e) \times N_e^{2/3} \text{ Å}$$

(3.3)

where n_1 and n_2 are the principal quantum numbers of the upper and lower atomic states and N_e is the electron density given by

$$N_e = \text{No. of particles in the Debye Sphere}$$

$$= 1.72 \times 10^{12} \frac{[T\,(eV)]^{3/2}}{[N(m^{-3})]^{3/2}} \qquad (3.4)$$

Z_e is the nuclear charge ($Z_e = 1$ for Hydrogen). Z_p is the charge on the perturbing ion and the other symbols have the usual meanings. For example for H_β at 4861 Å with $N_D = 10^{16}$ cm^{-3} and T = 4eV gives,

$$\Delta\lambda_{1/2} \approx 9.3 \text{ Å}$$

which is substantially greater than thermal Doppler broadening. However in a hot expanding plasma plume the effect of energetic electrons colliding with ion emitters must be accounted for. The details of such calculations are non-trivial, require a knowledge of the atomic structure of the emitting species and are discussed in some detail by [Griem 1974]. For the simple case of Hydrogen Lyman - α, the collisional half-width is given by

$$\Delta\lambda_{1/2}\,(\text{impact}) \approx 1.62 \times 10^{-17} N_e / T^{1/2} [13.76 - \ln (N_e^{1/2} / T)] \text{ Å} \qquad (3.5)$$

where T = plasma temperature in Kelvin and N_e = electron density in cm^{-3} . For a hydrogen plasma with an electron temperature of 50 eV and density of 10^{18} cm^{-3} , $\Delta\lambda \approx$ 0.15 Å. At long times (μs 's) after plasma ignition and / or at significant distances from the plasma core neutral and singly ionised species are dominant. In this case Stark broadening may be computed using Griem [1974]

$$\Delta\lambda_{1/2} = \underbrace{2\,W(N_e / 10^{16})}_{\text{(electron impact contribution)}} + \underbrace{3.5\,A(N_e / 10^{16})[1 - \alpha N_D^{-1/3}] \times W(N_e / 10^{16})}_{\text{(ion field correction)}} \text{ Å}$$

(3.6)

where $\alpha = 0.75$ for atoms and 1.2 for singly charged ions and W and A are so called Stark broadening parameters [cf. Table 13.3 of Befeki for example data]. For an aluminium plasma with $N_e \approx 10^{17}$ cm^{-3} and $T_e \approx$ and 0.7 eV $\Delta\lambda \approx 14$ Å is obtained from the measurement of the 5593 Å line [Knudson *et al* 1987] .

It is clear from the above discussion that both ion-motional Doppler boadening and Stark broadening are the two main physical effects which determine the shape of emission lines from laser produced plasmas. However, the relative contributions of each mechanism depend on the region of plasma viewed and the time of observation after plasma ignition. Further Stark effects depend not only on space / time dependent parameters (e.g, electron/ion density, temperature etc.) but also on the detailed atomic parameters of the line studied. However it is clear that time and space resolved studies of line profiles are critically important to the study of laser plasma physics. In the next section we discuss how instrumental broadening effects on measured profiles may be reduced using three different deconvolution techniques.

3.3 DECONVOLUTION TECHNIQUES

Every measurement instrument adds something of its own characteristics to the measurand. Eliminating at least in part, that extra something that blurs our vision of the measurand is the motivation for developing the art of deconvolution. A true spectrum can be thought of as having a comb like appearance. When observing this spectrum with a spectrometer, it distorts the shape and dimension of the spectral lines, and if the resolution of the spectrometer is substantially less than the spacing between the spectral lines it will "wash-out" the comb like appearance of the true spectrum.

It is intuitively obvious that if one has a detailed knowledge of how an instrument distorts a spectrum that this information should permit the restoration of the spectral image (not withstanding any limitations imposed by the accuracy of the algorithm used, complete loss of spatial frequency information in selected bands, signal to noise ratio of the recorded data etc.). Since a measured spectrum can be thought of as consisting of the 'original' spectrum convolved with a 'distorting' function, the art of spectral image restoration can be considered as the deconvolution of the distorting function from the measured data. In the following section three commonly used restoration techniques will be reviewed : 3.3.1 Fourier Deconvolution [Michaelian and Friesen 1987], 3.3.2 Constrained Non-Linear Deconvolution [Blass and Hassley 1981] and 3.3.3 Maximum Likelihood Deconvolution [Frieden 1983]. The Fourier transform method will be

discussed first as it illustrates most clearly many of the fundamental concepts underpinning image restoartion via deconvolution.

3.3.1 FOURIER DECONVOLUTION

Before starting the analysis of the Fourier Deconvolution method it is important to realise what advantages there are to using the Fourier (or spatial frequency) domain.

The advantages are;

1) In the way that we can view electrical signals in either the time and frequency domain we can view images in the space or spatial frequency domain. For example, the diffraction pattern of a square aperture is simply the Fourier Transform of the aperture shape and hence both the shape and its diffraction pattern are interchangable representatives of the same entity.

2) Many processes which degrade experimental data are often manifested largely in the higher frequency portion of the Fourier spectrum. The fact that much of the error may be localised in a narrow band of high-frequencies, along with the fact that this band may be adequately represented by a small number of discrete spectral components allows considerable reduction of the computation burden of restoration.

3) Many of the physical processes that affect optical images and many other types of experimental data have a simpler mathematical form in Fourier space. For example convolution of two functions in the time/pixel domain is equivalent to multiplication in the frequency (Fourier) domain.

4) With the improvements made in the computational efficiency of the Discrete Fourier transform for large data sets; Fourier Deconvolution can be significantly faster than other methods of computation.

Fourier deconvolution can estimate a more highly resolved spectrum in the following way. The effect of Instrumental broadening can be modelled as the convolution of the true spectrum $\mathbf{O(x)} = \{o_1, o_2, \ldots\ldots, o_n\}$ with the instrument function $\mathbf{M(x)} = \{m_1, m_2, \ldots\ldots, m_n\}$,

$$I(x) = M(x) \otimes O(x) \tag{3.7}$$

where $\otimes$ denotes convolution,

$$I(x) = \int_{-\infty}^{+\infty} M(x - x') \otimes O(x) dx' \tag{3.8}$$

where I(x) is the observed image spectrum, O(x) is the true spectrum and M(x) is the instrument Function (typically a peaked function which falls to zero in both directions from its maximum).

The convolution integral (3.8), can be greatly simplified if it is expressed in terms of the Fourier transform of the functions involved.

$$F[I(x)] = F[M(x)] * F[O(x)] \tag{3.9}$$

where F denotes Fourier Transform and where * denotes multiplication. Since convolution in the pixel domain is equal to multiplication in the frequency domain this means (3.9) can be written as

$$I(\upsilon_x) = M(\upsilon_x) * O(\upsilon_x) \tag{3.10}$$

where $I(\upsilon_x)$, $M(\upsilon_x)$, $O(\upsilon_x)$ are the Fourier transforms the quantities defined in equation 3.7. Now the process of deconvolution becomes a simple matter of division.

$$O'(x) = F^{-1}[O(\upsilon)] = F^{-1}\left[\frac{I(\upsilon)}{M(\upsilon)}\right] \tag{3.11}$$

where $F^{-1}[\ ]$ is Inverse Fourier transform and O' (x) is the estimated true spectrum.

In words this means that if the Fourier transform of the observed spectrum is divided by the Fourier transform of the instrument function the result can be inverse transformed to ideally get back the true spectrum (inverse filtering). In practise things are not so easy; there are two problems associated with the model.

The first problem is due to noise on the spectrum, which limits the recovery of resolution. Since inverse filtering has by its very nature high gain at high spatial

frequency the restored spectrum can be significantly contaminated by high levels of high spatial frequency noise of the original measured data set and hence has a poor SNR.

The second problem involves the discrete nature of the sampled data set. The data set has in effect been truncated by a rectangular function and an abrupt truncation in the pixel domain results in generation of sidelobes (artifacts) in the restored spectrum. This results from the application of the infinite continuous Fourier transform to a finite discretely sampled data set. These artifacts can be minimised by weighting the deconvolved function I(x) so that the truncation is not abrupt (a process called apodisation). However when this is done there can be a resultant loss in spatial resolution.

These problems can be minimised by considering the following. If we ignore noise for the moment and apply a filter (apodization function) to the measured data I(x) we obtain by Fourier deconvolution of I(x) yields an estimate of the true spectrum O(x) given by

$$O'(x) = \boldsymbol{F}^{-1}\left[\frac{I(\upsilon_x)W(\upsilon_x;L)}{M(\upsilon_x)}\right] \tag{3.12}$$

where $W(\upsilon_x;L)$ is the window function that weights or apodises $1/M(\upsilon)$ and truncates the Fourier integral at $\upsilon_x = L$. The **F**inite **I**mpulse **R**esponse **O**perator (FIRO) is defined as

$$R_S(x;L) = \boldsymbol{F}^{-1}\left[\frac{W(\upsilon_x;L)}{M(\upsilon_x)}\right] \tag{3.13}$$

Eq 3.12 can now be expressed as

$$O'(x) = R_s(x;L) \otimes I(x) \tag{3.14}$$

The expression above enables deconvolution to be visualised in terms of a filter operation in which we restore the spectral image by simple convolution of the FIRO $R_s(x;L)$ with the measured data set I(x).

What has not been considered yet in the above analysis is the presence of noise in the data. If we include noise, the measured spectrum becomes

$$I(x) = M(x) \otimes O(x) + N(x) \tag{3.15}$$

$$= I(x) + N(x)$$

From Eqn 3.14, the restored spectrum is $O'(x) = R_s(x;L) \otimes I(x)$. Substituting Eqn 3.15 into Eqn 3.14 we obtain an expression for the resolved spectrum which is given by

$$O'(x) = R_s(x;L) \otimes I(x) + R_s(x;L) \otimes N(x) \tag{3.16}$$

The W (x;l) (window functions) used in this thesis are

$$\textbf{Triangular} = [\,1 - \frac{x}{L}\,] \tag{3.17}$$

$$\textbf{Boxcar} = 1 \text{ for } |x| \leq 1, \; = 0 \text{ for } |x| > 1 \tag{3.18}$$

$$\textbf{Bessel} = [\,1 - \frac{|x|}{L}\,]^2 \tag{3.19}$$

The width of the filter $W(\upsilon_x;L)$ and the instrument function vary inversely with L while the magnitude of $R_s(x;L) \otimes N(x)$ increases approximately exponentially with L^2 when e.g. M(x) is Gaussian. Thus amplification of noise is an unavoidable consequence of resolution enhancement. Fourier deconvolution is the art of finding the appropriate filter, which gives the best resolution with the minimum of noise.

When noise levels are low simply inverse filtering the data as described above yields a good approximation to O(x). For higher noise levels the increasing noise term rapidly obscures all higher frequency information in the deconvolved spectrum making truncating or filtering of the resulting spectrum necessary to achieve meaningful results. For most data encountered in practice it is found that only a relatively small number of Fourier spectral components are required to represent the spectrum adequately; the higher frequencies being mostly noise.

The reason for getting rid of this noise is that in pixel space it can give an "apparent" increased resolution. With a low noise spectrum it is easier to determine with more certainty the actual resolution. Another reason is that the Fourier deconvolution process is quite sensitive to noise and contributes considerable instability to the solution. If deconvolution is carried out too far in the Fourier domain, serious distortion of the spectral information can result. Too far means that deconvolution is attempted, using Eq

3.17, beyond the point at which the spectral information becomes indistinguishable from the noise.

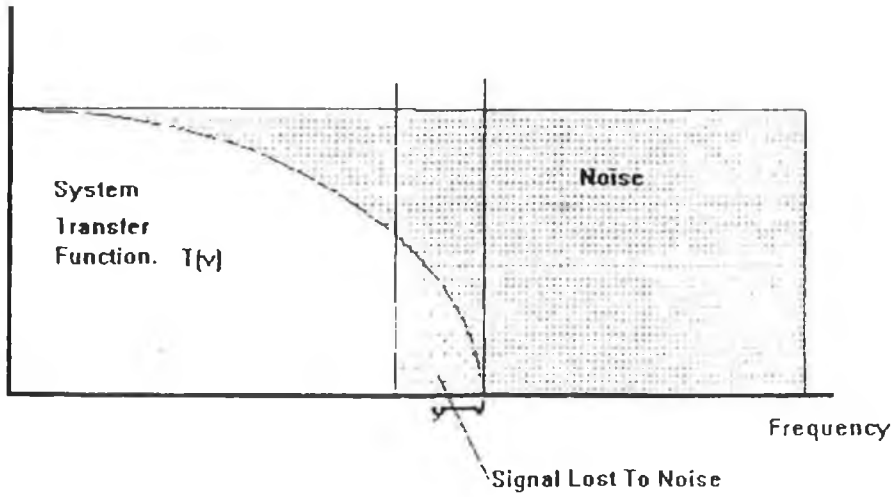

Figure 3.1 Relationship between the instrument function and noise in spatial frequency space.

For this reason it is important to choose an appropriate value of L (the cut off frequency of the filter). Choosing a large value of L results in a higher resolution but increases the noise level on the restored data while conversely a smaller value of L means poorer resolution but less noise also. A method for determining a value for L for a required optimal resolution has been devised [Kauppinen *et al* 1981] and demonstrates that the resolution is highly dependent on the data signal-to-noise ratio (SNR) and on the type of filter used. Thus the optimum combination depends on the user's aims and criteria.

When the SNR is sufficiently high, Fourier deconvolution provides a good result. Moreover, it is easily programmed and also executes quickly. A code written in 'C' has been developed to investigate the FIRO method of Fourier Deconvolution. Some sample results are presented in Chapter 4.

3.3.2 CONSTRAINED NON-LINEAR DECONVOLUTION

This class of deconvolution method involves computation in signal space, i.e. directly on recorded data sets. Van Cittert [1931] is credited with devising the first iterative scheme for the recovery of O(x) (the original undistorted spectrum) from I(x) (the recorded spectrum) directly in signal space. His algorithm may be stated simply as follows :

$$O_n = O_{n-1} + \{I - O_{n-1} \otimes M\} \qquad (3.20)$$

where we drop the continuous variable x. In reality our data set is discrete and x becomes an array index e.g. (i). We use the subscript 'n' to indicate iteration number

The starting assumption is that

$$O_1 = I \tag{3.21}$$

i.e. our first guess at the recorded data set is taken to be the measured data set. However as stated this algorithm has a number of problems mainly associated with convergence [Blass and Hasley 1981].

In order to overcome these problems, Jansson [1970] developed a modified Van Cittert algorithm for which the error factor $\{I - O_{n-1} \otimes M\}$ is multiplied by a relaxation (or weighting) parameter α_n. The modified algorithm now has the form

$$O_n = O_{n-1} + \alpha_n \{I - O_{n-1} \otimes M\} \tag{3.22}$$

As the Van Cittert algorithm involves simple addition, subtraction and convolution it is a linear process. On the other hand, Jansson's modification involves multiplication and hence the often used term that it belongs to the non-linear deconvolution class.

The form of the relaxation parameter α_n is the key to the success of the Jansson-Van-Cittert method. A number of functional forms of α_n have been developed and are summarised below. In Chapter 4 we have used the Blass and Hasley form of the relaxation function to perform deconvolution using this technique.

- Jansson [1970] function can be stated as :

$$\alpha_n = \alpha_{n\,max} [1 - 2 | O_{n-1}(x) - \tfrac{1}{2} |] \tag{3.23}$$

  were $\alpha_{n\,max}$ = const and is triangular in shape and generally used with absorption spectra scaled between 0 and 1.

- Willson [1973] used a quadratic function

$$\alpha_n = 4\, \alpha_{n\,max} \{O_{n-1}(x) - [O_{n-1}(x)]^2\} \tag{3.24a}$$

$$= 4\,\alpha_{n\,max}\,\{O_{n-1}(x)\,[1 - O_{n-1}(x)\,]\} \qquad (3.24b)$$

designed to overcome potential problems with oscillatory behaviour between successive iterations.

- Blass and Hasley [1981] have used the function

$$\alpha_n = \alpha_{n\,max}\,\{O_{n-1}(x)[1 - O_{n-1}(x)\,]\}^p \qquad (3.25)$$

which is similar to Willson except for the value of the exponent 'p' which is fixed at '1' in the case of Willson (ignoring the constant factor of 4).

- Finally Frieden [1975] has given a relaxation function of triangular form which unlike the above three functions may be used with data sets of arbitrary

minimum and maximum values and is stated as ;

$$\alpha_n = \alpha_{n\,max}\,[1 - 2(B-A)^{-1}\,|\,O_{n-1}(x) - \tfrac{1}{2}\,(A+B)\,|\,] \qquad (3.26)$$

where A = maximum and B = minimum value of the data set. For A = 1 and B = 0 the function reduces to Eqn (3.23) above.

In the code developed as part of this these the relaxation functions given by equation 3.23 to 3.26 are included. Details on the application of this code to experimental data sets are given in chapter 4.

3.3.3 MAXIMUM LIKELIHOOD DECONVOLUTION

Every time we measure a spectrum we know that the spectrometer both reveals and distorts the sample spectrum, that noise is added by the detector, and that furthermore, each spectrum is just one example of a statistical process. Therefore the proper question to ask is : What is the most likely sample behaviour that could have produced the observed spectrum given the characteristics I know about my instrument ?

Maximum Likelihood techniques answer this question. They give you the *most probable*

If the noise is random with a Poisson distribution, then the probability for obtaining a particular i_j is

$$p(i_j \mid o) = \frac{(o \otimes m)_j^{\,ij}\, e^{-(o \otimes m)_j}}{i_j!} \tag{3.29}$$

Assume that the noise n_i is uncorrelated with the noise n_j , for i,j. Then the likelihood of observing the set $\{i_1, i_2, \ldots\ldots, i_n\}$ is the product of the probabilities for each of the i_j :

$$p(i_1, i_2, \ldots\ldots, i_n \mid o_1, o_2, \ldots\ldots, o_n) = \prod_{i=1}^{n} p(i_j \mid o) \tag{3.30}$$

For Poisson noise, this becomes

$$p(i_1, i_2, \ldots\ldots, i_n \mid o_1, o_2, \ldots\ldots, o_n) = \prod_{i=1}^{n} \frac{(o \otimes m)_j^{\,ij}\, e^{-(o \otimes m)_j}}{i_j!} \tag{3.31}$$

The Maximum Likelihood Principle says we must maximise **p**, given a set of constraints. The two most important constraints are the instrument function and the signal to noise ratio. This is one advantage with Maximum Likelihood methods that you can include *a priori* constraints other than just the instrument function. This allows for a more robust solution with less probability of spurious results.

There are many data sets $O(x) = \{o_1, o_2, \ldots\ldots, o_n\}$, which, when convolved with the instrumental function $M(x) = \{m_1, m_2, \ldots\ldots, m_n\}$ give a result $M(x) \otimes O(x)$ which conforms to the data *within the limits of the noise*. The question is which solution set is correct ?. One's intuition says that $M(x) \otimes O(x)$ should be a smooth curve that fits somewhere in the middle of the noisy data set $I(x) = \{i_1, i_2, \ldots\ldots, i_n\}$. The noise fluctuations $N(x) = \{n1, n2, \ldots\ldots, n_n\}$ should be nearly evenly distributed between positive and negative values since it is improbable that all the noise fluctuations were negative. In this instance, intuition and Maximum Likelihood are closely related, because both deal with probabilities. From the statistics of the noise, it provides the most probable solution $O(x) = \{o_1, o_2, \ldots\ldots, o_n\}$.

In order to investigate the usefulness of this method and compare it with both Fourier and Jansson techniques a commercial code 'SSRES' piggybacked onto the

SPECTRACALC™ package is used to implement this method and results presented in Chapter 4.

REFERENCES

Befeki G. , *Principles of Laser Plasmas* (Wiley, New York, 1976.)

Blass, W.E. and Hassley, G.W., "Deconvolution of Absorption Spectra", Academic Press (1981).

De Noyer, L.K. and Dodd. I.G., "Maximum Likelihood smoothing of noisy data.", *Am. Lab.* **22** (3), 21-27 (1990).

Frieden B.R., in *Picture Processing and Digital Filtering* (T. S. Huang, ed.), p. 179. Springer Verlag, Berlin and New York, 1975.

Frieden, B.R, J. Opt. Soc. Amer. **73**, 927 (1983).

Griem, H. R. 1974, *Spectral Line Broadening by Plasmas.* Academic. New York.

Iglesias E. J., Greim H.R., Phys. Rev. A. **38**, 301 (1988)

Irons F. E. , McWhirter R. W. P. , Peacock N. J. , 1972 *J. Phys. B: Atomic. molec. Phys.* **5** (1975)

Jansson P.A. , Hunt R. H., Plyer E. K. , *J. Opt. Soc. Am.* **60**, 596 (1970).

Jansson P.A. , *J. Opt. Soc. Am.* **60**, 184 (1970).

Kauppinen J.K, Moffat D.J, Cameron D.G, Mantsch H.H, Appl Opt. **20**, 1866 (1981)

Kirkbright, G.F. and Sargent, M. , in *Atomic Absorption and Fluorescence Spectroscopy*, Academic Press , 1974.

Knudson J. T., Green W.B. , Sutton D. G. , J Appl. Phys. **61**, 4771(1987)

Michaelian, K.H. and Friesen, W.I., Appl. Spec. **42**, 1538 (1987).

Nicolosi P. , Tondello G. , Jannitti E. , Phys. Rev. A. **20**, 2574(1979).

Van Cittert P.H. , Z. *Phys.* **69**, 298 (1931).

Willson P. D. , Ph. D. Thesis, Michigan State Univ., East Lansing, 1973.

Chapter 4

Deconvolution of Emission and Photoabsorption spectra; Comparison of different restoration techniques

CHAPTER 4 :DECONVOLUTION OF EMISSION AND PHOTOABSORPTION SPECTRA; COMPARISON OF DIFFERENT SPECTRAL RESTORATION TECHNIQUES.

4.1 INTRODUCTION

The current chapter presents the results of deconvolution procedures applied to aluminium oxide emission spectra and helium photoabsorption spectra obtained using the 2.2 m spectrometer described in chapter 2. Spectral data are shown which serve to demonstrate the various strengths and weaknesses of three different deconvolution techniques in terms of resolution enhancement, peak recovery and noise performance. The three methods of deconvolution discussed and compared are :

- FOURIER DECONVOLUTION
- CONSTRAINED NON-LINEAR DECONVOLUTION
- MAXIMUM LIKELIHOOD DECONVOLUTION

A spectrum of AlO in the 170 Å to 200 Å region was used as the sample spectrum to deconvolve and inter compare the outcomes of each technique. The spectrum, shown in Figure 4.1,

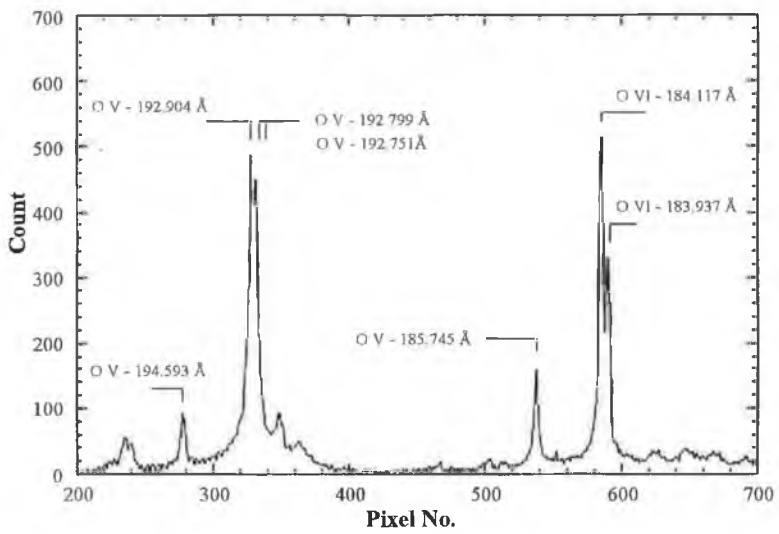

Figure 4.1 Experimental AlO Spectrum in the 170 - 200 Å range.

exhibits a pair of closely spaced doublet features which were examined before and following the application of each spectral restoration technique. The doublet features are located at ~193 Å (pixel position 320) and ~184 Å (pixel position 590). These peaks have been identified using Kelly's tables [1987] and provide good examples of features which are partially resolved and which can further be recovered by deconvolution using an instrumental line shape taken from a spectrum in the same region. The spectrum from which the instrumental function was taken is shown in Figure 4.2 and inset is shown the actual peakshape function used. The spectrum is one of an AlO plasma in the same wavelength region as that shown in Figure 4.1. The line used was an Al IV line at wavelength ~ 161.7 Å ($2s^2\ 2p^6 \rightarrow 2s^2\ 2p^5\ 3s$). The reasons underlying the choice of this line are as follows

- the baseline in this spectrum and for this particular line exhibits a low level of noise and a low continuum radiation level
- it is a single isolated line
- the full width half at maximum (FWHM) for this line is ~ 3.3 pixels which is close to this instruments resolution capability and it can therefore reasonably reliably assumed that the intrinsic linewidth is below that of the instrument

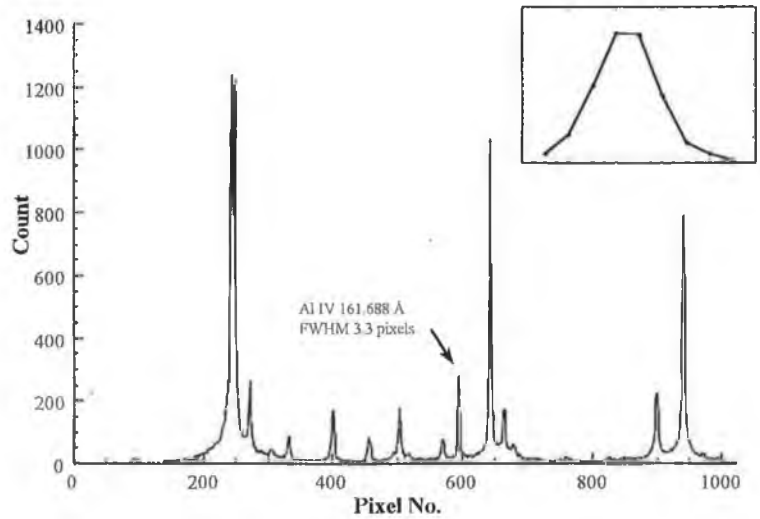

Figure 4.2 AlO Spectrum from which peakshape was measured (peakshape shown inset - contains 10 points FWHM 3.3 pixels)

In an ideal circumstance, the instrument function would represent the true impulse response of the spectrometer with no baseline continuum associated with it. In the present case, it is necessary that baseline subtraction be performed to generate a reasonable approximation to a single instrument function profile. It is worth noting that in Figure 4.1 there is also a peak (~ pixel position 540) which was considered for use as an instrument function but from the observations mentioned below this would not have been suitable due to the difficulty in performing baseline subtraction and the presence of baseline continuum. Before presenting data on each of the three deconvolution techniques some observations about peakshapes and the importance of selecting the correct one are mentioned below. These observations are based on deconvolution of different experimental spectra, taken with the 2.2m system in Chapter 2, using different peakshapes and different deconvolution techniques.

- Peakshapes used in deconvolution need to be close to the spectral region of interest for the best resolution enhancement. Using instrument functions from spectral regions far away from the region of interest can to lead to false splitting and extra features where there are none. This can be attributed to the fact that the dispersion of a spectrometer varies with wavelength, hence the width of lines will vary across a spectrum (see Figure 2.13 Chapter 2).

- A lot of energy and information about an instrument function is contained in its wings. When a peakshape, isolated from a spectrum is used as an instrument function, you lose a lot of information about the peakshape itself because it is difficult to know where the wings are defined in the presence of baseline continuum and system noise Using peakshapes processed like this can produce artefacts and false peaks in deconvolved spectra in cases where the peakshape is no longer representative of the true instrument function.

- peakshapes isolated from spectra and fitted with Gauss-Lorentz lineshapes produce the best results from the point of view of resolution enhancement and absence of artefacts and false splitting of experimental lineshapes. It is known (and intuitively obvious) that a substantial degree of both the energy and information about an instrument function are contained in its wings. It is known that mixed Gauss-Lorentz or so called Voigt profiles can often provide best fits to the instrument function profile wings. Hence Voigt profiles are used here in those cases where the measured instrument function is curve fitted and the curve fit subsequently used for spectral restoration.

Deconvolution was performed on both single shot and multishot accumulated spectra. This was done in order to examine the sensitivity of each method to noise i.e. best and worst case scenarios. The difference between the experimental single and multishot spectra is shown below in Figure 4.3. As can be seen the averaging has no affect on the separation or position of the peaks, for reasons mentioned in Chapter 2 Section 2.4.3, but the averaging does result in a smoother or less noisy baseline. This is important particularly in cases where you are trying to resolve weak peaks which are in close proximity to strong peaks. For present purposes interest is confined to improved resolution in the case of strong peaks and resonances.

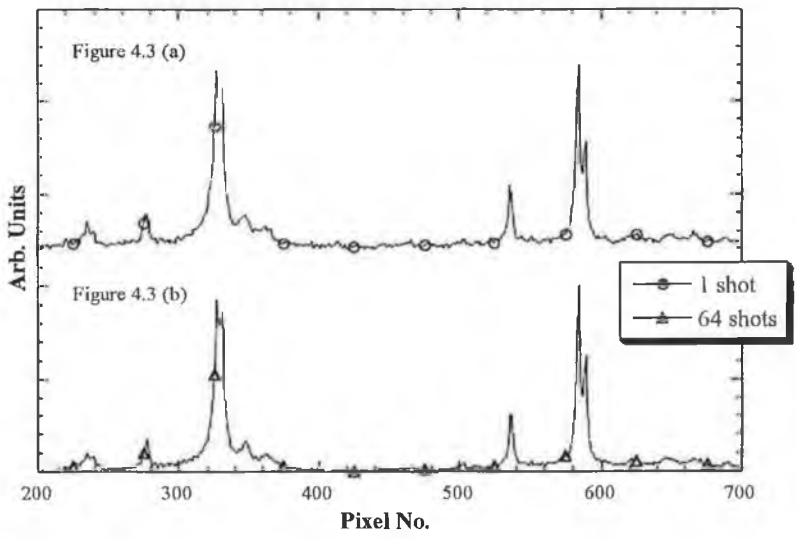

Figure 4.3 (a) Single shot AlO spectra, (b) Multishot (64) averaged AlO spectra

The AlO spectra (single and multishot) and peakshape used for each deconvolution technique were normalised as this is a requirement of the Constrained Non-Linear deconvolution method that the data be normalised between 0 and 1. So to maintain consistency this approach was used for each of the other deconvolution methods i.e. Fourier and Maximum Likelihood.

4.2 DECONVOLUTION OF EMISSION SPECTRA

4.2.1 FOURIER DECONVOLUTION

Before data are presented on the Fourier method, the following is a brief description of the parameters input to the technique. Fourier deconvolution reduces the halfwidths of

lines by a factor K [Kaupinnen *et al* 1981], which is in practice limited by the noise in the measured spectrum. K is the factor which decides what amount of spectral frequency information you smooth or cut-off in the Fourier domain. It is given by the expression

$$K = \frac{4\sigma L}{A} \tag{4.1}$$

where σ is the halfwidth at half max. of the instrument function, L is the value in Fourier space above which the spectral frequencies are cut-off and A is a constant determined by the apodisation functions used as part of the Finite Impulse Response Operator (FIRO) Fourier method described in Chapter 3. Three different apodisation functions were used [Kaupinnen *et al* 1981]:

$$\text{Triangular} = [\,1 - \frac{x}{L}] \qquad \text{and} \qquad \Delta\upsilon_{1/2} = \frac{1.772}{2L} \tag{4.2}$$

$$\text{Boxcar} = 1 \text{ for } |x| \leq 1, \; = 0 \text{ for } |x| > 1 \text{ and } \Delta\upsilon_{1/2} = \frac{1.207}{2L} \tag{4.3}$$

$$\text{Bessel} = [\,1 - \frac{|x|}{L}]^2 \text{ and } \Delta\upsilon_{1/2} = \frac{1.904}{2L} \tag{4.4}$$

where $\Delta\upsilon_{1/2}$ is the full width half maximum of the apodisation functions and where we get the values for A i.e. $\Delta\upsilon_{1/2}$ = A/2L. Once we understand the effect of K on the deconvolved spectra, we can choose an optimum value for it. We know σ so we can determine a value for L. This is how the Fourier software was written. The K, σ and A are input to the program and it generates a value for L as part of its deconvolution process.

With high K values there are significant differences in the SNR of the restored data as a result of the use of different smoothing or apodisation functions. The higher the value of K the greater the differences between the different smoothing functions. Usually apodisation defines the instrumental resolution. Hence the higher K, the more critical is the selection of the apodisation function.

Figure 4.4 (a) shows deconvolution of the spectrum in Fig 4.1 but with no filter used (no apodisation). Compared with the original spectrum there is a significant improvement in

the resolution of the strong peaks at pixel position ~ 340 and ~ 580. The downside to this simple approach is that by using no filter baseline noise has been amplified with the possible loss of information about weak features as they are now indistinguishable from the noise. The appearance of non-physical negative peaks is also of concern. Therefore we can say that for unfiltered single shot spectra, weak resonances are masked by the significant noise on the restored spectrum. For comparison purposes Figure 4.4 (b) shows a sixty four shot averaged spectra deconvolved the same way. There is no real change in resolution performance of the strong features in this case but there is a reduced level of baseline noise to the point where one can still distinguish the weak resonances (e.g. O V lines at pixel positions ~ 240 and 280).

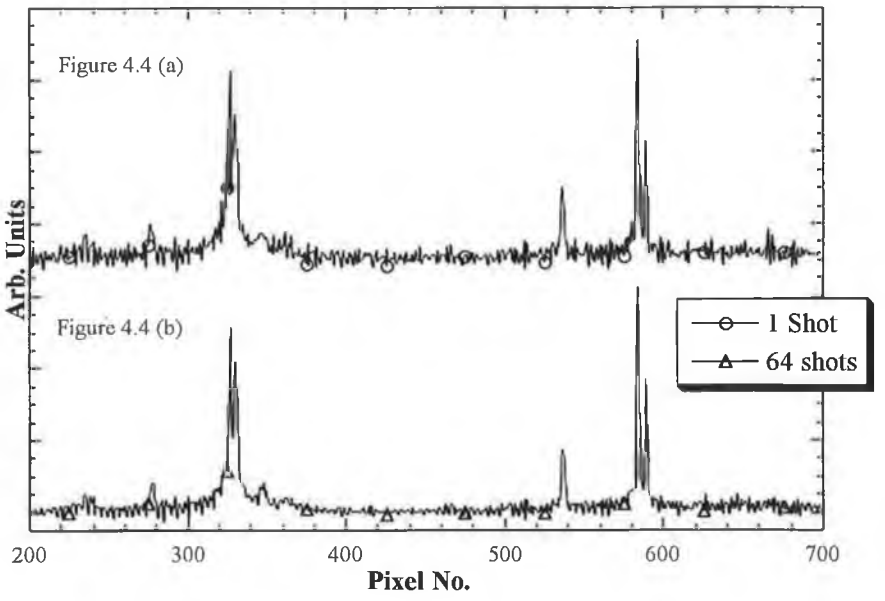

Figure 4.4 AlO Fourier deconvolved unfiltered spectra (a) Single shot and (b) Multi shot accumulated traces.

We next discuss the effect of filtering on the deconvolved spectra. The data in Figure 4.5 (a), (b) and (c) shows the same spectrum deconvolved but with three different types of filter or apodisation function applied with a K-value of 1.6 and σ value of 1.65 for each filter (Eqn's 4.2 - 4.4). With the filters we can still see an improvement in resolution of the strong peaks but less than that for the unfiltered spectra in Figure 4.4. On the positive side it is clear that the SNR of these data is significantly better than that of the unfiltered data. Therefore we can say that the filtering process improved restored image SNR but at a cost of reduced resolution. We also note from Figure 4.5 that

filtered deconvolution has improved SNR sufficiently to make clear weak features in the restored spectra.

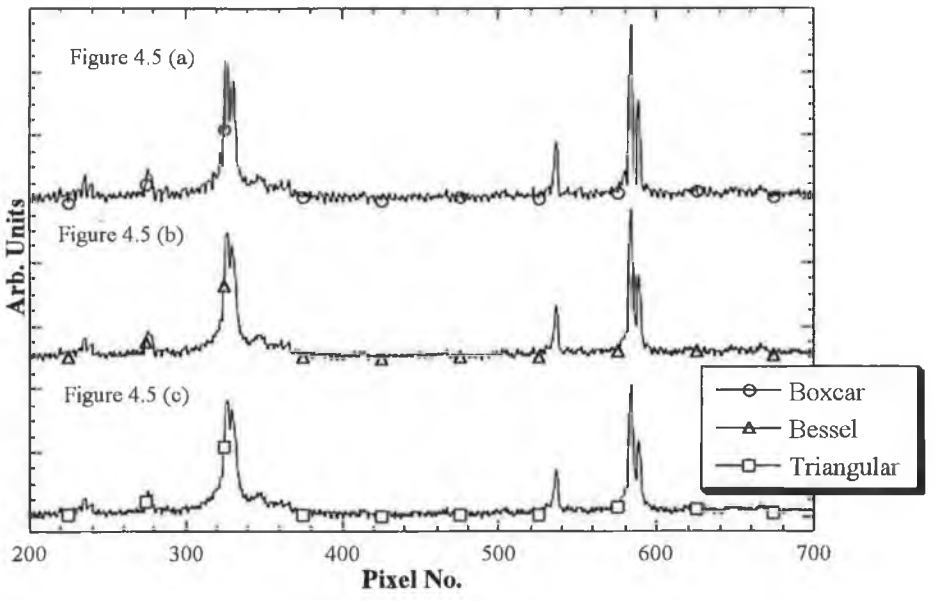

Figure 4.5 (a) Single shot AlO spectrum deconvolved with (a) Boxcar filter, (b) Bessel filter and (c) Triangular filter

The Bessel and Triangular data sets of Figure 4.5 show better noise and baseline performance and hence SNR. While the spectrum deconvolved using the Boxcar filter shows better resolution performance for the strong features but worse SNR. This is the trade-off that must be considered when using the filtered Fourier deconvolution or FIRO technique.

As the Boxcar filter gave the best resolution enhancement using the Fourier deconvolution method, for strong features, it was decided to examine the effect of varying the K parameter for this filter, which determines the amount by which the lines will be narrowed. The A and σ values are held constant at 1.207 and 1.65 respectively. Hence one is in effect varying L which in turn varies the frequency content of the restored spectrum. Figure 4.6 below shows the AlO spectrum for 3 different K values; 2.4, 1.3 and 0.5 respectively.

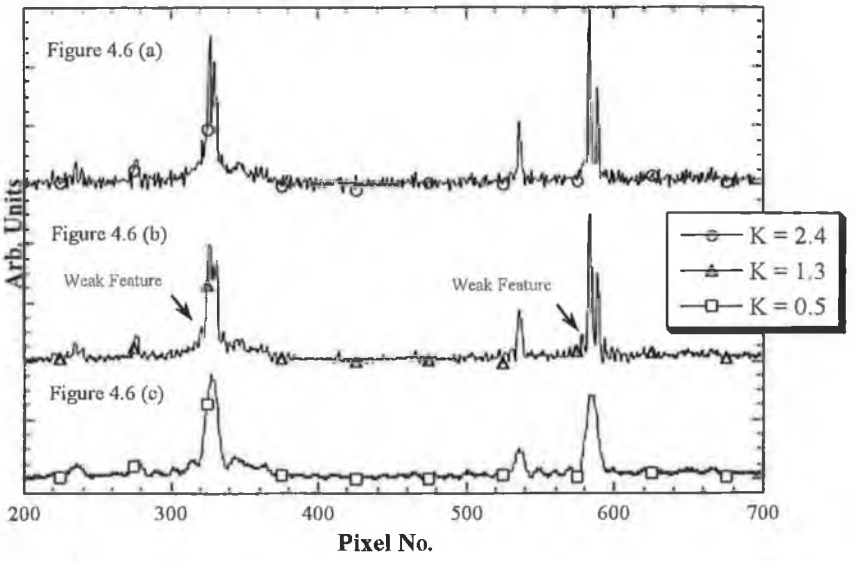

Figure 4.6 (a) Deconvolved AlO Spectrum with Boxcar filter and (a) K = 2.4, (b) K = 1.3 and (c) K = 0.5

These plots show that a reduction in the value of K results in a loss of resolution. This indicates that careful selection of K is critical to getting the optimum results from Fourier deconvolution. Its value will be based on the apodisation function used and the SNR of the measured data i.e., if the spectrum is noisy a smaller value of K (which results in smoothing of the restored spectrum and hence some loss of resolution) maybe a more suitable choice. Table 4-I below summarises the results of Fourier deconvolution for different K-Values and apodistion / filter functions.

Table 4 - I : Summary of Fourier deconvolution data for AlO experimental data for different K-Values and apodisation functions.

	Apodisation Function	Boxcar	Bessel	Triangular	Boxcar		
	K and HWHM Value ->	1.6 / 1.65	1.6 / 1.65	1.6 / 1.65	K = 2.4	K=1.3	K=0.5
Experimental Observation							
1. Level of Noise in restored data		High	Low	Low	High	Medium	Medium
2. Resolution Gain		Good	Poor	Poor	Good	Poor	None

The appearance of 'additional' weak features on the spectra in Figure 4.6 on either side of the stronger features may be an artefact of Fourier deconvolution as the instrument function is comparable with many of the features we are trying to deconvolve. For broad instrument functions, higher gain at higher spatial frequencies is required to restore a spectrum which can result in intense noise peaks at high spatial frequency which look like real peaks.

As we will see, for the Jansson Constrained Non-Linear technique these 'additional' false peaks do not appear. When the instrument function becomes too broad and the Fourier method fails, the Jansson technique succeeds by requiring that the intensity of the deconvolved bands be positive at all frequencies and the instrument function width be comparable with the measured lines.

The bottom line with Fourier deconvolution is that to get the best results you must play around with a number of different variables which include the value for K i.e., the selection of the apodisation function and a knowledge of the SNR in the data and also very importantly the instrument function used. The better one's knowledge of these variables, the more confidence one may have in the results obtained from this deconvolution method.

4.2.2 CONSTRAINED NON-LINEAR DECONVOLUTION

The following data illustrates the application of the Jansson - Van Cittert Non-Linear deconvolution technique. As a reminder, the basic algorithm used is given by the expression

$$O_n = O_{n-1} + \alpha_n \{I - O_{n-1} \otimes M\} \qquad (4.5)$$

where the symbols used here have been previously defined in Chapter 3. The data presented here makes use of the relaxation function α_n of Blass and Hasley [1981] which is given by the expression

$$\alpha_n = \alpha_{n\,max} \{O_{n-1}(x)[1 - O_{n-1}(x)]\}^p \qquad (4.6)$$

The success of this technique is dependent on the form of this relaxation function. It is this parameter that actually makes the technique decidedly non-linear. The data set used

to deconvolve is the same as that used for Fourier deconvolution, i.e. AlO spectrum. Figure 4.7 (a) and (b) show the results of the application of this technique to a single shot and multi-shot accumulated spectra (64 shots) using the following parameters; number of iterations = 50, p = 4 and $\alpha_{n\,max} = 5$.

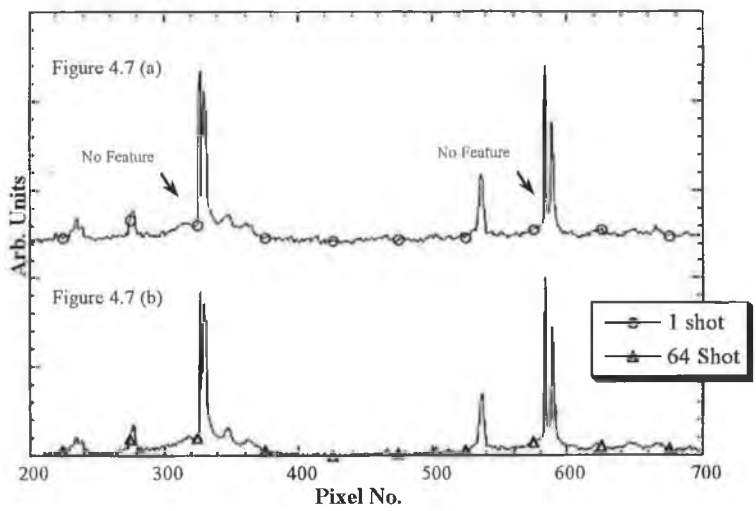

Figure 4.7 (a) Restored AlO single shot spectrum, (b) Restored AlO Multishot spectrum. With the following parameters used for (a) and (b) number of iterations = 50, p = 4 and $\alpha_n = 5$.

From these data we see that for both spectra there is very good restoration on the strong resonances and better SNR performance than the Fourier method. We also note that for the multishot spectrum the noise is less as would be expected from observations made in chapter 2. The resonances around the 340 pixel region appear as a doublet, with one of the components broader than the other. From identification of the lines in this region of the spectrum, it is known that there are three O V lines present here 192.906 Å, 192.751 Å and 192.799 Å. The separation of these later two features is ~ 0.05 Å (of the order of one pixel width). We can see that this method has not resolved these two features because their separation lies below the Nyquist limit. However this technique does tell us that there are possibly two features here.

Both spectra in the above case do not appear to have "wall" side features that the Fourier method gave. The Jansson method is saying that there are no other features in this region.

Figure 4.8 shows the sensitivity of this technique to the relaxation parameter $\alpha_{n\,max}$. In this case the number of iterations and the exponent p in equation 4.6 have been kept

constant at number of iterations = 20 and p = 4, where the $\alpha_{n\ max}$ parameter has been varied to see what the effect on the restored AlO spectra would be in terms of resolution and noise.

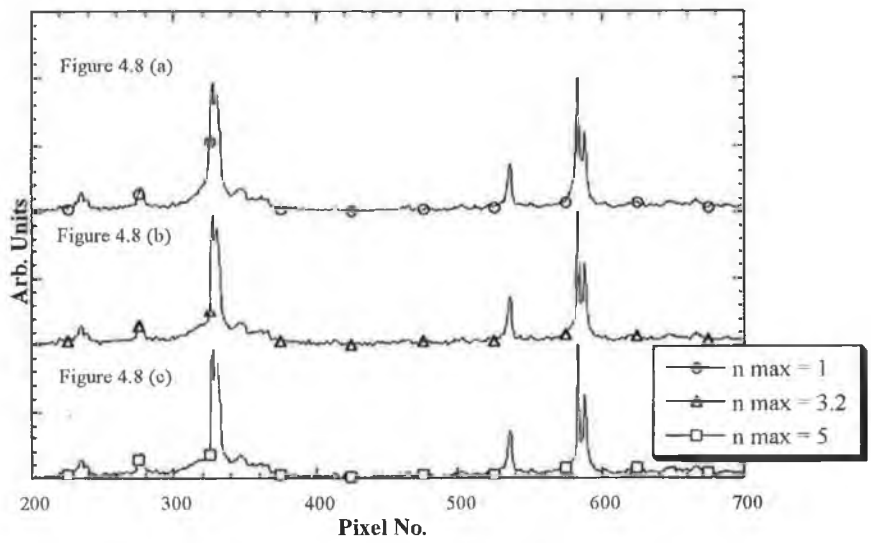

Figure 4.8 AlO single shot spectrum with iterations = 20 and p = 4 and (a) α_{nmax} = 1.0, (b) α_{nmax} = 3.2 and (c) α_{nmax} = 5.

Figure 4.8 (a) is practically the same as the original unrestored spectrum, with no resolution gain seen. Figure 4.8 (b) shows a further slight resolution gain. In Figure 4.8 (c) we still only see a slight improvement is resolution, even though the factor $\alpha_{n\ max}$ is now 5 times greater compared to Figure 4.8 (a). For each change in the value of $\alpha_{n\ max}$ there are only slight, if any changes, in the resolution improvement of the spectra. It is obvious that for further resolution improvement we must continue to iterate. If we compare Figure 4.7 (a) and 4.8 (c), the only difference between them being the number of iterations, the former having been processed for 50 iterations and Figure 4.8 (c) iterated 20 times. By comparing these two figures it can be concluded that continued iterations result in improved resolution for $\alpha_{n\ max} = 5$.

To conclude we can say that the technique appears to be good for restoring single shot spectra without the appearance of "false" peaks and it does not cause the noise in the spectra to increase. Indeed it maintains and often improves the SNR. The key parameters to get right are again the instrument function, value for $\alpha_{n\ max}$ and the number of iterations. Of all the problems that can be encountered in attempting deconvolution using this technique, the most serious is the failure to converge. The main reason for

this happening would be the presence of noise. If the SNR is poor for this technique then it will diverge and give unphysical results. Caution must be taken not to use too many iterations and over deconvolute thereby causing the appearance of "false" peaks. This technique is similar to the Fourier method in that you must vary different parameters a number of times before you get the optimum result.

4.2.3 MAXIMUM LIKELIHOOD DECONVOLUTION.

In this particular case, it was decided to use a commercial package called "SSRES" which was part of spectrocopic data analysis package called SPECTRACALC™. The commercial code was developed using the theory discussed in Chapter 3 for this method. This technique requires as input the instrument function and an estimate of the SNR of the measured spectral data. The software actually estimates the SNR for the user and hence one can either use this estimate or input an arbitrary value.

When this method is applied to the AlO spectrum of Figure 4.3 (a) for two different SNR ratios we get the data sets shown in Figure 4.9 (a) ("SSRES" estimates 2% noise in data) and Figure 4.9 (b) (user estimate of 10 % noise in data). Figure 4.10 (a) and (b) are multishot spectra.

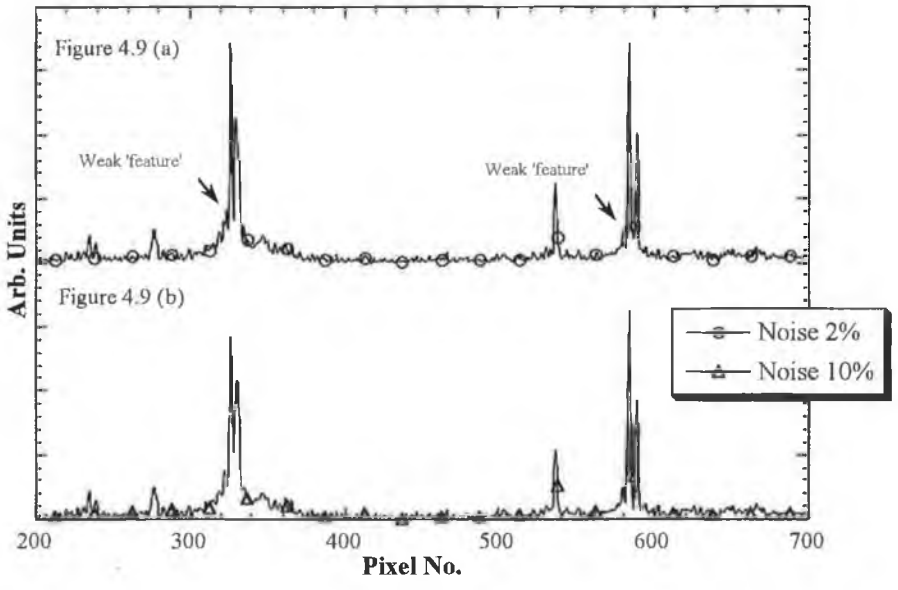

Figure 4.9 AlO single spectrum with noise equal to (a) 2 % and (b) 10 %

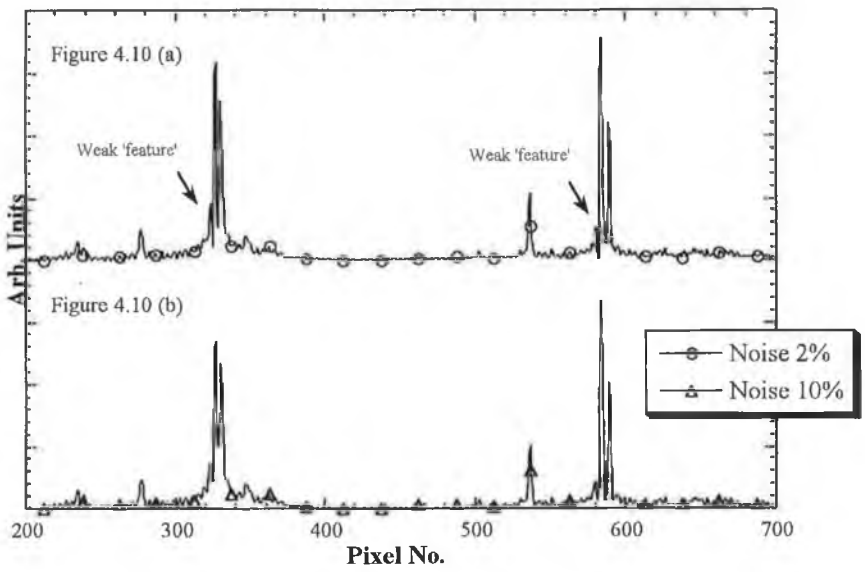

Figure 4.10 AlO multishot spectrum with noise equal to (a) 2 % and (b) 10 %

We see that there is a definite improvement in the resolution, but we see the appearance of side wall features as in the Fourier method. An estimate of 10 % noise was input in order to force the Maximum Likelihood software to restore noise as real spectral features. This method permits a test of the sensitivity of Maximum Likelihood to data noise. As in the case for the Fourier method, Maximum Likelihood 'restored' weak features on the low energy side of the strong doublet features. Hence the physical reality of these features remains uncertain. The data in Figures 4.9 and 4.10 shows that the Maximum Likelihood method recognises that there are two components in the doublet centred around pixel position 340. This is the same as the result for Fourier and Constrained Non-Linear methods.

4.2.4 COMPARISONS AND CONCLUSIONS

Fourier deconvolution has a tendency to amplify measured data noise and hence Jansson and Maximum Likelihood generate restored spectra with by far the best SNR and resolution. Overall the Jansson and Maximum Likelihood methods give similar performance in terms of resolution enhancement and do not enhance or amplify the noise. Fourier does provide resolution enhancement but at the expense of degrading the SNR. From a point of view of ease of use and minimal number of variables Maximum Likelihood is the better technique. Both Fourier and the Constrained Non-Linear

method have multiple variables which can have multiple values depending on the user so in this sense these techniques are difficult to use and require a lot of experience in choosing the appropriate variable values (different users will get different results for the same spectral data). The following table below summarises the performance of each method in terms of noise and resolution gain.

Table 4-II : Table comparing the different deconvolution techniques for the doublet features at pixel positions 340 and 580 in Figure 4.1.

	Fourier	Constrained Non-Linear	Maximum Likelihood
Experimental Observation			
1. Level of Noise in restored data	High	Low	Low
2. Resolution Gain	Medium	Good	Good
3. No. of Input parameters	Multiple	Multiple	2
4. Level of spurious features after restoration	High	Low	Medium

4.3 DECONVOLUTION OF PHOTOABSORPTION SPECTRA

4.3.1 INTRODUCTION

The well known extreme-UV (XUV) absorption spectrum of helium was used to test both the photoabsorption capability of the system and the potential use of deconvolution methods to determine restored resonance profiles.

The Maximum Likelihood method was chosen as the deconvolution technique to examine photoabsorption spectra and deconvolution because it accounted for the SNR of the data and had comparable resolution to the Jansson method and didn't require any arbitrary filter or window functions as used in FIRO and Non-Linear methods. Hence one can conclude that the objectives of the Maximum Likelihood (best estimate) makes it the optimum candidate for the present exercise.

The usefulness of the deconvolution process , as applied to photoabsorption spectra, could be measured in terms of the determination of resonance parameters of features present in the spectrum of Helium. We know that the photoabsorption cross section for a certain element represents a measure of the probability that a photon will be absorbed as a function of the photon energy. For helium these cross sections are larger at certain energies which result in resonances which have a characteristic shape known as a Fano-Beutler profile (see Fano [1961]).

Normally in photoionisation / absorption experiments one would expect the photoionisation cross section to decrease monotonically as one moves toward higher photon energy away from the ionisation threshold. In the case of helium, asymmetric resonances in the photoabsorption cross section were observed by Madden and Codling [1965] some 30 years ago. The origin of these resonances as atomic interference phenomena had been discussed in some detail some years previously by Fano [1961]. Briefly for an incident photon energy of ~ 60.15 eV two outcomes are possible :

- direct single ionisation resulting in a He^+ ion and a free electron.
- one photon two electron excitation $1s^2 \rightarrow 2s\ 2p$

The doubly excited ($1s^2 \rightarrow 2s\ 2p$) state is clearly unstable and undergoes a process by which one of the electrons is "shaken off" - so called autoionisation.

Clearly we have a situation in which the final state i.e. He^+ and a free electron maybe reached by two competing pathways, each with its own probability amplitude which are themselves photon energy dependent and hence the net result is an atomic interference phenomenon i.e. asymmetric Fano shape.

4.3.2 DECONVOLUTION OF HELIUM PHOTOABSORPTION SPECTRA

Figure 4.11 shows an experimental helium photoabsorption spectrum obtained with the spectrometer described in chapter 2. The helium pressure was 0.28mbar and no foil was used. You can see clearly from this spectrum the $1s^2 \rightarrow 2s\ np$ (n = 2 to 6) series. To demonstrate the effect of deconvolution on this type of spectrum, the first member was concentrated on.

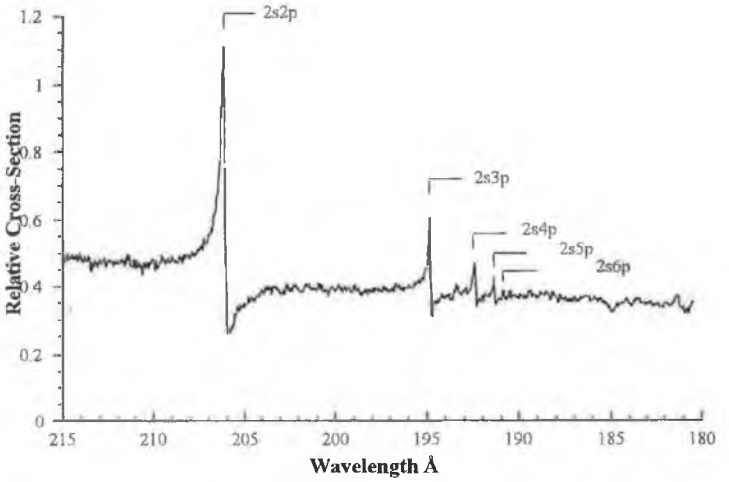

Figure 4.11 Photoabsorption spectra of He in the photon energy regions corresponding to direct photoionisation and double electron excitation (He pressure = 0.28 mbar).

From work done by Fano [1961] and as measured at high resolution by others e.g. Domke *et al* [1991], there is a minimum in the cross-section at ~ 60.2 eV. The minimum is not observed in experimental measurements due to 1. the inherent resolution limit of the multichannel spectrometer and 2. the effect of additional light on the "incident" I_0 and "transmitted" I intensities as discussed previously in chapter 3. In order to fit the measured resonance we employ a modified Fano formulism given by

$$\sigma = \sigma_b + \sigma_a \left(\frac{(q+\varepsilon)^2}{1+\varepsilon^2} \right) \tag{4.8}$$

where the parameter ε is given by

$$\varepsilon = \frac{E - E_0}{\tau/2} \tag{4.9}$$

and where τ is the FWHM of the resonance, E_0 is the resonance energy position and q is the profile index or asymmetry parameter which is a measure of the strength of the coupling of the 'discrete' two electron state to the continuum. The results of this fit to the first resonance is shown in Figure 4.12. The values for the resonance obtained were E_0 = 60.155 eV, τ = 0.077 eV and q = -1.77. When compared with the currently accepted

values of E_0 = 60.15 eV, τ = 0.038 eV and q = -2.6 (Morgan and Ederer [1984]), it is clear that the results for q and τ are significantly in error.

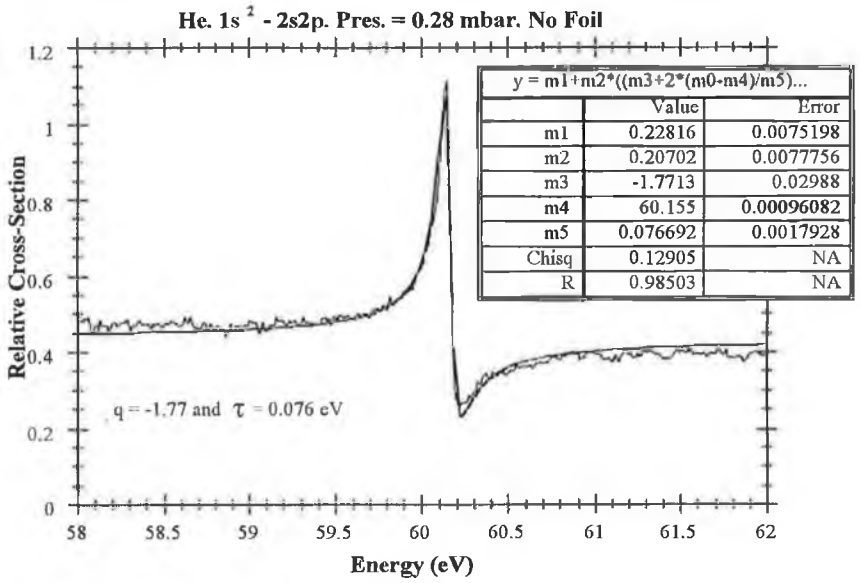

Figure 4.12 He photoabsorption spectrum with a Fano fit to the first member of the series $1s^2 \rightarrow 2s2p$.

In order to improve these values, the Maximum likelihood deconvolution technique was applied to the data using an instrument function which was obtained from an Al emission spectrum close to the energy region for the He resonance. A line was selected from the data shown in Figure 4.13 at pixel position 809 and a wavelength of 168 Å.

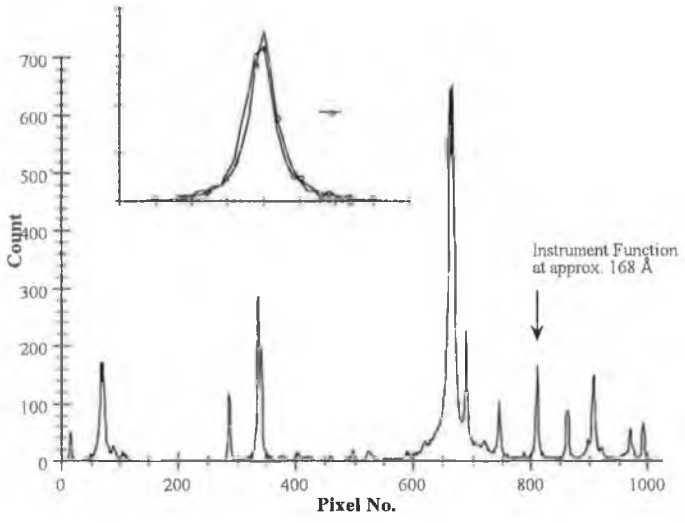

Figure 4.13 Al emission spectrum showing where the instrument function was obtained (inset - Lorentzian fit to experimental line).

The line in fact is not a single isolated line but consists of a blend of four lines at wavelengths of 167.98 Å, 168.007 Å, 168.046 Å and 168.076 Å. However the bulk of the intensity lies with the first two lines which are separated by 0.02 Å which is well less than one pixel width (0.03 Å) and is a reasonable approximation to a single isolated line. In order to obtain an instrument function we fitted this line with a Lorenztian (after baseline subtraction) which provided the best approximation to the measured line profile. This instrument function was used for subsequent deconvolution of helium data sets. Its FWHM was 3.6 pixels. Applying the Maximum Likelihood deconvolution process to the helium data in Figure 4.12 yielded the resonance shown in Figure 4.14.

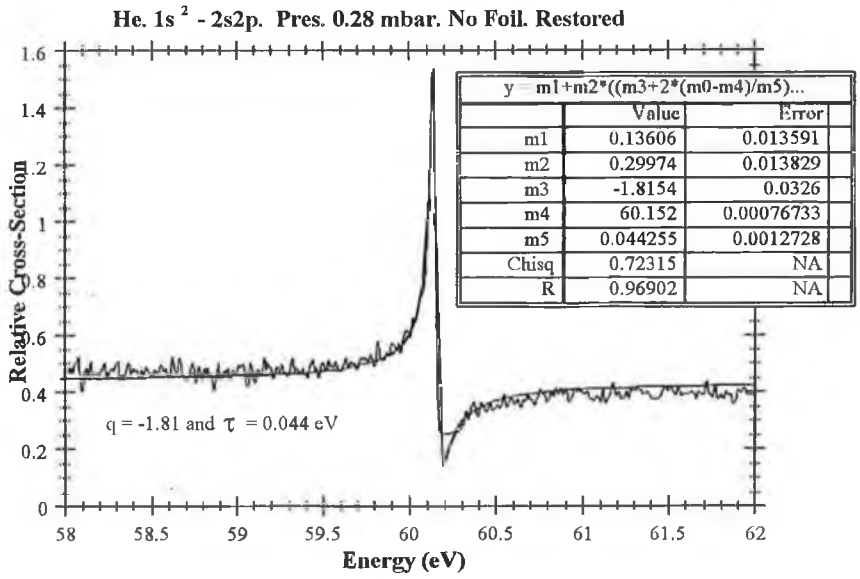

Figure 4.14 Helium spectrum with deconvolution and with Fano fit applied.

A slight improvement in the q-value to -1.81 and a significant improvement in the width τ resulted (0.077 eV to 0.044 eV). However it is clear that the restored profile is far from the true profile.

In a second experiment, the same measurements were made at a similar pressure of 0.25 mbar (shown in Figure 4.15 (a)) but this time in the presence of a 200 nm aluminium foil in order to reduce the effects of additional light on the incident and transmitted XUV intensities. A FANO fit to the experimental data before deconvolution yielded q and τ values of -1.93 and 0.076 eV respectively. Although the τ value is similar to that in the case of no foil, the q value is better, which is most likely the result of the reduction of additional light. Using exactly the same instrument function the spectrum is

deconvolved (Figure 4.15 (b)) and the resultant Fano fit yielded q and τ values of -1.99 and 0.046 eV respectively.

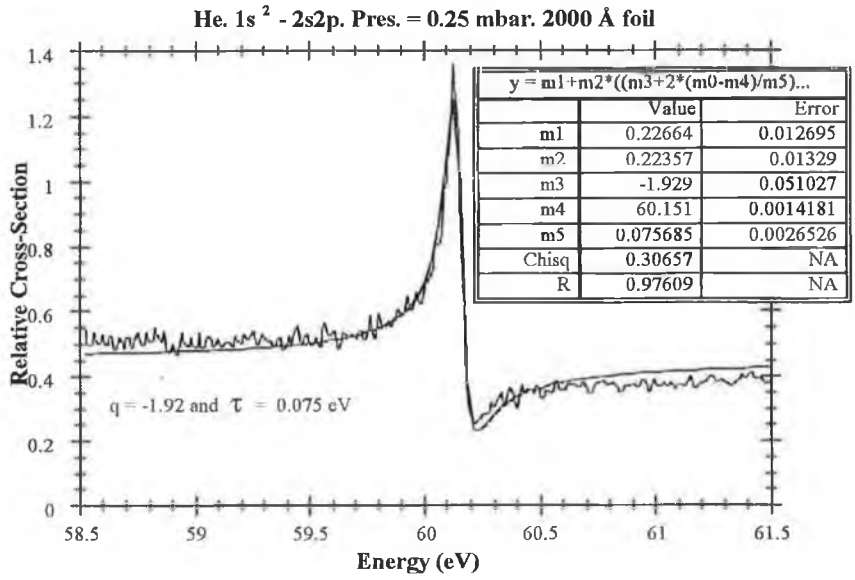

4.15 (a)

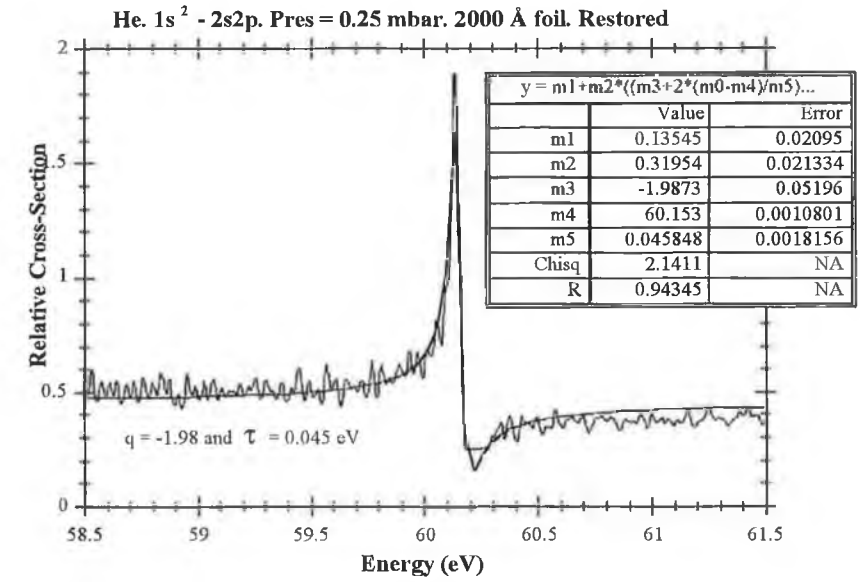

4.15 (b)

Figure 4.15 Helium 0.25 mbar with 2nm foil photoabsorption data (a) experimental with fit and (b) deconvolved with fit.

In the final experiment the helium pressure was reduced to 0.16 mbar (Figure 4.16 (a)). In this case a Fano fit to the raw spectral data yielded a slightly improved q value and slightly narrower width of 0.067 eV. Application of the Maximum Likelihood

deconvolution procedure and further Fano fit to this data yielded improved q and τ values of -2.1 and 0.035 eV respectively (Figure 4.16 (b)).

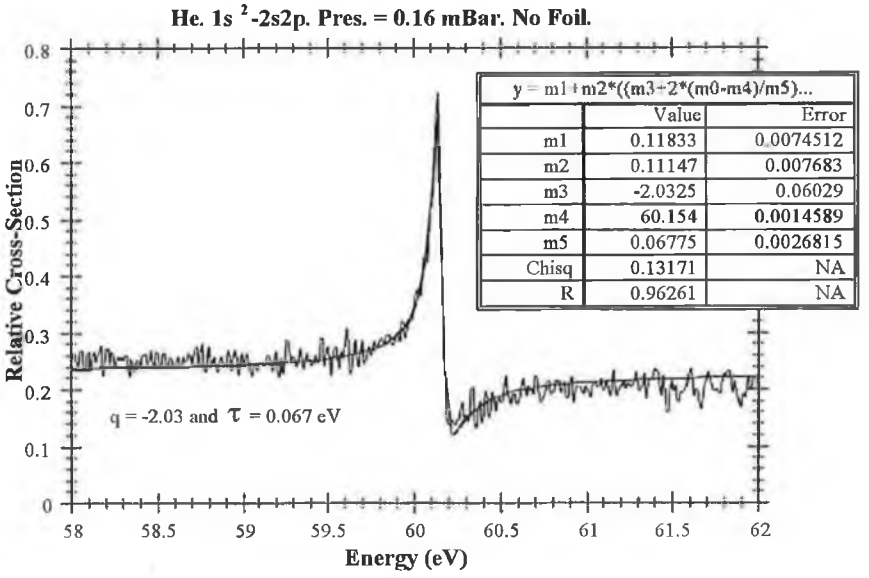

4.16 (a)

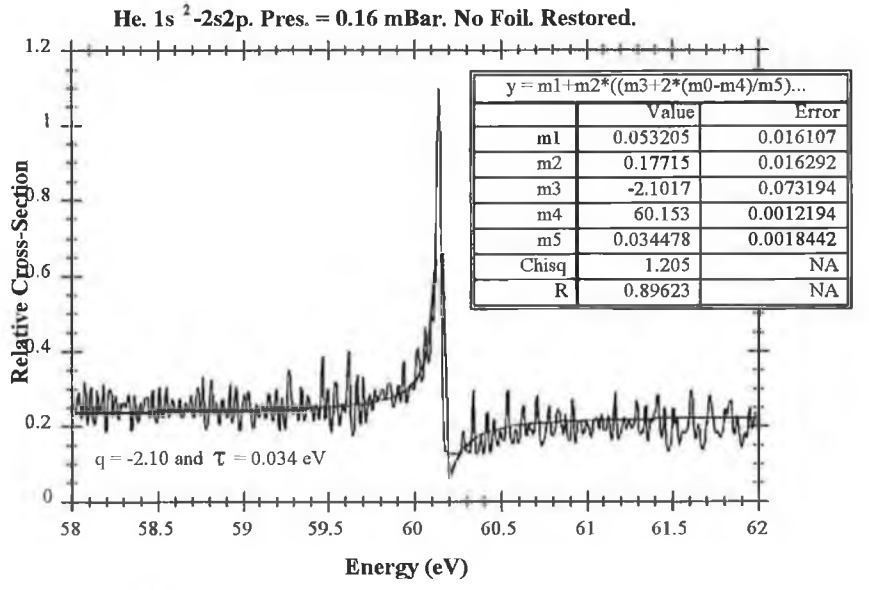

4.16 (b)

Figure 4.16 Helium 0.16 mbar photoabsorption data (a) experimental with fit and (b) deconvolved with fit.

Finally a theoretical Fano profile was constructed from the known Fano parameter and folded with a Lorentzian instrument function of FWHM 3.5 pixels. The resultant Fano fit yielded q and τ values of -2.6 and 0.068 eV respectively (Figure 4.17), which shows

the width τ is largely determined by the instrument resolution. In this particular case at least q is insensitive to the instrument resolution and other additional factors (e.g. additive light on I and I_0) which can be mentioned in order to explain discrepancies in the measured values of q and τ.

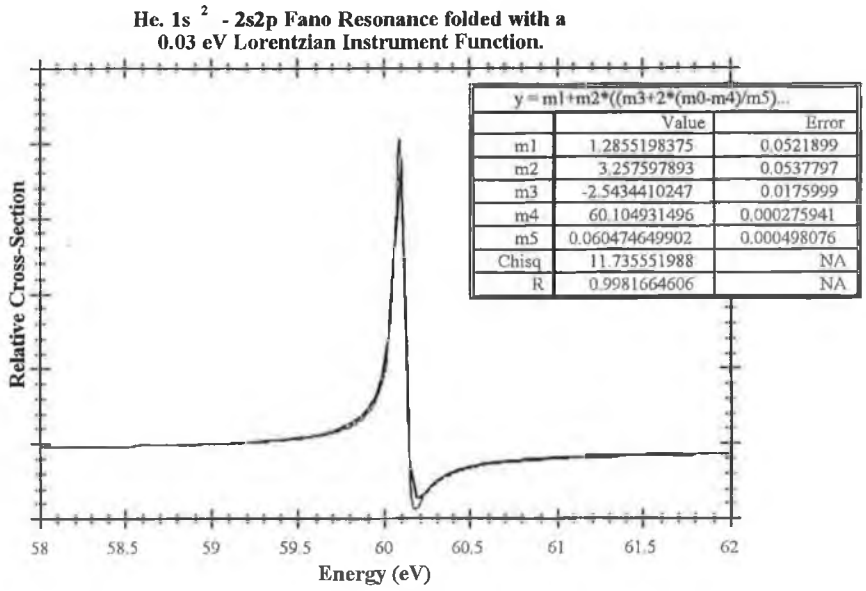

Figure 4.17 Theoretical Fano resonance folded with a Lorentzian peakshape of FWHM 3.5 pixels.

Table 4-III below summarises the q and τ values obtained for each of the Helium experiments above.

Table 4-III : q and τ values obtained using the Maximum Likelihood Deconvolution technique for the $1s^2 \rightarrow 2s2p$ resonance of Helium

Pressure (mbar)	Foil Thickness	q Exp	q Decon	τ Exp (eV)	τ Decon (eV)
0.16	n/a	-2.03	-2.1	0.067	0.034
0.25	2000 Å	-1.92	-1.98	0.075	0.045
0.28	n/a	-1.77	-1.81	0.076	0.044

REFERENCES

Blass, W.E. and Hasley, G.W., "Deconvolution of Absorption Spectra", Academic Press (1981).

Domke, M., Xue, C., Pushmann, A., Mandel, T., Hudson, E., Shirley, D.A., Kaindl, G., Greene, C.H., Sadeghpour, H.R. and Petersen, H., Phys. Rev. Lett. **66** 1306 (1991).

Fano, U., Phys. Rev. **124** 1866 (1961).

Kauppinen, J.K, Moffatt, D.J., Cameron, D.G. Mantsch, H.H., Appl. Opt. **20** 1866 (1981)

Kelly R.L., "Atomic and ionic lines below 2000 angstroms : Hydrogen through Krypton", Part I (H-Cr), Part II (Mn-Kr) and Part III (Finding List), J. Physical & Chem. Ref. Data, Vol **16,** supplement No.1, (1987).

Madden, R.P. and Codling, K., Astrophys. J. **141**, 364 (1965).

Morgan H.D. and Ederer D.L., Phys. Rev. A., **29**, 1901, (1984).

Chapter 5

Conclusions and Future Work

CHAPTER 5 : CONCLUSIONS AND FUTURE WORK

5.1 SUMMARY

A multichannel extreme-UV (XUV) spectrometer system for emission and absorption spectroscopy with laser produced plasmas has been described. The instrument is based on a 2.2m grazing incidence Rowland mount to which an XUV multichannel detector consisting of a Galileo Channel Electron Multiplier Array (CEMA) with photodiode readout has been fitted. The performance of the instrument is illustrated by presenting typical emission spectra of Al/ AlO plasmas (line radiation dominated), tungsten plasmas (continuum radiation dominated) and photoabsorption spectra of both helium gas and thin film aluminium. Briefly, the characteristics of the system are;

- Single laser shot sensitivity
- Wide photon energy range (20 - 250 eV)
- High resolution (R = 1000 -> 2000 for a 1200 grooves.mm grating)
- Real time spectral recording
- Measurement of photoabsorption cross-sections
- Flexible and easy to use control and data acquisition software

It is found that although spectral resolution is a key consideration in the measurement of photoabsorption line profiles the effects of additional light (scattered and/or high spectral order radiation) can result in erroneous values for both line profile parameters and even non resonant cross-sections. Calculations with simple modified transmission formulae illustrate this point clearly in chapter 2. Hence great care is needed in the determination of relative and absolute cross sections in future experiments. This point is returned to in the section 5.2 below.

A second major aim of the project concerned an investigation of the application of three key deconvolution techniques using (i) Linear Filtered Fourier, (ii) Contained Non-Linear Jansson-Van Cittert and (iii) Maximum Likelihood algorithms to resolution enhancement of spectra recorded with the XUV multichannel spectrometer. Preliminary results show that both the Constrained Non-Linear and Maximum Likelihood methods generate restored spectra with the best signal to noise ratio (SNR) when compared to linear Fourier methods. Although the filtered Fourier technique may be forced, by suitable choice of spatial frequency filter, to yield data of SNR comparable to the non-linear and probabilistic methods, it does so at a cost of poor spatial resolution gain. The

Maximum Likelihood technique has the attraction of being the most objective method as it does not employ arbitrary frequency filters or weighting factors as in the case of the linear and non-linear techniques. By far the most important parameter, no matter the method chosen, turns out to be the instrument function a point taken up in section 5.2 below.

5.2 FUTURE WORK

It is clear that for photoabsorption studies 'additional' light on both the incident and transmitted spectra has the effect of modifying both line profiles and cross-sections (even non resonant values). Hence for future experiments it will be necessary to determine both the level of such light on the I and Io traces and also to take steps to eliminate (or at least reduce) such unwanted signals. Clearly the use of narrow band thin metallic filters should be considered in such applications to eliminate additional light in all but the spectral region of interest. Comprehensive data are available for most metals and some polymers from the UV to the X-ray spectral range for design purposes (e.g. Powell et al , Chapter 2.). One further advantage of the use of bandpass filters matched to the spectral region of interest is that any higher order radiation contributions to additional light are eliminated and any residual effects can be ascribed to e.g., scattered light only.

The results on the deconvolution studies to date show that this line of investigation is worth further study. In particular a comprehensive study of the effect of instrument function shape and a measurement of the multichannel spectrometer's real instrument function are most important goals. An XUV source emitting a spectrum with bright lines of width well below the instrument limits of ~ 3.3 pixels and covering the 20 - 250 eV photon energy range would be needed for the measurement of the instrument's impulse response. One possibility might be a windowless hollow cathode lamp. However, it may be necessary to run such a source at a high pressure / density in order to generate bright XUV lines which then defeats the original purpose of obtaining narrow lines.

As yet the shape of the XUV beam as accepted by the spectrometer optics has not been determined. A combination of ray tracing and measurement of the beam shape using a knife edge intercepting the XUV beam in two orthogonal directions would provide such a measure of the spatial resolution of the instrument at any position between the plasma source and toroidal mirror.

One final enhancement to the system would be the addition of a gated detector providing gate widths from nanoseconds upwards. This would allow a closer examination of the time resolved properties of expanding laser produced plasmas via time resolved emission spectroscopy. Plasma parameters, such as electron and ion densities / temperatures, could be measured using a gated detector on the 2.2 m spectrometer described in this thesis. For photoabsorption studies the duration of the continuum pulse could be selected by utilising the timing features of the detector/optical shutter in this mode. This would be useful as it would ensure fixed time resolution for absorption in a particular spectral region. Because the duration of the continuum pulses emitted from laser produced plasmas varies across the XUV region, by gating the detector you could select a time window of say ~ 10 ns and the continuum would be uniform in this window.

APPENDICES

Appendix I

GPIB SOFTWARE SETTINGS

GPIB.COM/IBCONF.EXE configuration file settings for both the GPIB board and Model 1461 Detector Interface

1. Board : GPIB0

· Primary GPIB Address.	0
· Secondary GPIB Address.	None
· Time-out Setting.	T10s
· EOS byte.	00H
· Terminate Read on EOS.	No
· Set EOI with EOS on Write.	No
· Type of compare on EOS.	7-bit
· Set EOI w/last byte of write.	Yes
· GPIB-PC Model.	PC2
· Board is System Controller.	Yes
· Local Lockout on all devices.	Yes
· Disable Auto Serial Polling.	Yes
· Disable Device Unaddressing.	No
· High Speed Timing.	Yes
· Interrupt Jumper Setting.	7
· Base I/O Address.	2B8H
· DMA Channel.	1
· Internal Clock Frequency.	8

2. Device : M1461 BOARD : GPIB0

· Primary GPIB Address.	12
· Secondary GPIB Address.	None
· Time-out Setting.	T10s
· EOS byte.	00H
· Terminate Read on EOS.	No
· Set EOI with EOS on Write.	No

· Type of compare on EOS. 7-bit

· Set EOI w/last byte of write. Yes

NOTE: For the meaning of the individual entries press F2 to explain each field when you are actually running the IBCONF program and also look-up information provided in the GPIB manual.

Appendix II

GPIB FILES AND DIRECTORY STRUCTURE

There are a number of files needed to control the OMA. These files must be placed in the correct directories and also there are commands which must be placed in both the AUTOEXEC.BAT and CONFIG.SYS files in order for the software to run properly.

The basic set of files needed to run the OMA software are as follows :

1. OMAPROG.EXE
2. OMA.BAT
3. 1.BAT
4. 2.BAT
5. 3.BAT
6. GPIB.COM
7. IBCONF.EXE

FILE DESCRIPTIONS :

1. OMAPROG.EXE

This is the main control program which was developed using Turbo C. It is an executable file which can be run by typing OMAPROG at the DOS prompt. It contains the code required to control the OMA interface and change settings e.g. number of scans, number of ignore scans, exposure time, etc. The package is user friendly with instructions being presented in window format. Details are also entered through windows displayed on the screen and responses typed in on the keyboard.

2. OMA.BAT, 1.BAT, 2.BAT, 3.BAT

These are simple DOS batch files which allow the user to interchange between the OMA control program, SPECTRACALC plotting program and DOS.

3. GPIB.COM

This is a GPIB-PC software file. It is a device handler file that is loaded at system start-up by the DOS operating system.

4. IBCONF.EXE

This is a software configuration program that allows you to change the software parameters and other data used by the handler file GPIB.COM

NOTE: for more detailed information about installing the GPIB software and hardware refer to the GPIB manual and Chapter 3 of M Shaw's thesis.

INSTALLING AND USING THE OMA CONTROL SOFTWARE

The diagram below indicates where the above files should be placed in order to use the OMA software to control and acquire data from the detector on the 2.2 m grazing incidence spectrometer.

Diagram showing where the files required to run the OMA software should be installed

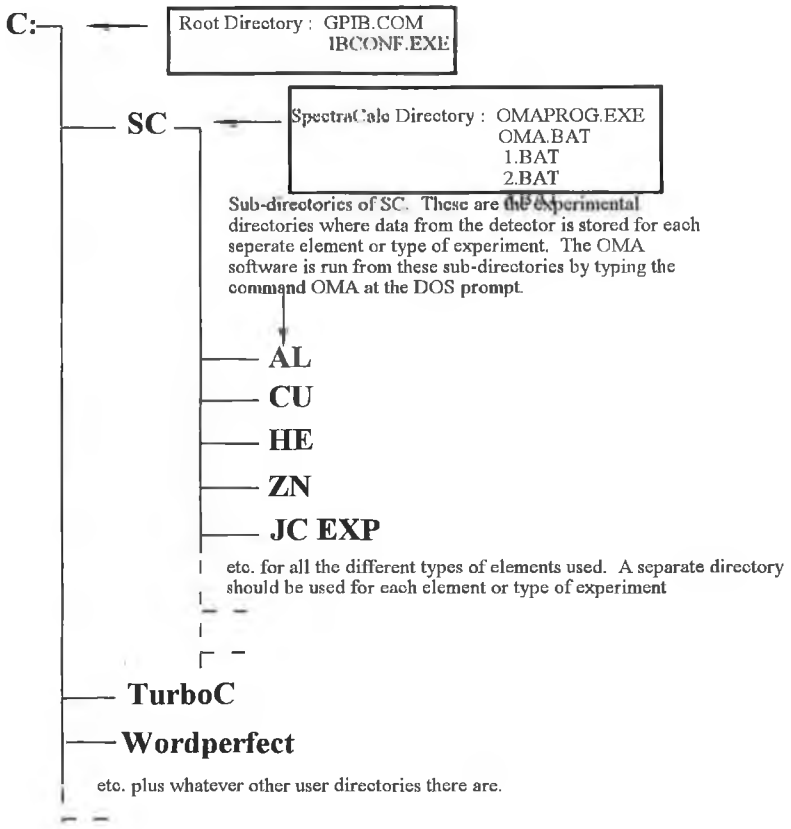

The files OMAPROG.EXE, OMA.BAT, 1.BAT, 2.BAT AND 3.BAT should be installed in the spectracalc (SC) directory where the spectracalc program itself is installed.
The files GPIB.COM and IBCONF.EXE are files which come along with the GPIB-PC hardware and software package. The GPIB software is installed using the installation program provided with the package. In order to communicate with the OMA the file GPIB.COM must be loaded at start-up. This is done by placing the command :

DEVICE=GPIB.COM

in the CONFIG.SYS file, which is also in the root directory. The program IBCONF.EXE is used to configure the card and whatever devices are attached to it (i.e. the OMA interface). To use this program type IBCONF from the root directory and set the required parameters for both the card and the device (OMA). At the moment the parameters for the GPIB interface card and OMA interface are set on the computer (TANDON 286) used to control the 2.2 m instrument. In order to check these settings or change them if you are going to use another computer, just type IBCONF from the root (C:\) directory and check the GPIB0 and M1461 devices on the device map. Once these settings have been made and you can communicate with the OMA there is no need to change any of the settings in the GPIB.COM file. Every time you use the OMA software these settings will automatically be used so that you only need to run the OMA program from the directory you will save your data to. The only time you will change any settings is when you attach another device to the card or when you re-install the card in another computer

In order to run the OMA software from any directory you must also place the command :

PATH = C:\SC

in the AUTOEXEC.BAT file. This will ensure that when you type the command OMA from any of the experimental/user directories.

USING THE SOFTWARE

If the above files have been installed/copied into the correct directories then you are ready to use the software. Create or goto a sub-directory off the SC directory e.g. **HE**

and type OMA and you will see three different options. Before you choose the OMA option make sure of the following:

1. The proper connections are made between the OMA and computer via the interface
   cable.
2. The OMA interface is switched on.
3. The water cooling and nitrogen gas are supplied to the detector.

Once you have checked all this you can choose the OMA option. When you enter the program you will see a screen with a list of menu items across the top. The first thing you should do is to goto the TERMINAL ID. option and choose it. If you see a message with the number 1461 flashing then proper communication between the computer and OMA interface has been established (NOTE : you should also see the remote indicator on the OMA light up as well). The software is then ready to use and you can proceed with your experiment using the other features provided with the software (See Chapter 3 of M Shaw's thesis).

ORIGINAL PROGRAMS USED IN THE DEVELOPMENT OF THE OMA SOFTWARE.

1. Turbo C project file OMAPROG.PRJ. This file contained the following programs :

TCIBS.OBJ
VID.OBJ
VIDEO.C
KEY.C
SCRSTK.C
MENU.C
LX800.C
INPUT.C
OMAPROG.C

These are the programs which were used in the development of the OMA control program. In order to add or change the OMA program you must open the file OMAPROG.PRJ and then edit the files to make the required changes. After editing you use the project make facility with Turbo C to create a new OMAPROG.EXE file which

must then be copied to the C:\SC directory. A description of the function of each program is given in Chapter 3 of thesis.

The following are a number of files which must also be included in the program development as well:

VIDEO.H
KEY.H
SCRSTK.H
MENU.H
LX800.H
INPUT.H
DECL.H

Also the file VID.ASM is the MASM program used to produce the file VID.OBJ for low level screen handling functions. The purpose of all these programs, both the OMA software and GPIB programs, is explained further in the thesis.

Appendix III

DIP switch settings for addressing parallel connection

GPIB INTERFACE CARD DIP SWITCHES

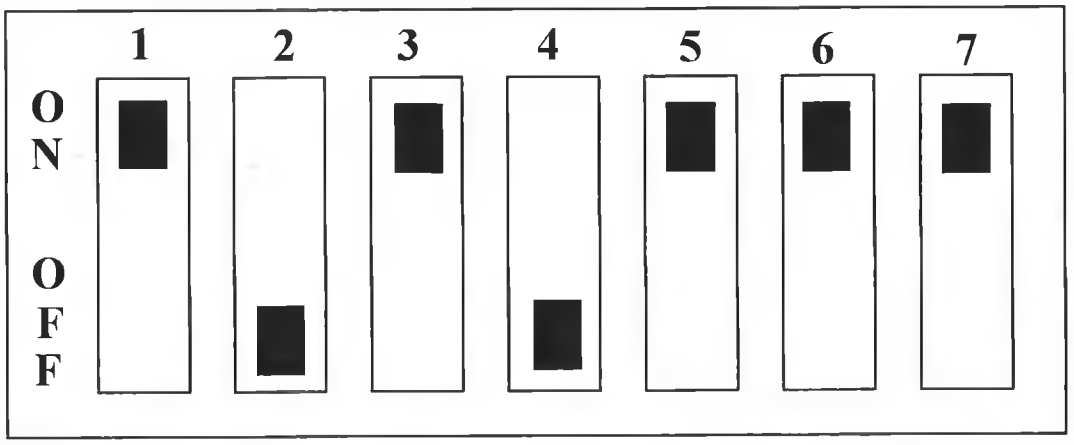

These settings correspond to a Base I/O address for the card of 2B8H

■ **- Switch has been depressed**

1461 DETECTOR INTERFACE DIP SWITCH SETTINGS

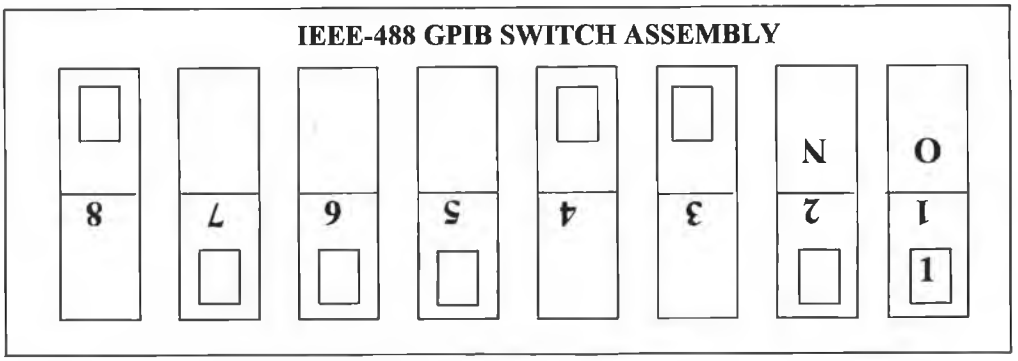

These switch settings 1-5 correspond to the following addresses :

Decimal Address	**12**
Hex Listen Address	**2C**
Hex Talk Address	**4C**

□ **- SWITCH HAS BEEN DEPRESSED**

Acknowledgements

I wish to take this opportunity to sincerely thank my supervisor Dr. John Costello for his interest, enthusiasm and patience throughout my research. You are a great supervisor and I couldn't have completed this work without your encouragement especially over the last few months. I also wish to take this opportunity to thank John's family (Ann, Aine and Emma) and apologise for keeping him late a few nights and in on weekends helping with my thesis. Thank you again.

I would also like to thank Prof. Eugene Kennedy for his helpful advice and Dr. John-Paul Mosnier for a few laughs. To the postgrads in DCU, especially those in the Laser Plasma group ('the lads' - Martin, Lar, Hassan, Ulrich), thank you for your contributions to this thesis and all the good times. Especially to Martin and Lar, we had great craic, many a good racquetball game and some physics thrown in.

To Al Devine, who so generously offered his resource and time in helping me prepare the figures for this thesis, thank you. Your effort is much appreciated. I am indebted to the other technical and administrative staff of the college for providing me with the resources and knowledge to complete this work.

May I say thanks to my family, who have encouraged me throughout my education and never asked for more than my best from me. Particular thanks to my father who encouraged me to go to college and supported me every step of the way. Finally I wish to extend my immeasurable thanks to Camilla for her constant support and patience.